Methodology development for the analysis of AGATA data

Thesis submitted in accordance with the requirements of the
University of Liverpool for the degree of
Doctor in Philosophy

by

Fay Eleanor Elizabeth Filmer

Oliver Lodge Laboratory

December 2011

For my family; Mum, Dad, Tony, Tim, Iza and Zoe.

Dedicated to my Grandparents; Lily, Cissy, George and Fred. I know you are always with me.

Nothing in life is to be feared. It is only to be understood

Marie Currie

Dreams are the touchstones of our character

Henry David Thoreau

Wait a minute, Doc. Ah... Are you telling me that you built a time machine...out of a DeLorean?

Marty McFly

Firstly I would like to thank my supervisors Dr. Andy Boston and Prof. Paul Nolan for providing me with the opportunity to study for a Ph.D., without it I would not be able to pursue a career in Medical Physics. I would also like to thank Dr. John Cresswell, Janet Sampson and Mark Norman for all the computing help they provided me over the last few years. I would like to thank Dr Rob Fay for helping me download my data from the GRID. Thank you also to Dr Pete Cole and Dr Dan Juson for all the help and support given to me over the last few years. A huge thank you has to go to Dr Andrew Robinson, of Manchester University, for all the help and support he gave me throughout the course of my studies. Also thank you to Dr Andy Boston and Prof. Paul Nolan for all the travel opportunities I was given throughout my Ph.D., especially the three months I spent at Laboratori Nazionali di Legnaro. Which leads me to on to thank all the staff member at Laboratori Nazionali di Legnaro, especially Daniele Mengoni, for all the help given to during that time and the other experiments I attended.

I have some lovely memories from my time at Liverpool University. Thank you to Mike Slee and Rob Carroll. I would also like to say thank you and goodbye to the rest of the physics department past and present. Thank you to Vicky Byard, not only for being a good friend, but also being no more than a telephone call when I really needed someone. Without her being there over the last few months I would not have been able to write my thesis. I would like to thank my family for all the help and support that has always been given to me, but especially in the last four years, making it possible to complete my Ph.D. successfully. Finally I would like to thank my boyfriend Andy Wilde for being there for me and also making me smile and laugh. Without his support and consideration, this accomplishment would not have been made possible.

Abstract

The Advanced GAmma Tracking Array (AGATA) project is an European collaboration project that is aiming to construct a next generation gamma-ray spectrometer for nuclear-structure applications. The final array will consist of 180 highly-segmented HPGe detectors mounted into 60 triple clusters forming a full 4π shell. AGATA will utilise pulse-shape analysis and gamma-ray tracking to achieve high photopeak efficiency and peak-to-total. Central to the AGATA spectrometer is the Nouvelle Acquisition temps-Réel Version 1.2 Avec Linux (NARVAL) data-acquisition system that will perform pulse-shape analysis and gamma-ray tracking calculations in real time (online). The system is comprised of separate blocks of actions, called *actors*. Each one containing a self-sufficient piece of code designed for a specific action. AGATA data can be downloaded and replayed through an offline version of NARVAL, known as the NARVAL-emulator. With a new format and techniques there is need to define new methodology to analyse the data. Discussed in the first part of this work will be processing of AGATA data and how by utilising the *actors* of the NARVAL-emulator different output formats can be chosen. In the next part of this work, the Compton polarimetry capability of an AGATA triple cluster will be investigated by utilising pulse-shape analysis and the detector's granularity. The basic design of a Compton polarimeter consists of two detectors; one acting as a scatterer and the second as a absorber. The same principles apply to an AGATA triple cluster with each sector acting as the scatterer and absorber. The pulse-shape analysis algorithm identifies the positions and energies of the interaction points. Data was obtained from the heavy-ion fusion-evaporation of ^{110}Pd (^{32}S,4n) ^{138}Sm at 135 MeV was used to investigate the Compton polarimetry capability of an AGATA triple cluster. This work utilised the phenomenon that the scattering cross-section for gamma rays is larger in the direction perpendicular to its electric field vector than parallel. This is described by the differential Compton scattering cross-section for polarised gamma rays. A useful event to determine linear polarisation occurs if the incident gamma ray is Compton scattered from the first interaction and then fully absorbed at the second interaction. The sum of the energies deposited in the two interactions gives the energy while the azimuthal scattering angle contains the linear polarisation information. To determine the linear polarisation of a gamma ray, a polarisation sensitivity and asymmetry measurement can be made. Such measurements were made in this work using gamma rays from ^{138}Sm of known linear polarisations. The polarisation sensitivity method utilised the incident and scattered gamma-ray energy, in addition to the azimuthal scattering angle information produced from the pulse-shape analysis algorithm. The experimental polarisation sensitivities ranged from 5.0±0.3% at 139.7 keV to 16.4±0.1% at 1287 keV. A asymmetry measurement was carried by determining the number of gamma rays that scattered perpendicular and parallel to the reaction plane. A positive asymmetry would indicate an electric transition and a negative a magnetic one. It was found that there was partial consistency with expectation. From the asymmetry and polarisation sensitivity measurement an experimental linear polarisation for each gamma ray was determined. The result should be in the range $-1 \leq \mathrm{P}(\theta_\gamma) \leq +1$ with the sign propagating through from the asymmetry measurement. Finally a coincidence efficiency and figure of merit was measured and are given as 32.6±1.0% and 3.9±0.2%, respectively at 346.9 keV. Overall it was concluded that there was limited Compton polarimetry capability and proposed reasons for this were discussed.

Contents

List of Figures

List of Tables

Chapter 1

Introduction

High-resolution gamma-ray spectrometers are some of the most sensitive tools there are to probe atomic nuclei and the nature of nuclear states. The emitted gamma rays carry valuable information about the nucleus. For example, spin and parity information of nuclear states can be extracted from angular distribution and linear polarisation experiments [Pau95] [Jon02]. Over the last 40 years, gamma-ray spectrometers have evolved from sodium iodide detectors in the 1970s to the germanium TESSA[1] arrays of the 1980s, to Eurogam[2] of the early 1990s [Sim05]. The increasing sensitivity of gamma-ray spectrometers over the last forty years is shown in Figure 1.1 [Sim06]. The current generation of high-resolution gamma-ray spectrometers utilises the principle of Compton-suppression via bismuth germanate (BGO) scintillator shields which significantly improves the peak-to-total.[3] This is achieved by operating the shields in anti-coincidence with the high-purity germanium (HPGe) detectors, which veto gamma rays that Compton scatter into the shields [Bea94]. An example of a current generation gamma-ray spectrometer is Gammasphere and it provides nuclear-structure physics with the highest efficiency 4π detector array [Sim05]. The Gammasphere array, based at Argonne National Laboratory, consists of ~100 Compton-suppressed (HPGe) detectors in a spherical configuration. It has

---

[1] The Escape-Suppressed Spectrometer Array. An UK first generation gamma-ray detector array.

[2] An UK/French second generation gamma-ray detector array.

[3] Ratio between the counts in a full energy peak and the total counts of a gamma-ray spectrum.

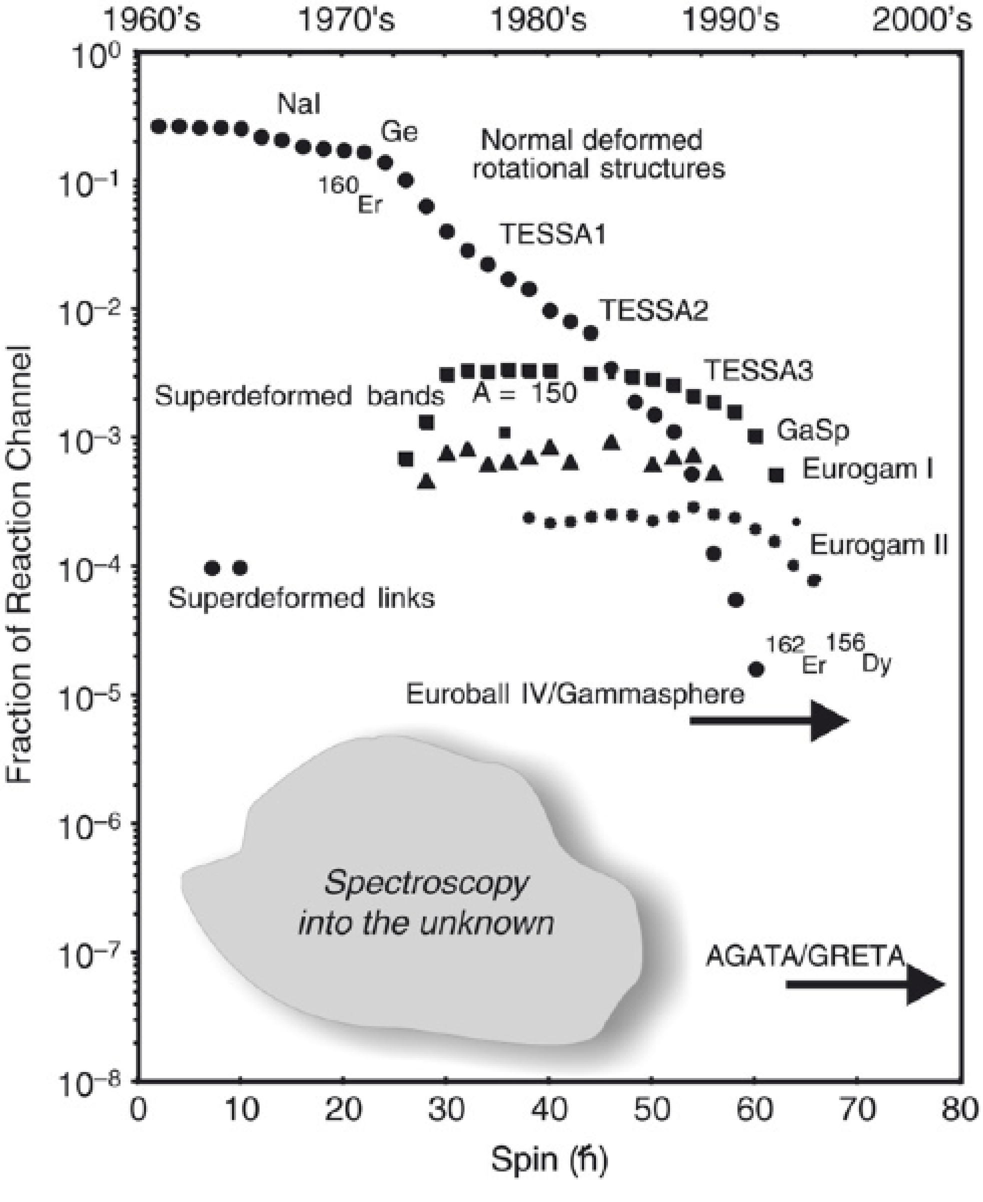

Figure 1.1: The evolution of gamma-ray spectrometers since the 1970s which shows the sensitivity achieved in terms of the weakest states that can be observed with each new gamma-ray detector array. To observe even weaker states a much more powerful spectrometer is required. Future spectrometers, for example AGATA, will achieve potentially 1000 times higher sensitivity at low intensity and with high-spin decays [Sim06].

a photopeak efficiency[4] of ∼9% at 1 MeV gamma-ray energy. Each new development in gamma-ray detectors since the 1970s has brought considerable advancement in the field of nuclear-structure physics. However, there are still many unanswered questions which is hoped will be addressed with the next generation of gamma-ray detectors. They current research questions include [Sim06],

- How does nuclear-shell structure evolve in exotic neutron-rich nuclei?
- How do collectivity and pairing correlations change in neutron-rich nuclei?
- What is the structure of the heaviest nuclear systems?
- What are the limits of the high-spin domain?

1.1 Challenges for current gamma-ray spectrometers

There are currently several new facilities under construction, for example, FAIR[5] and SPIRAL2 which when completed will host experiments that will aim to extend current nuclear-structure knowledge. However, it has been noted, that due to low-beam intensities, large Doppler-broadening and high backgrounds, experiments will be challenging. As a result there is a need for greater efficiency and energy resolution. In current gamma-ray detector arrays, which utilise Compton suppression, improvements in efficiency are restricted by the fraction of solid angle covered the the BGO shields [Sim05].

1.2 Future of gamma-ray spectroscopy

A spectrometer composed of highly-segmented HPGe that will utilise the method of gamma-ray tracking through pulse-shape analysis has been proposed. In this method

---

[4] The fraction of all gamma rays of a given energy which are totally absorbed [Han67].

[5] Facility for Antiproton and Ion Research

the path that the gamma ray took is reconstructed. As a result the BGO Compton-suppression will be removed and as such would allow for a 4π coverage. There are currently two gamma-ray tracking arrays under construction; the Advanced GAmma Tracking Array (AGATA) project (European collaboration) and the Gamma-Ray Energy Tracking Array (GRETA) (American collaboration). The aim of AGATA is to construct a next generation gamma-ray spectrometer for nuclear-structure applications. The final array will consist of 180 asymmetric segmented HPGe detectors mounted into 60 triple clusters in a full 4π shell of Ge. Further details on the AGATA spectrometer are presented in Chapter Three. A schematic diagram of five triple clusters and a Geant4 model of the final array are shown in Figure 1.2 [Sim05].

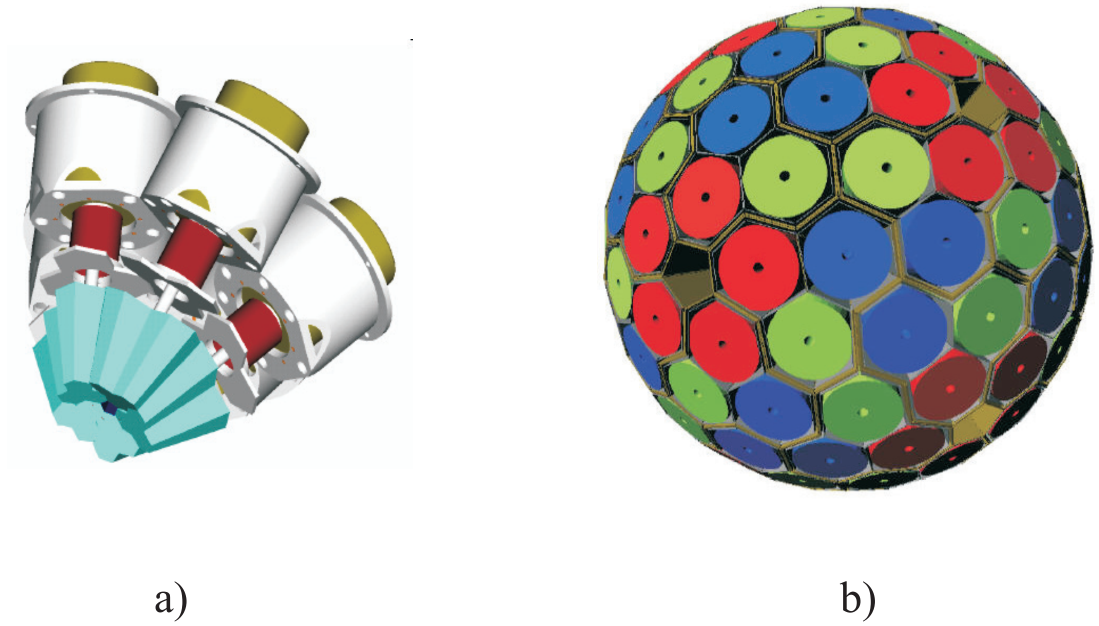

Figure 1.2: a) A schematic representation of five AGATA triple clusters. Each triple cluster consists of three asymmetric detectors mounted in a cryostat. b) A Geant4 simulation model of the final 4π array. There are 60 triple clusters in the final array. Each of the asymmetric detectors is labelled blue, green and red [Sim05].

1.3 Aims of this thesis

Central to the AGATA spectrometer is the Nouvelle Acquisition temps-Réel Version 1.2 Avec Linux (NARVAL) data-acquisition system that will perform pulse-shape analysis and gamma-ray tracking calculations. With a new format and techniques there is need to define new methodology to analyse the data. The first part of this thesis is concerned with the processing of AGATA data. The second part will apply pulse-shape analysis techniques to investigate the Compton polarimetry capability of an AGATA triple cluster. Compton polarimetry is a method of distinguishing between the electric and magnetic character of transitions. Techniques have been successfully used since the 1950s and are based the phenomenon that the scattering cross-section for gamma rays is larger in the direction perpendicular to its electric field vector than parallel to it. The basic method of Compton polarimetry involves using two or more detectors, one as a scatterer and the other one as an absorber(s) [Lei97]. With the development of new detectors, for example Clover and Cluster (Section 2.4), improvements in efficiency and sensitivity were observed. In these arrangements each detector acts as a scatterer and an absorber. AGATA will utilise the technique of pulse-shape analysis and as a result will accurately locate the position of the gamma-ray interactions. This should result in an increase in sensitivity and could enable Compton polarimetry measurements potentially to be carried out on the weakest transitions.

1.4 Thesis overview

This thesis will investigate the methodology development in the processing of AGATA data and the Compton polarimetry capability of one AGATA triple cluster. The following outline the details of the forthcoming chapters.

- Chapter 2 will discuss electromagnetic transitions and give details on linear polarisation. The chapter will then discuss the principle mechanisms by which gamma-rays interact with matter. Next it will deal with the fundamentals of Compton polarimetry and gives examples of previous work.

- Chapter 3 will introduce the AGATA spectrometer and its constitute parts. The fundamentals of pulse-shape analysis and gamma-ray tracking will be discussed. Next details of the NARVAL data-acquisition will be given and procedure for downloading AGATA data. Finally detector performance characteristics will be outlined.
- Chapter 4 will discuss the commissioning experiments of the AGATA spectrometer that were undertaken prior to the start of the physics campaign. Next the chapter will give details of the experiment that was performed to obtain the data analysed in this thesis. Finally, the methodology for processing AGATA data will be discussed and how this will be applied to determining the Compton polarimetry capability of an AGATA triple cluster.
- Chapter 5 will outline and discuss the Compton polarimetry capability results of an AGATA triple cluster.
- Chapter 6 will summarise the main findings in this thesis and outline future work.

Chapter 2

Gamma-ray Compton polarimetry

2.1 Fusion-evaporation reaction

In this thesis the Compton polarimetry capability of an AGATA triple cluster was investigated from the heavy-ion fusion-evaporation reaction, ^{110}Pd (^{32}S,4n) ^{138}Sm at 135 MeV. In this type of reaction sufficiently high-beam energies are used to overcome Coulomb repulsion and fuse two nuclei together. If the impact parameter $\mathbf{b}$ is of the order of 1.2 fm the two nuclei will touch, the beam energy is sufficient to overcome the Coulomb barrier and a compound nucleus is formed. The resulting compound nucleus is in an excited state with the kinetic energy of the collision converted into the excitation energy of the compound system. The amount of angular momentum transferred to the compound nucleus is,

$$\mathbf{l} = \mathbf{b} \times \mathbf{p}, \tag{2.1}$$

where $\mathbf{p}$ is the linear momentum of the beam. It follows that at higher beam energies more angular momentum will be transferred. The compound nucleus must live longer than 10^{-20} seconds for thermodynamic equilibrium to occur. During this time the compound nucleus loses its formation knowledge, but conserves energy and angular momentum. Excitation energy is released, via particle and gamma-ray emission, if the compound nucleus is stable against fission. Nucleon evaporation occurs approximately

10^{-19} seconds after the initial impact. This results in the production of excited residual nuclei. The emitted nucleons carry away at least their binding energy (8–10 MeV), but only a small amount of angular momentum ($\sim 1\hbar$). The residual nucleus will lose excitation energy, via the emission of dipole gamma-rays, when the excitation energy, relative to the rotational energy, is reduced below the particle-emission energy threshold ($\sim$8 MeV). This process is know as statistical gamma-ray emission and occurs 10^{-15} seconds after impact. The dipole radiation continues to be emitted until the nucleus reaches the yrast line at which point quadrupole gamma-ray emission dominates. The yrast state is the state of lowest energy for a given value of angular momentum. The residual nucleus loses angular momentum as the quadrupole gamma-ray emission allows the nucleus to cascade down from one level to the next, this occurs 10^{-12} seconds after impact. After 10^{-9} seconds the residual nucleus reaches its ground state, and if the nucleus is not stable, radioactive decay will occur. The fusion-evaporation process is illustrated in Figure 2.1. In order to determine the polarisation of excited nuclear states the angular distribution can be measured. To achieve this the nucleus needs to be populated in such a way that has been described and results in aligned states of angular momentum. In fusion evaporation the angular momentum vector (Eq. 2.1) is in a plane perpendicular to the beam direction [Cas05] [Lei97] [Kra88].

2.2 Electromagnetic transitions

Within a nucleus a transition between discrete states must follow conservation laws. Following a fusion-evaporation reaction the compound nucleus is left with an orientation. The alignment of the angular momentum vectors of the resulting nuclei means that the intensities of the gamma-ray transitions are dependent on the angle of observation. These angular distributions are characterised by the multipole of the gamma-ray emission. The emissions are directly related to the nuclear state with the

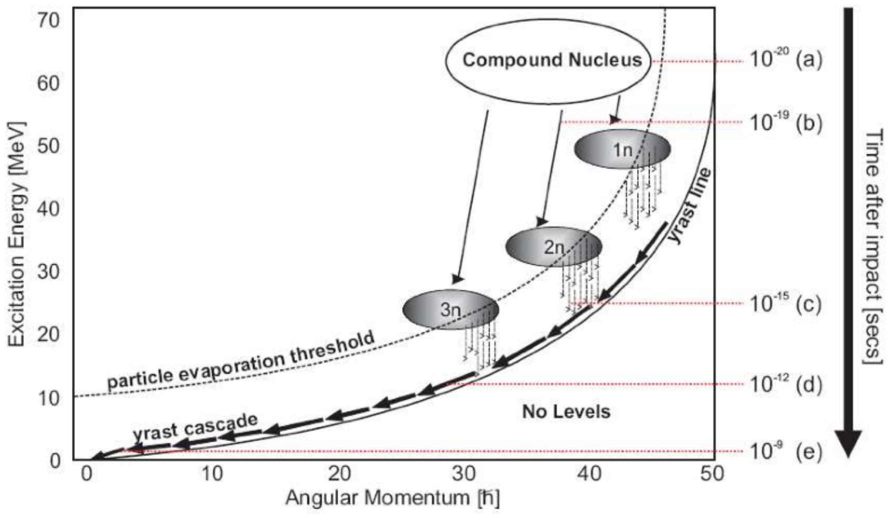

Figure 2.1: A schematic diagram to illustrate the process of energy and spin loss by a nucleus following a fusion-evaporation reaction [Dar06].

intensity of the emitted photons given the Poynting vector [Ben11],

$$\mathbf{P} = \left(\frac{c}{4\pi}\right) \mathbf{E} \times \mathbf{M}, \tag{2.2}$$

whose magnitude is expressed by

$$\left(\frac{c}{4\pi}\right) |\mathbf{E}|^2$$

or

$$\left(\frac{c}{4\pi}\right) |\mathbf{M}|^2$$

where **E** and **M** are the electric and magnetic components respectively, c is the speed of light. The angular distribution for the electric and magnetic multipoles are the same. Due to the symmetry of the reaction any variation in the intensity is dependent on θ. The angular distribution of gamma rays is described as,

$$W(\theta_\gamma) = A_0 + A_2 P_2(\cos\theta_\gamma) + A_4 P_4(\cos\theta_\gamma), \tag{2.3}$$

where $P_x(\cos\theta_\gamma)$ are Legendre polynomials and θ_γ is the emission angle of the gamma ray with respect to the beam direction. The ratios A_2/A_0 and A_4/A_0 are angular distribution coefficients which depend on the sub-state population distribution of the initial state, the spins of the initial and final states, the multipole orders and the multipole mixture of the gamma radiation. The electric field vector for linearly polarised gamma rays is parallel or perpendicular to the emission plane. The plane is defined by the beam direction and the direction of the gamma rays. The angle between the emission plane and the electric field vector is ϕ and the polarisation parameter is given by [Twi75] [Lei97],

$$P(\theta_\gamma) = \frac{W(\theta_\gamma, 0^\circ) - W(\theta_\gamma, 90^\circ)}{W(\theta_\gamma, 0^\circ) + W(\theta_\gamma, 90^\circ)}, \tag{2.4}$$

and is in the range of $-1 \leq \mathrm{P}(\theta_\gamma) \leq +1$. The sign is determined from the multipole character [Lei97].

2.3 Introduction to Compton polarimetry

2.3.1 Interactions of gamma rays with matter

The principal mechanisms by which gamma-rays interact with matter are photoelectric absorption (Figure 2.2a), Compton scattering (Figure 2.2b) and pair production (Figure 2.2c). The probability that a particular mechanism will occur depends on the gamma-ray energy and the atomic number of the matter [Kno00].

Photoelectric absorption

This is the dominant process at a gamma-ray energy of <150 keV in Ge. The energy is transferred to an atomic electron, usually the most tightly bound (K-shell) electron of an atom, which is released. The energy of the emitted electron is equal to the incident gamma-ray energy less the binding energy of the electron as shown in the following (assuming no recoil of the atom),

$$E_{e^-} = E_\gamma - E_b, \tag{2.5}$$

where E_γ is the incident gamma-ray energy and E_b is the binding energy of the electron. The cross section (σ_{PA}) for a gamma ray undergoing photoelectric absorption

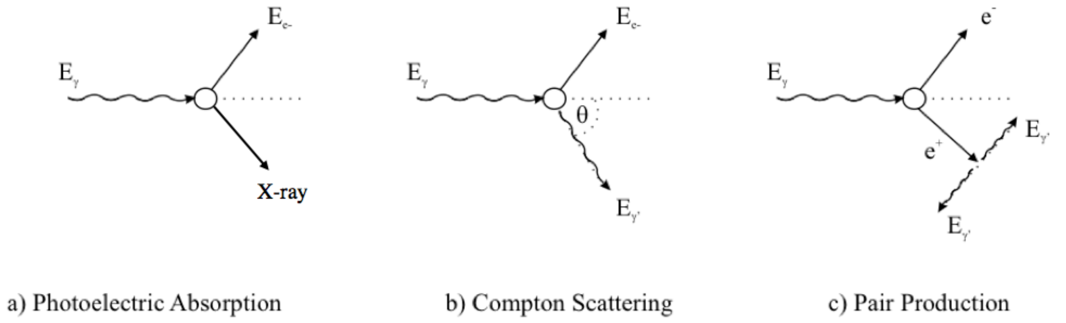

Figure 2.2: Schematic representation of the principal mechanisms by which gamma-rays interact with matter. (a) Photoelectric absorption is the dominant process in Ge at a gamma-ray energy of <150 keV. The gamma ray is completely absorbed by the atom, then this gamma-ray energy is transferred to an electron of the atom which is in turn released. (b) Compton scattering is the dominant process at a gamma-ray energy in the range of ∼150 keV to ∼6 MeV region. An incident gamma ray transfers part of its energy to a loosely bound electron. The gamma ray is scattered and has an energy defined by the Compton scattering formula. (c) Pair production can occur when the energy of the gamma ray exceeds twice the rest mass of an electron (1022 keV), the gamma ray is replaced by an electron-positron pair [Kno00] [Dim08].

varies with the Z of the atom and the incident energy of the gamma ray as,

$$\sigma_{PA} \propto \left(\frac{Z^n}{E_\gamma^{3.5}} \right), \tag{2.6}$$

where exponent n varies between 4 and 5 depending on the incident gamma-ray energy. When an electron is ejected from the K or L shells of an atom, this results in an electron from a higher energy state falling into the gap, releasing in the emission of an X-ray [Kno00].

Compton scattering

Compton scattering in Ge is the most probable interaction mechanism with gamma-ray energies in the range of ∼150 keV to ∼6 MeV. In this process the incident gamma ray transfers a fraction of its energy to a loosely bound electron, which is scattered at an angle. The energy of the scattered γ-ray ($E_{\gamma'}$) is defined by,

$$E_{\gamma'} = \frac{E_\gamma}{1 + \frac{E_\gamma}{m_0 c^2}\left(1 - cos\theta\right)}, \tag{2.7}$$

where E_γ is the incident gamma-ray energy and $m_0 c^2$ is the rest mass energy of the electron (511 keV). For the differential scattering cross-section, $d\sigma/d\Omega$, the angular distribution of the scattered gamma rays can be determined from the Klein-Nishina formula as [Dav65],

$$\frac{d\sigma}{d\Omega} = Zr_0^2\left(\frac{1}{1+\alpha\left(1-cos\theta\right)}\right)^2\left(\frac{1+cos^2\theta}{2}\right)\left(1+\frac{\alpha^2\left(1-cos\theta\right)^2}{\left(1+cos^2\theta\right)\left[1+\alpha\left(1-cos\theta\right)\right]}\right), \tag{2.8}$$

where $\alpha = E_\gamma/m_0 c^2$ and r_0 is the electron radius. Plotting the differential scattering cross-section as a function of incident gamma-ray energy demonstrates a tendency for the gamma ray to forward scatter as energy increases [Kno00]. This is shown schematically in Figure 2.3.

Pair production

Pair production can occur when the energy of the gamma ray exceeds twice the rest mass of an electron (1022 keV). In Ge pair production is the dominant mechanism above ∼6 MeV. This interaction must take place in the Coulomb field to conserve momentum. The gamma ray is replaced by an electron-positron pair. If the energy exceeds 1022 keV then the excess energy is transferred as kinetic energy to both particles. After a short distance (<1 mm) the positron will annihilate with an electron emitting two 511 keV gamma rays [Kno00].

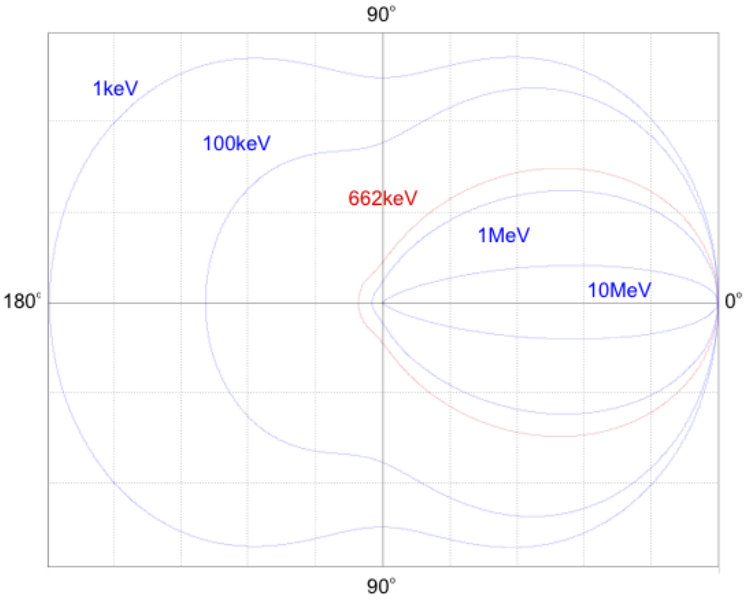

Figure 2.3: A normalised polar plot demonstrating the angular distribution of the scattering of gamma rays in Ge as a function of gamma-ray energy. This plot demonstrates a tendency for the gamma ray to forward scatter as energy increases [Kno00].

2.3.2 Basic Compton polarimetry techniques

In order to investigate the polarisation of gamma rays for the energy range from 60 keV up to several MeV, the Compton scattering effect, which is known to be sensitive to linear polarisation, is usually employed. Compton polarimetry techniques have been successfully used since the 1950s and utilise the phenomenon that the scattering cross-section for gamma rays is larger in the direction perpendicular to its electric field vector than parallel to it. This is described by the differential Compton scattering cross-section for polarised gamma rays [Eva55].

$$d\sigma = \frac{{r_0}^2}{2} d\Omega \left(\frac{{k_1}^2}{{k_0}^2}\right) \left(\frac{k_0}{k_1} + \frac{k_1}{k_0} - 2\sin^2\theta\cos^2\phi\right), \tag{2.9}$$

Where k_0 is the wave number of the incident gamma ray, k_1 is the wave number of the scattered gamma ray, θ is the Compton scattering angle and ϕ is the azimuthal scattering angle, that is the scattering angle between the plane of Compton scattering and the polarisation plane (shown as a schematic diagram in Figure 2.4). The wave number is defined as,

$$k = \frac{E_\gamma}{\hbar c}. \tag{2.10}$$

The basic method of Compton polarimetry involves using two or more detectors, one as a *scatterer* and the other one as an *absorber*, see Figure 2.5. The gamma ray is Compton scattered from the *scatterer* and, for an useful event, is fully absorbed in the *absorber* [Lei97]. The absorber detectors are at 0° and 90° with respect to the plane defined by the incident of the polarisation orientation of the gamma ray and its incident propagational direction. The degree of linear polarisation can be determined from the angular distribution of gamma rays [Fer79].

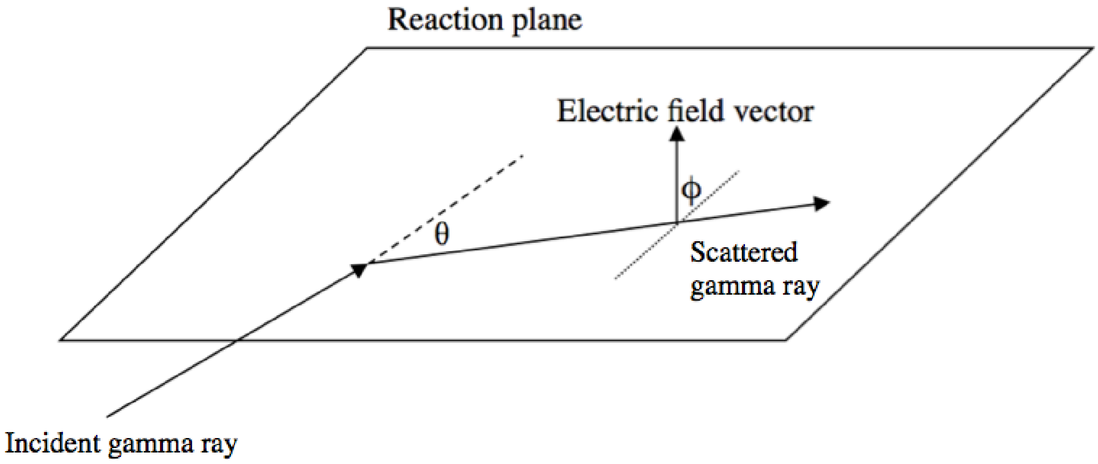

Figure 2.4: Schematic representation of polarised Compton scattering. The polar angle θ is measured from the direction of the incident gamma ray. The azimuthal angle ϕ is measured from the plane containing the electric field vector.

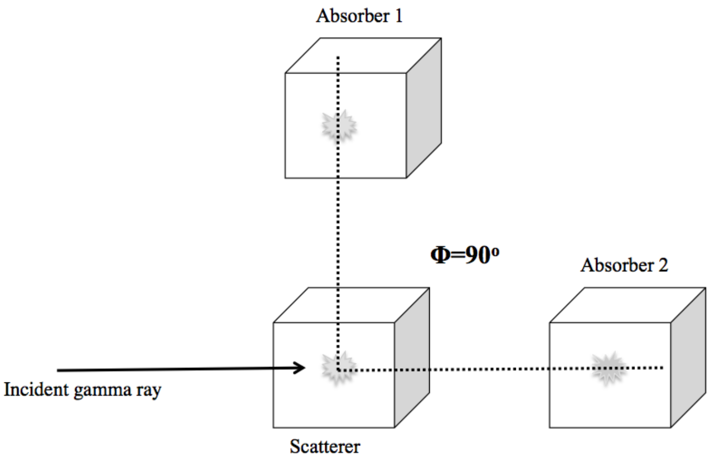

Figure 2.5: Schematic diagram of a basic Compton polarimetry design. The first detector is known as a *scatterer* and second detectors at 90° and 0°, respectively, are *absorbers*.

2.3.3 Modulation factor

The modulation factor, expressed in normalised units, is used to find the the maximum scatter direction and is given by the following,

$$R(\phi) = \frac{N(\phi + 90) - N(\theta)}{N(\phi + 90) + N(\theta)} = \frac{\sigma_\perp - \sigma_\parallel}{\sigma_\perp + \sigma_\parallel}, \tag{2.11}$$

where N is the number of scattered gamma rays and ϕ is the azimuthal scattering angle. The quantities $\sigma_\perp$ and $\sigma_\parallel$ are the differential cross-sections of Compton scattering in a direction perpendicular and parallel to a reaction plane, respectively. R reaches a maximum when ϕ is in the direction of the initial polarisation vector and minimum when perpendicular. The modulation factor as a function of Compton scattering angle θ is represented in Figure 2.6. From Figure 2.6 it can be seen that 50 keV gamma rays have the highest modulation factor and 800 keV gamma rays have the lowest; lower energies have a higher modulation factor. The maximum modulation fraction is approximately 90% for energies below 200 keV, and occurs for events that Compton scatter by around 90°. The peak of the curve moves slightly to smaller angles with increasing energy. A modulation factor tends to zero for small scattering angles and for back scatter. It follows that the most useful events are those that scatter around

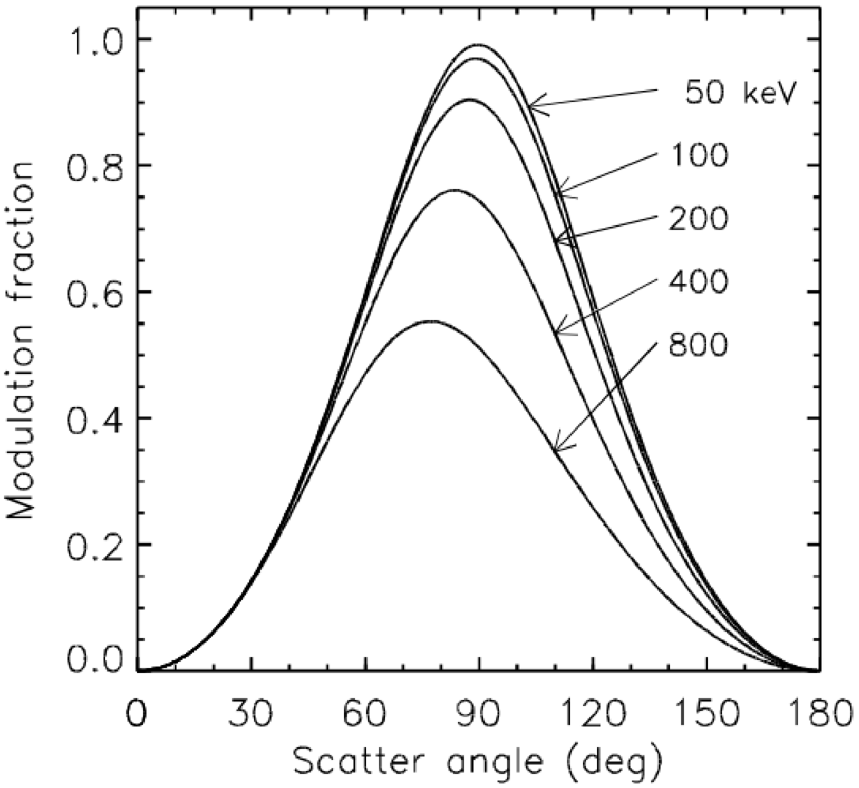

Figure 2.6: Modulation factor as a function of the Compton scattering angle θ for gamma-ray energies 50-800 keV. For a incident gamma-ray energy the modulation fraction is maximised when the scattering angle is slightly less than 90° [Fer79].

the angle of 90° [Fer79].

2.3.4 Limitations of basic Compton polarimetry design

The following outlines some of the limitations of the basic Compton polarimetry setup.

- Low efficiency for the detection of linear polarisation due to incomplete coverage of the scatterer material by the absorber.
- The scatterer should have a small active volume in order for the scattered

gamma ray to have a high probability to escape after one interaction [Wer95]. This is necessary as linear polarisation information is lost after one or two Compton scatters.

- If a gamma ray scatters with different azimuthal angles or Compton scattering angles which are not in the region of 90°, a smearing of modulation could be introduced. In order to avoid significant smearing, the scatterer and absorber detector can be placed with a large empty place in between. As a result there is a small ratio of the effective area of the absorber to the total geometrical area of both scatterer and absorber. This can be problematic where space limited experimental environments [Cos95].

Such polarimeters are still used in this basic arrangement due to the ease of use and low cost involved [Wer95].

2.3.5 Characterisation of a Compton polarimeter

There are several parameters widely used in order to compare efficiencies of different polarimeters. Relevant examples are polarisation sensitivity (Q), and figure of merit (F) .

Polarisation sensitivity of a detector (Q)

This is a measure of the detector's response to linear polarisation. The response of an ideal polarimeter, assuming a point-like detector, is given by,

$$Q_0 = \frac{1+\alpha}{1+\alpha+\alpha^2}. \tag{2.12}$$

where, $\alpha = \frac{E_\gamma}{m_e c^2}$. Polarisation sensitivity of a non-ideal polarimeter is a fraction of this value because of the finite size of detectors. The polarisation sensitivity value can be determined experimentally by using Eq. 2.11 for 100% polarised gamma rays [Met50].

Figure of merit (*F*)

The figure of merit is a method that was defined by *Logan et al.* [Log73] for comparing different type of polarimeters and is given by,

$$F = \varepsilon Q^2. \tag{2.13}$$

It takes into account the polarisation sensitivity and the coincidence efficiency[1] (ε) of the detector [Mil08].

2.4 Compton polarimetry using composite detectors

2.4.1 Clover and Cluster detectors

Composite detectors consist of a number of Ge detectors in close geometry. Efficiency is increased for such detector arrays because the whole arrangement is treated as a large detector. This is achieved by adding up the individual signals from each detector. Two types of composite detectors are Clover (Figure 2.7a) and Cluster (Figure 2.7b) which were developed for the Euroball project. The Clover detector was developed by the Eurogam collaboration. It consists of four coaxial Ge detector, in a four-leaf clover arrangement, mounted in a common cryostat. Each detector is 50mm in width and 70mm in length. A Cluster detector consists of seven large hexagonal Ge detectors which are individually encapsulated, The detectors are closely pack into a common cryostat and surrounded by a common BGO escape-suppression shield. The hexagonal front face of the detector has a diameter of 59mm and the back face has diameter of 70mm. The length of each detector is 78mm [Lei97].

2.4.2 Compton polarimetry techniques of composite detectors

Composite detectors can be used as Compton polarimeters due to their granularity. Each Ge detector can act as a scatterer and an absorber [Lei97].

---

[1] This is this probability of measuring coincidences between the scatterer and absorber sectors.

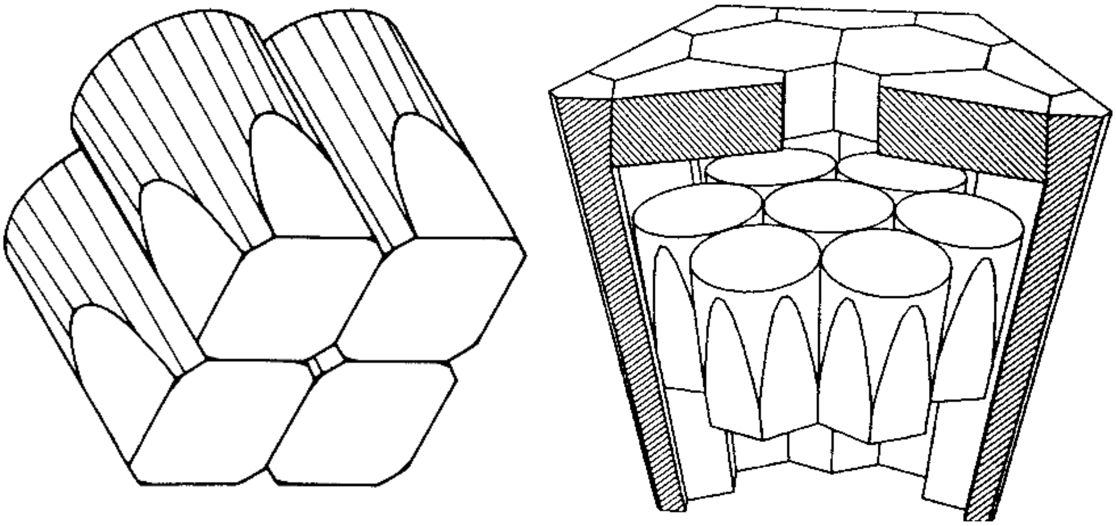

(a) Clover detector

(b) Cluster detector

Figure 2.7: (a) Schematic representation of the Clover detector. Each detector is 50mm in diameter and 70mm in length and is grouped in this four-leaf clover arrangement. (b) Schematic representation of the Cluster detector surrounded by a common BGO escape-suppression shield. The front face and back face are 59mm and 70mm, in diameter, respectively. The length of each detector is 78mm [Lei97].

Clover techniques

A schematic representation of a Clover detector array indicating the scattering directions in shown in Figure 2.8. In this arrangement the geometry is orthogonal; detectors in this geometry were designed by *Twin et al.* [Twi75]. The polarisation sensitivity Q is defined as,

$$Q = \frac{A}{P}, \tag{2.14}$$

where P is the polarisation parameter as defined in Eq. 2.4 and A is the measured asymmetry given as,

$$A = \frac{N_{\perp} - N_{\parallel}}{N_{\perp} + N_{\parallel}}. \tag{2.15}$$

In Eq. 2.15, $N_{\perp}$ and $N_{\parallel}$ are the counting rates for scatters perpendicular and parallel to the emission plane, respectively. The emission plane is indicated in Figure 2.8. It

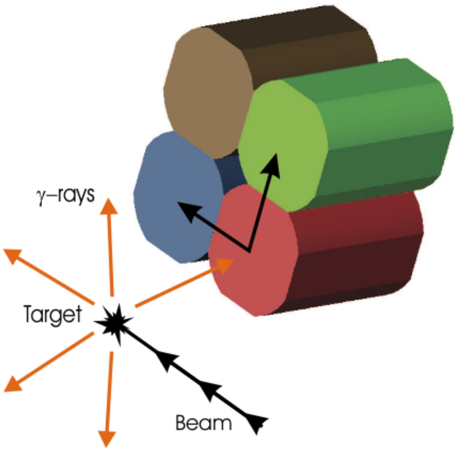

Figure 2.8: A four detector Clover array. Each detector acts as a scatter and an absorber.

is defined by the beam direction and the direction of the incident gamma ray [Lei97] [Duc99].

Cluster techniques

To determine the polarisation sensitivity of the Cluster, Eq. 2.15 has to be adapted because the geometry is non-orthogonal as,

$$A = \frac{Q'P}{1 + \kappa Q'P}, \tag{2.16}$$

where Q' is the polarisation sensitivity of a non-orthogonal polarimeter and ϕ, the plane incline is defined by,

$$\kappa = \frac{\sin^2\phi' - \cos^2\phi}{\cos^2\phi - cos^2\phi'}. \tag{2.17}$$

where ϕ'=90° [Dro06] [Gar95].

2.4.3 Improvement in sensitivity with composite detectors

Butler et al. [But73] constructed and tested a three Ge(Li) Compton polarimeter. By using gamma rays of known linear polarisation, the polarisation sensitivity of a three detector setup was measured. The experimental setup in shown in Figure 2.9. The method made use of the relationships given in Eq. 2.14 and 2.15. The results of polarisation sensitivity as a function of energy is shown in Figure 2.10. This is shown as a comparison to Clover and Cluster detectors. It can seen from Figure 2.10 that the polarisation sensitivity of Clover and Cluster detectors are in agreement. However, a three Ge(Li) polarimeter in about a factor of 2 more sensitive. The Clover and Cluster detector are less sensitive due to the compact geometry of composite detectors. This results in large scattering angles between the scatterer and the absorber detector. This effect is compensated by the large polarimeter efficiency of such detectors. Polarimeter efficiency is defined as the probability of measuring coincidence between the scatterer and absorber. The figure of merit (Section 2.3.5) is used as a comparison between polarimeters as it represents both efficiency and polarisation sensitivity [Bec92].

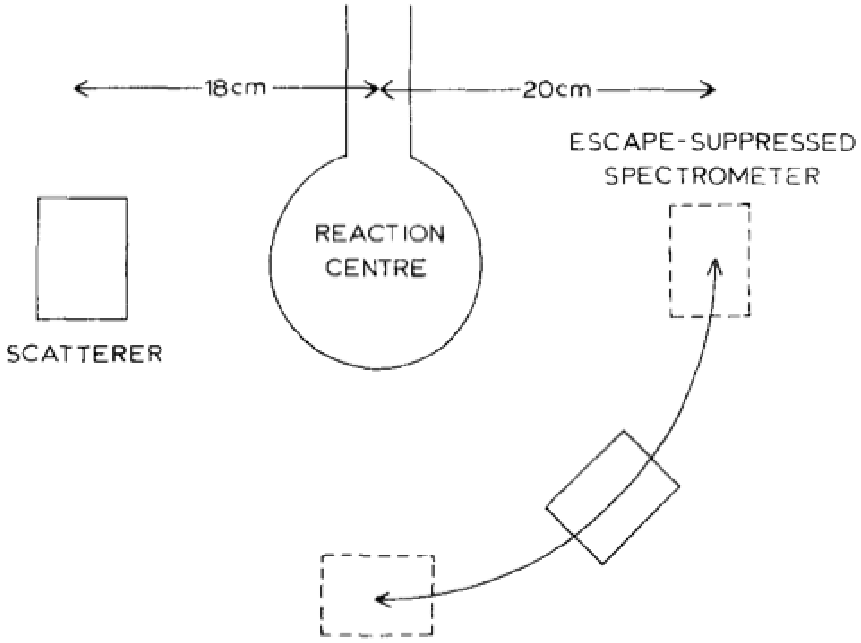

Figure 2.9: Schematic representation of the arrangement used by *Butler et al.* [But73]

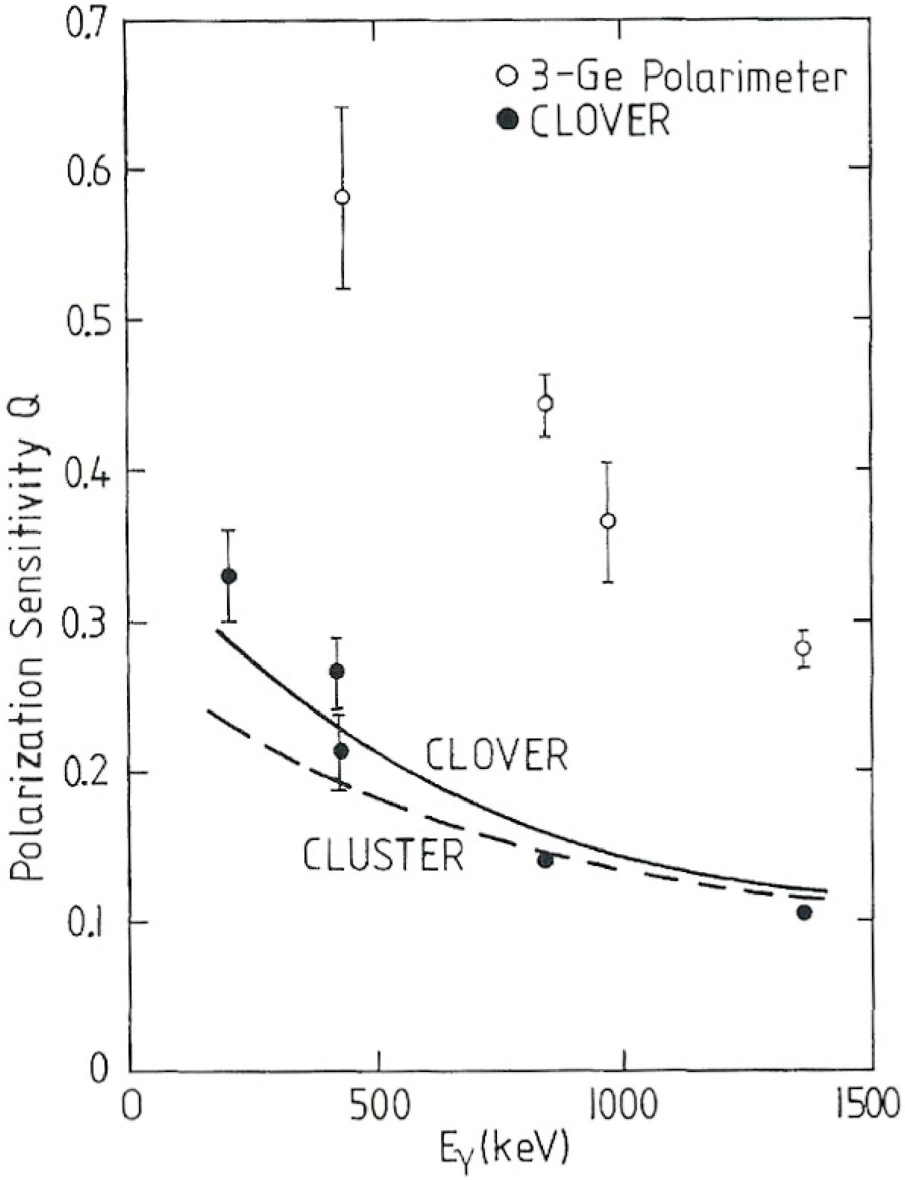

Figure 2.10: Polarisation sensitivity (Q) as a function of energy for a 3-Ge polarimeter, Clover and Cluster detector. The points are experimental results for a 3-Ge polarimeter and Clover detector. The lines are Monte-Carlo results for Clover and Cluster detectors [Lie97].

2.5 Other techniques of Compton polarimetry

Segmentation of a Ge detector increases the granularity of the gamma-ray detector array. Each detector of the array is divided up into a number of individually electrically segmented sectors. Signals are only collected from the sector where the gamma ray interacted.

2.5.1 The Segmented Germanium Array (SeGA)

A successful Compton polarimetry experiment involving a segmented Ge detector was carried out by *Miller et al.* in 2008. Polarisation sensitivity measurements were determined, by using four detectors from SeGA array, from alpha-gamma coincidence of ^{249}Cf. The experimental setup is shown in Figure 2.11. The array consists of 18

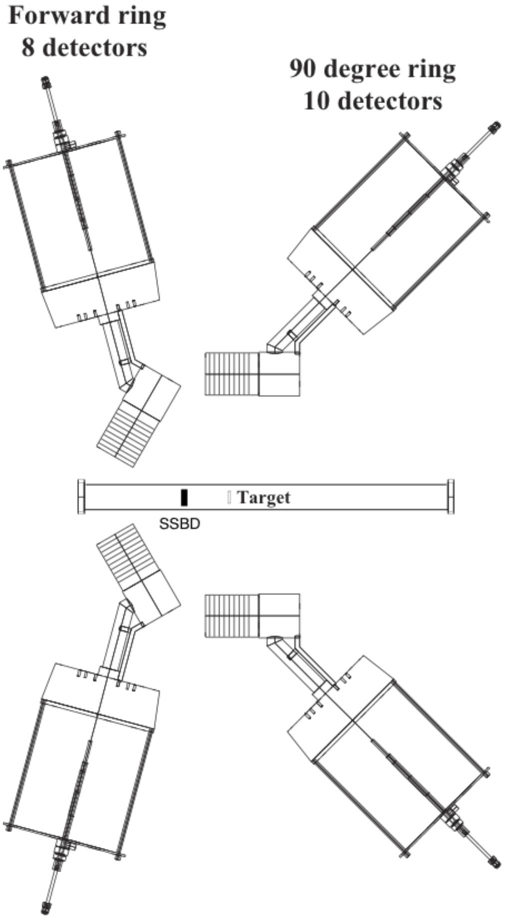

Figure 2.11: A standard SeGA setup with an added silicon surface barrier detector used for this measurement [Mil08].

detectors. Each cylindrical crystal is 80 mm long, 70 mm in diameter and made of n-type high-purity germanium. The outer p-type ion-implanted contact of the crystal is vertically segmented into four longitudinal segments and horizontally segmented into eight transverse segments. This is represented in Figure 2.12. There were detectors at forward and backward angles to allow for angular correlation calculations to be performed. The detectors were irradiated from the side to utilise the transversal segmentation allowing for better Doppler correction. The polarisation sensitivity of Q~0.14 for 350 keV [Mil08] was measured. This value is less than a Clover or Cluster detector. However, the experiment demonstrated that the SeGA array could be used as a Compton polarimeter.

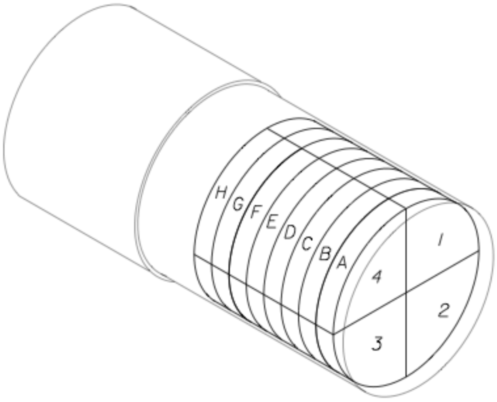

Figure 2.12: The segmentation of a SeGA detector [Mil08].

Chapter 3

The AGATA spectrometer

3.1 The AGATA project

The aim of the AGATA project is to construct a 4π array of highly-segmented HPGe detectors based on the techniques of gamma-ray tracking and pulse-shape analysis. The final array will consist of 60 asymmetric triple clusters with a single cryostat per triple cluster [Sim05]. Each detector of the triple cluster has a different geometry to allow for better 4π coverage; the detectors are labelled blue, green and red. This is represented in Figure 3.1 [Wie10].

3.1.1 Constituents of the AGATA spectrometer

An AGATA detector

Each individual crystal has a lithium-drifted positive centre-contact and 36 electrically segmented boron-implanted negative outer-contacts. Each detector consists of an HPGe hexagonal crystal that is 9 cm long and 8 cm in diameter with a tapering angle of $\sim 8^\circ$. Laterally it is segmented into rings measured from the front ring, with each ring further segmented into six sectors. The depth of each ring is given in Figure 3.2c. Finally there is a 5 mm radius bole in the middle of the crystal [Rec08]. This is also shown schematically in Figure 3.2c. Each ring is numbered from one to six,

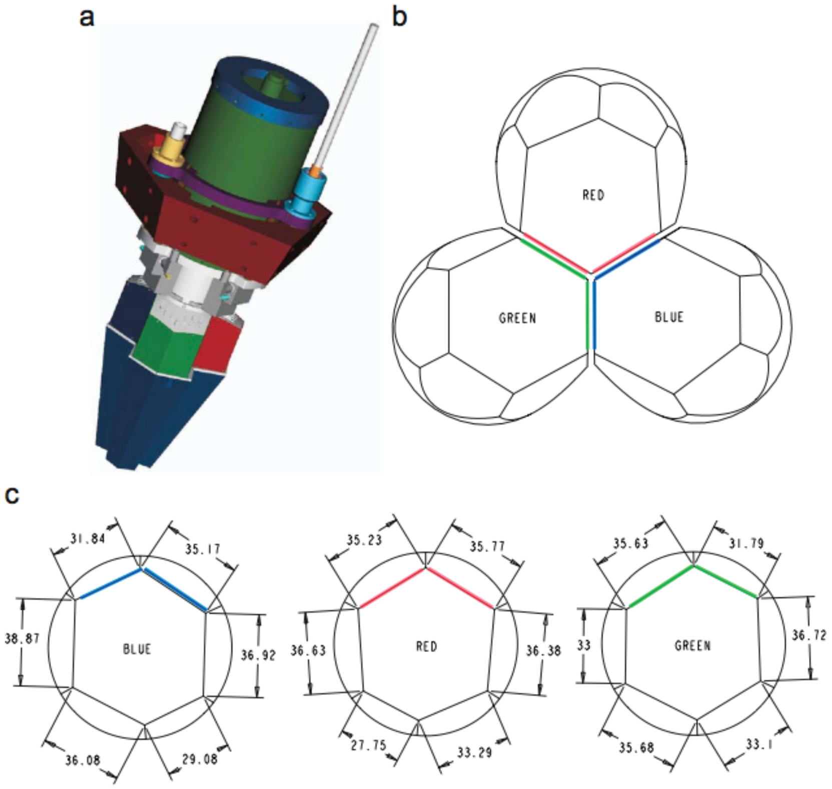

Figure 3.1: An AGATA asymmetric cryostat. (a) Schematic drawing of the crystal configuration (b) Schematic representation of the crystal configuration. (c) The geometry specifications of the red, blue and green crystals. The dimensions are in mm [Bos09].

starting at the first ring (Figure 3.2a). The six segments of each ring are labelled A-F (Figure 3.2b). Each crystal is encapsulated with 0.8 mm thick aluminium [Wie10].

An AGATA triple cluster

Three of the encapsulated crystals, one of each geometry, are mounted in a cryostat forming a triple cluster. An end cap is placed around the encapsulated crystals. There is an internal distance of 0.5 mm between the end cap and encapsulated crystal capsule. Figure 3.3a shows a typical constructed triple cluster with a cryostat. In Figure 3.3b is a graphically edited photograph of a triple cluster showing the alignment of the encapsulated crystals relative to the end cap [Wie10]. The crystals in the

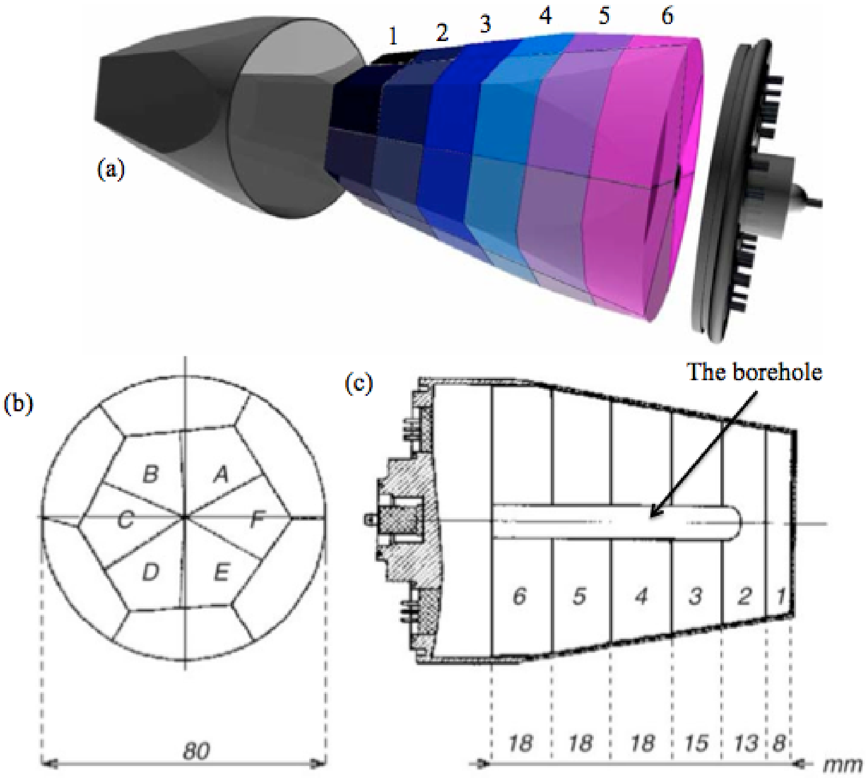

Figure 3.2: (a) Schematic representation of an AGATA detector showing the number of ring of the crystal, labelled 1-6. (b) Schematic drawing of the front ring of a AGATA crystal; each subdivided sectors of the ring A-F. (c) Schematic drawing of a horizontal cross section of an AGATA crystal showing the depth of each ring (1-6) [Wie10].

cryostat are cooled to 90 K to prevent thermal electron-hole excitation. Behind the crystals is the cold part of the preamplifer which is in the same vacuum to minimise the noise contributions to the signals. The warm part of the preamplifier is located outside the vacuum for ease of accessibility [Wie10].

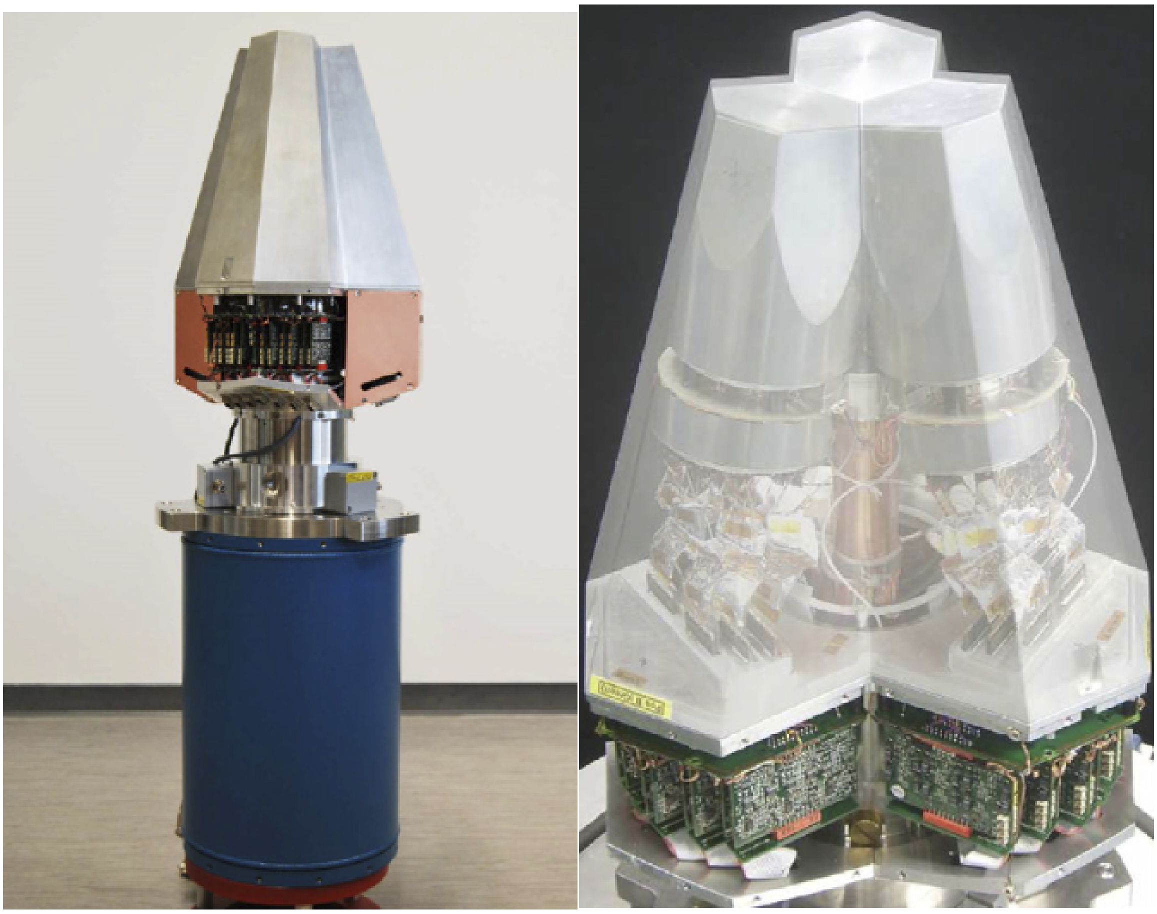

(a) (b)

Figure 3.3: (a) Part of the shielding is removed to show the inside the preamplifier housing. (b) A graphically altered image showing the alignment of the encapsulated crystals relative to the end cap. There is an internal spacing between the end cap of the encapsulated crystals of 0.5 mm [Wie10].

3.2 Pulse-shape analysis

3.2.1 Production of charge carriers

The interaction of gamma rays with matter was outlined in Section 2.3.1. The probability of a particular mechanism occurring is energy dependent. However in all cases electrons are liberated. The electrons lose energy by ionisation. This occurs within a small distance ($\sim$1 mm). The number of electron-hole pairs created is dependent on the incident gamma-ray energy and the ionisation energy (ϵ_{pair}) as given by,

$$N_{pair} = \frac{E_\gamma}{\epsilon_{pair}}, \tag{3.1}$$

where N_{pair} is the number of electron-hole pairs created, E_γ is the incident gamma-ray energy and, in Ge, ϵ_{pair} is ~3 eV [Kno00]. There is a statistical spread of electron-hole pairs created. This is corrected by the Fano factor [Fan47] given by,

$$\Delta N_{pair} = \sqrt{F N_{pair}} = \sqrt{F \frac{E_\gamma}{\epsilon_{pair}}}. \tag{3.2}$$

The Fano factor in Ge is ~0.08. This small value means the variance in the number of free electrons per event is small, leading to a smaller spread in energy. This results in excellent energy resolution [Kno00]. The collection of electron-hole pairs forms a signal. The factors that influence the signal are outlined below.

3.2.2 Signal generation

Electric field

A bias voltage is applied to collect the electron-holes pairs. In an AGATA detector the electrons drift to the positive core while the holes are attracted to the outer contact. The field strength at each point in the detector crystal can be calculated by solving the Poisson equation at each point;

$$\frac{d^2V(x)}{dx^2} = \frac{-\rho(x)}{\epsilon}, \tag{3.3}$$

where $V(x)$ is the electric potential, $\rho(x)$ is the charge density and ϵ is the dielectric constant of the detector material. The electric field determines the velocity and trajectory of the charge carriers. The influence of the electric field on the drift velocity can be calculated from,

$$v_d(x(t)) = \mu_{e,h} E(x), \tag{3.4}$$

where $\mu_{e,h}$ is the mobility of the electron and holes, $E(x)$ is the electric-field strength. The current induced in the detector is proportional to the field strength. The velocity of charge carries given by [Ram39],

$$i(t) = q\frac{E(x)v_d(x(t))}{V(x)}, \tag{3.5}$$

where $V(x)$ is the electric potential and v_d is the drift velocity [Ram39].

Weighting field

There is a Coulomb field which extends throughout the whole detector due to the cloud of charge carriers. The field covers each electrode of the detector. The applied electric field moves the charge carriers and as a result the Coulomb field changes with time. This change of Coulomb field is converted into current at the electrodes. As the field is non-homogeneous throughout the detector, the changes in induced current depends on the position of the charged particles. The weighting field is a normalised measure related to the induced current at each position within the detector. The induced current is calculated from,

$$-i(t) = -qE_w(x)v_d(x(t)), \tag{3.6}$$

where E_w is the weighting field and v_d is the drift velocity which is dependent on the electric field and electron-hole mobility. The weighting field is calculated from solutions of the Poisson equation for a unit voltage on the electrode of interest and the collected charge is calculated from,

$$Q = \int i(t)dt = -q\int_{x_2}^{x_1} E_w dl = q[v_w(x_1) - V_w(x_2)], \tag{3.7}$$

where $i(t)$ is the induced charge. Also x_1 and x_2 are the before and after position of charge carriers, respectively. The charge is proportional to the potential difference between the two points in the weighting field. This is the gradient of the weighting field [Sho38].

3.2.3 Parametric pulse-shape analysis

Parametric pulse-shape analysis utilises the shape of signals in order to extract position information. The first characteristic used is the type of signal induced. There are two signals produced; *real* and *transient*. A *real* signal is produced in the sector where the interaction took, therefore inducing a charge. As the Coulomb field extends throughout the detector volume, adjacent sectors from where the interaction took place show an effect of the interaction in the form *transient* signal. On collection the difference in weighting potential is zero, therefore *transient* signal do not induce any charge. The second characteristic is the time the charge carriers take to drift toward their collecting electrodes. Following an interaction in a sector charge carries are swept towards their corresponding electrodes in opposite directions. This induces a pulse as outlined in Section 3.2.2. This process occurs over a finite amount of time and the collection time is a function of the distance that the charge-carriers travelled. This is known as the *rise-time* of the signal. The electronic noise that is present in experimental data can result in difficulty locating the starting points of the signals. One way this problem can be overcome is to measure the signal to and from arbitrary points. An example is T30 to T90 *rise-time* calculations. T30 measures the *rise time* from 10% to 30% of the pulse height and T90 measures 10% to 90% of it. This is represented in Figure 3.4. T30 and T90 calculations can provide information on the interaction position in the sector because the shape of the rising edge is dependent on the distance between the interaction position and the contact in addition to the difference in the electron-hole velocities

3.2.4 Basis dataset pulse-shape analysis

In the AGATA project the pulse shapes of all electrodes are calculated for a set of well defined interaction points within a crystal. This calculation creates a pulse-shape basis dataset. The measured signals are compared to the calculated basis dataset to find the best fit [Ola05]. The pulse-shape algorithm finds the minimal χ^2 to define the interaction point.

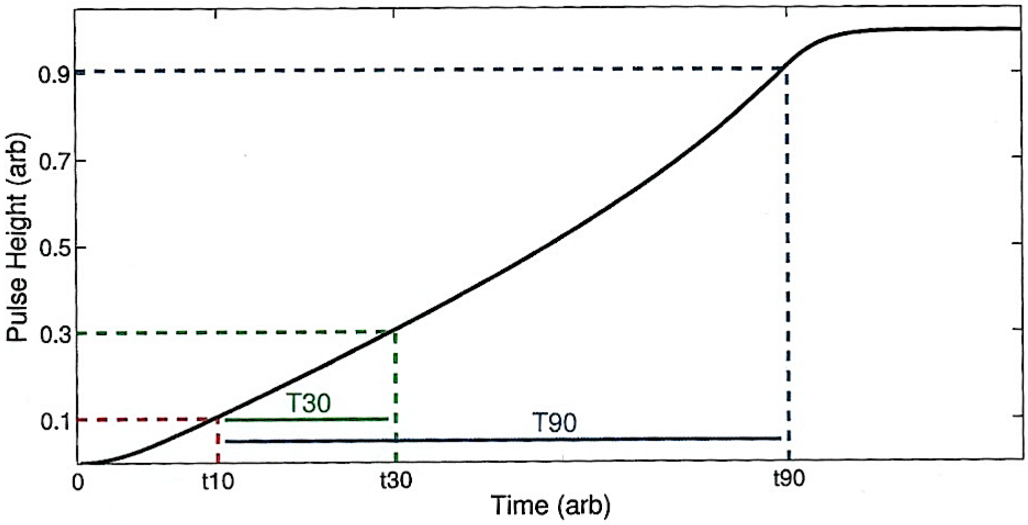

Figure 3.4: The *rise-time* can be measured from arbitrary points. The time between 10% and 30% (T30) and between 10% and 90% (T90) is shown here [Uns11].

JASS and ADL signal basis dataset

There are two methods of signal basis dataset; JASS (Java Agata Signal Simulation) [Sch09] and ADL (Agata Detector simulation Library) [Bru08]. The methods use the adaptive grid search technique which initially uses a coarse grid to find the point with minimum χ^2 between the reference and real signals. Upon localisation of this point, a finer grid is defined in the surrounding volume and the search is repeated. Both methods assume the same crystal orientation. This orientation is defined as the induced charge as a function of drift velocity. In Ge detectors the drift velocities of the charge carriers are dependent on the crystal plane through which they travel. However each method uses a different charge-carrier mobility which influences the calculated signal. Furthermore JASS calculates the pulse shapes on a 1 mm grid and ADL uses a 2 mm grid. The grid search algorithm reconstructs one interaction point per segment, which corresponds to the energy-weighted barycenter of all interaction positions in that sector. The basis dataset used in this work is JASS [Sch09].

3.2.5 Principles of gamma-ray tracking

The information extracted from the pulse-shape analysis algorithms is used to reconstruct the path that the gamma ray took. This is gamma-ray tracking. The Compton scattering equation is fundamental to all tracking calculations, Eq. 2.7. The Compton scattering angle (θ^{C}) can also be calculated from the following,

$$\cos\theta^{C} = \frac{\vec{x}_{\gamma}.\vec{x}_{\gamma'}}{|\vec{x}_{\gamma}|.|\vec{x}_{\gamma'}|}, \tag{3.8}$$

where $\vec{x}_{\gamma}$ and $\vec{x}_{\gamma'}$ are the interaction position of the incident and scattered gamma ray. The Compton scattering equation and Eq. 3.8 provide two independent methods in determining the angles from the same Compton-scattering process. For one event this should be the same. It is the comparison of these two values which can determine the correct scattering event and this is achieved by performing a least-squares minimisation of angle differences from the following equations (assuming N interaction sites, the final of which is absorption),

$$\chi^2 = \sum_{N-1}^{n=1} \left(\frac{\theta - \theta^{C}}{\sigma_{\theta}} \right)^2 . \tag{3.9}$$

In Equation 3.9, σ_{θ} is the error on the measures angle and it includes the uncertainty of the position determination and distance travelled by the gamma ray between two interaction points. The following outlines the key points of the calculation.

- It is assumed that the gamma ray is emitted from the source position.
- The calculation starts at the first interaction.
- The total gamma-ray energy is the sum of all energy deposited and this sum includes all up to the last interaction point.

This calculation uses a forward tracking method. It preliminarily identifies clusters of interaction points and all possible scattering angles within a cluster compared against the Compton scattering formula. The other method is backwards tracking. It looks for the final interaction and then reconstruct a track back to the original interaction point. This method allows, in principle, one to disentangle the interaction points of two gamma rays entering the detector very close to one another. Forward tracking is considered to be more accurate. Scatter events with approximately the same value χ^2 would indicate the same peak events and is dependent on the finite energy and position resolution of the detector. It follows that the tracking method is strongly dependent on the position resolution; a position resolution (full width half maximum) of 5 mm is required for an efficient method [Lop04].

3.3 Data-acquisition with AGATA

Processing the events from the detectors up to data storage is the principal purpose of the data-acquisition system (DAQ). The DAQ receives data from the crystals and processes them in four stages.

- Stage 1 - The data are transported to the preprocessing stage.
- Stage 2 - The gamma-ray interaction position (PSA), energy and time are calculated.
- Stage 3 - The tracking calculations are performed to reconstruct the gamma-ray tracks for the whole spectrometer.
- Stage 4 - The final stage merges the tracked data with a specific format and transfers it to storage.

3.3.1 Preprocessing

The front-end electronics (FEE) consists of a digitiser and a preprocessing system. It is the first stage of the chain of data-flow through the DAQ system. The FEE treats each crystal separately, forming a core signal from the superposition of the charges released by all the interactions in the 36 sectors of each crystal. The signal is used as a local trigger for the whole crystal in order to reduce the amount of data. Energy and

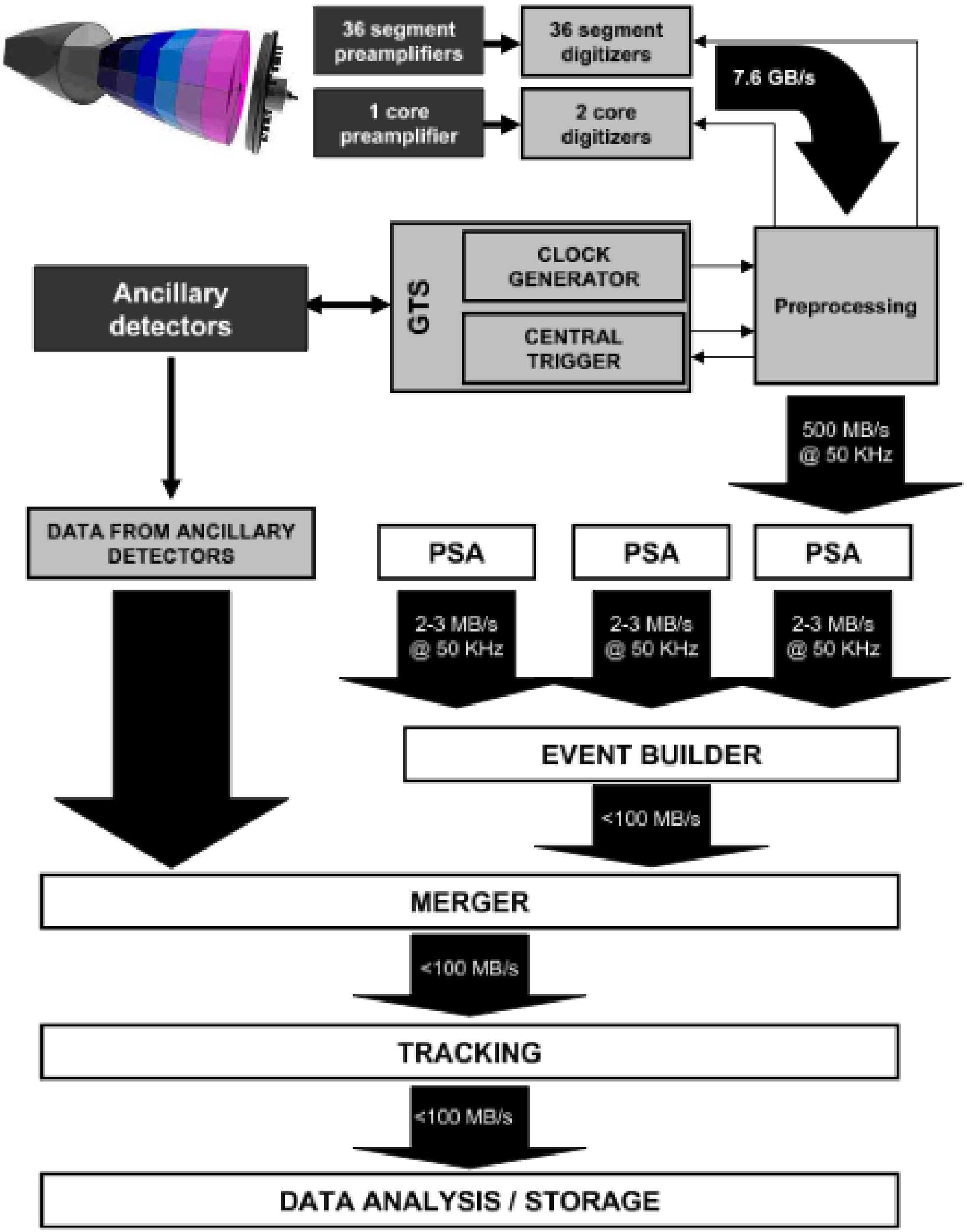

Figure 3.5: Schematic of the data-flow through the DAQ of AGATA. Data are received from the detectors and passed to the preprocessing stage. From here the data is analysed by the pulse-shape analysis algorithm where energy calibrations are performed. The tracking calculations are then performed. Finally, the data are transported to storage [Rec08].

time-stamp information are extracted before pulse-shape analysis is performed. In order to keep the relevant position information, the signals are digitised at a sampling frequency of at least 100 MHz, with a 14 bit analogue-to-digital converter (ADC). There is a rate of 50 kHz per crystal and this can result high data flux, too large to be stored and has to therefore to be analysed in real time in order to extract the useful physical information. All of the digitisers work synchronously by receiving their 100 MHz clock and a time stamp from a central clock generator (the Global Trigger and Synchronisation, GTS). Each crystal is treated as an independent entity in order to extract the useful information for each detected signal. The signal-processing algorithms are implemented in powerful highly-parallel FPGAs (Field Programmable Gate Array) [Kor01] [Rec08].

3.3.2 Pulse-shape analysis

The event configuration for each hit in a detector is determined. For each hit sector the algorithm will determine the number of interactions that took place within a detector and the interaction positions, as described in section 3.2. Following this the data are transported to the event builder [Kor01].

3.3.3 Data-flow software

The data-flow and processing that has been outlined, is carried out using Nouvelle Acquisition temps-Réel Version 1.2 Avec Linux (NARVAL) and it is an object-orientated distribution software written in Ada95 [Ada95]. The system is comprised of separate blocks of actions, called *actors*. Each one contains a self-sufficient piece of code designed for a specific action. There are three different types of *actors*:

- Producer - This is used to read in data from the electronics or disk.
- Filter - This conducts the operations on the data - pulse-shape analysis, data merging and gamma-ray tracking.

- Consumer - This is the final stage of the data flow, this is where the data are written to disk [Gar05].

3.4 Accessing AGATA data

Data generated by the AGATA spectrometer will be stored on the GRID.[1] Grid technologies allow computers to share through the internet or other telecommunication networks not only information, but also computing power (Grid computing) and storage capacity (Grid data). Data will be located at the storage sites of INFN-CNAF Tier-1 in Bologna and CC-IN2P3 Tier-1 in Lyon. To access and download data an X509 certificate is required. This certificate can only be issued by a GRID Certification Authority (CA). To obtain a certificate the user must prove their identify and provide a valid reason for accessing the data. Furthermore the user must be a member of the AGATA virtual organisation [Kac11].

3.5 Detector operational characteristics

The performance of gamma-ray detectors can be measured quantitatively using energy resolution and counting efficiency.

3.5.1 Efficiency

The efficiency of a Ge detector can be measured by one of the following methods:

- Absolute efficiency (ϵ_{abs}). This is dependent on the detector properties and counting geometry. It is the ratio of detected counts to the number emitted by the source. It is dependent on the source-to-detector geometry.

---

[1] The GRID is a set of information resources, for example computers, databases, networks, instruments that are integrated to provide users with tools and applications that treat those resources as components within a *virtual system.*

- Intrinsic efficiency (ϵ_{int}). This is the ratio of the number of detected events to the number of photons incident on the detector.

- Relative efficiency (ϵ_{rel}). The efficiency of a Ge detector relative to a 76mm in diameter and 76mm in length, NaI(Tl) crystal using a ^{60}Co source placed 250mm from the crystal. The relative efficiency is normally measured for an energy of 1.33 MeV [Kno00].

3.5.2 Energy resolution

The intrinsic energy resolution of a detector, ΔE_i, is calculated by adding, in quadrature, contributions from the statistical, detector and electronic noise contributions as,

$$(\Delta E_i)^2 = (\Delta E_D)^2 + (\Delta E_X)^2 + (\Delta E_E)^2. \tag{3.10}$$

- ΔE_D accounts for the inherent statistical fluctuation in the number of charge carriers created by an interaction and is given by,

$$\Delta E_D = 2.35\sqrt{\frac{F}{N_{pair}}}. \tag{3.11}$$

- ΔE_X represents the variations due to charge losses. In semi-conductors this accounts for problems with incomplete charge collection

- ΔE_E accounts for the electronic noise that results from the electronic components

Energy resolution is measured at the Full Width at Half the Maximum height (FWHM) of the photopeak. When accelerated beams ($\beta = v/c$) are used for experiments, the residual nucleus emits gamma rays moving with a velocity that is a fraction of the speed of light. The detected energy, E_γ, will be Doppler shifted to,

$$E_\gamma = E_{\gamma 0}\sqrt{1-\beta^2}\left(\frac{1}{1-\beta^2 cos\theta_\gamma}\right), \tag{3.12}$$

where $E_{\gamma 0}$ is the true energy and θ_γ is the photon emission angle relative to the trajectory of the recoiling nucleus. For a finite detector opening angle ($\Delta\theta_\gamma$), the observed photon energy is broadened by,

$$\frac{\Delta E_\gamma}{E_\gamma} = \left(\frac{\beta sin\theta_\gamma}{1 - \beta cos\theta_\gamma} \right) \Delta\theta_\gamma. \tag{3.13}$$

When calculating total photopeak FWHM (ΔE_γ) for a detector configuration using accelerated beams both intrinsic (ΔE_i) and Doppler effects must be taken into account. This is calculated from,

$$\Delta E_\gamma = \sqrt{\Delta E_i^2 + \Delta E_\theta^2 + \Delta E_\phi^2 + \Delta E_v^2}, \tag{3.14}$$

where ΔE_θ, ΔE_ϕ and ΔE_v are the contributions to Doppler broadening resulting from the opening angle of the detector, the angular spread of the recoils, and the velocity spread of the recoils, respectively [Kno00].

Chapter 4

Experimental details and data analysis methodology

4.1 Summary of the commissioning experiments of AGATA spectrometer

The physics campaign of the AGATA project commenced in February 2010. Prior to this there was a series of commissioning experiments performed at Laboratori Nazionali de Legnaro to ensure this campaign was successful. The following section summarises the commissioning experiments, starting February 2009, undertaken and the associated experimental objectives.

4.1.1 The test of a triple cluster with a radioactive source

This experiment took place in February 2009 with one triple cluster. The main aims were to test different constituents of the AGATA system. They were the front-end electronics, data-acquisition system and GUI[1]. Also tested was the auto-fill system and the mechanical support.

---

[1] **G**raphical **U**ser **I**nterface

4.1.2 The first in-beam test of a triple cluster

This experiment was carried out in March 2009 and the main aims were.

- The testing of an AGATA triple cluster in real experimental conditions.
- Testing of the data-acquisition system.
- Measuring the effective position resolution provided by the pulse-shape analysis algorithms.

To determine the effective position resolution the Doppler broadening at two different target-to-detector distances were measured. By varying the distance all contributions to the Doppler broadening will be the same apart from the contribution of the opening angle of the detector. Position resolution is deduced from this. The Doppler broadening was maximised by mounting an AGATA triple cluster at approximately 90° and by using a reaction with a large recoil velocity. The experimental set-up is shown in Figure 4.1. In order to achieve this a heavy-ion fusion-evaporation reaction was chosen, using inverse kinematics. A beam of ^{30}Si at 70 MeV was incident upon a thin target (216 μg/cm^2) of ^{12}C. Recoiling reaction products were stopped by placing 16 mg/cm^2 thick foils 2 mm downstream of the target. Pulse-shape analysis and gamma-ray tracking were performed on-line. The data acquisition system was run in a trigger-less mode and data was stored offline for further analysis, if necessary.

4.1.3 The in-beam test of a triple cluster with a a simple ancillary detector

This experiment was carried out in July 2009 and the main aims were.

- To show the feasibility to couple a simple ancillary detector to the AGATA demonstrator.
- To test the digital trigger-processor which validates the events and assigns the event number.

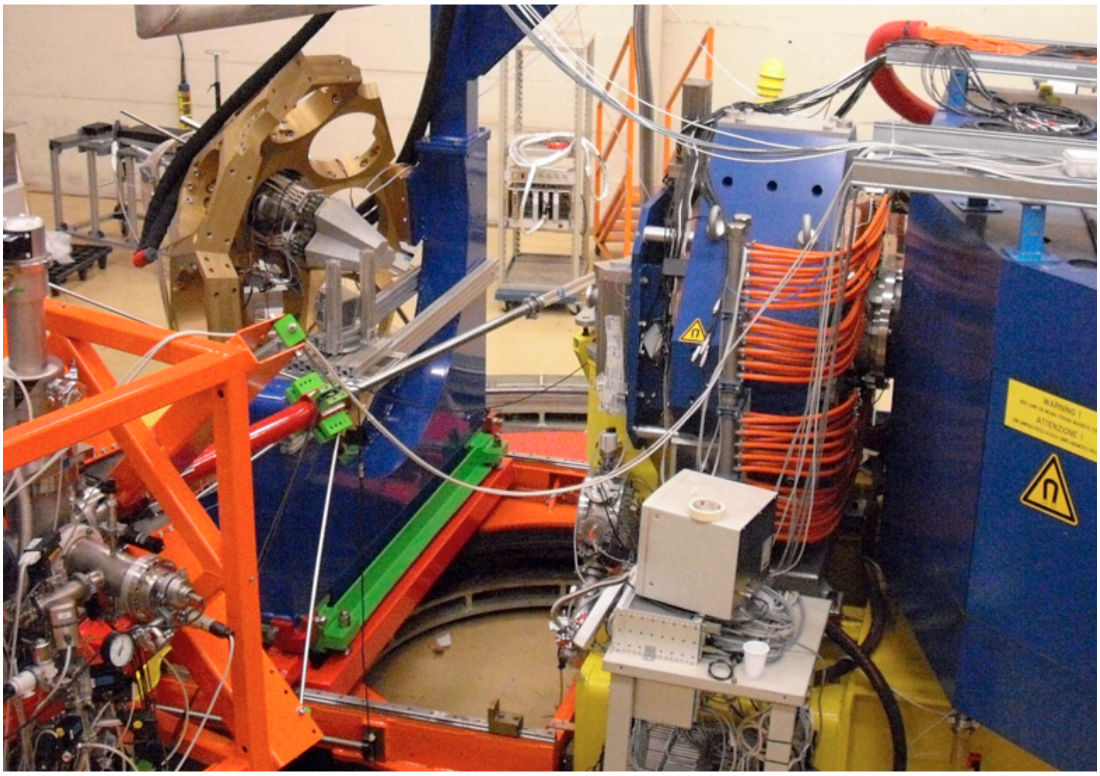

Figure 4.1: An AGATA triple cluster is shown in the AGATA holding frame at approximately 90° to the beam line. The beam line is in front of the AGATA triple cluster.

The ancillary detector chosen was DANTE,[2] a multi-channel plate detector. The experimental setup is shown in Figure 4.2. A beam of ^{56}Fe at 220 MeV (Coulomb excitation), from the LNL tandem accelerator was incident on a thin target of ^{197}Au. The energy resolution of the $2^{+}\rightarrow 0^{+}$ transition in ^{56}Fe (854 keV) was measured. DANTE was used to detect the scattered ^{56}Fe ions and allowed for a kinematic Doppler-correction to be performed. Data from the AGATA triple cluster were analysed online using NARVAL (Section 3.3). Data from DANTE were analysed offline due to an online code being unavailable at this time. There was an improvement in energy resolution from 30 keV to 4.6 keV observed when carrying a kinematic Doppler-correction.

---

[2] **D**etector **A**rray for multi-**N**ucleon **T**ransfer **E**jectiles

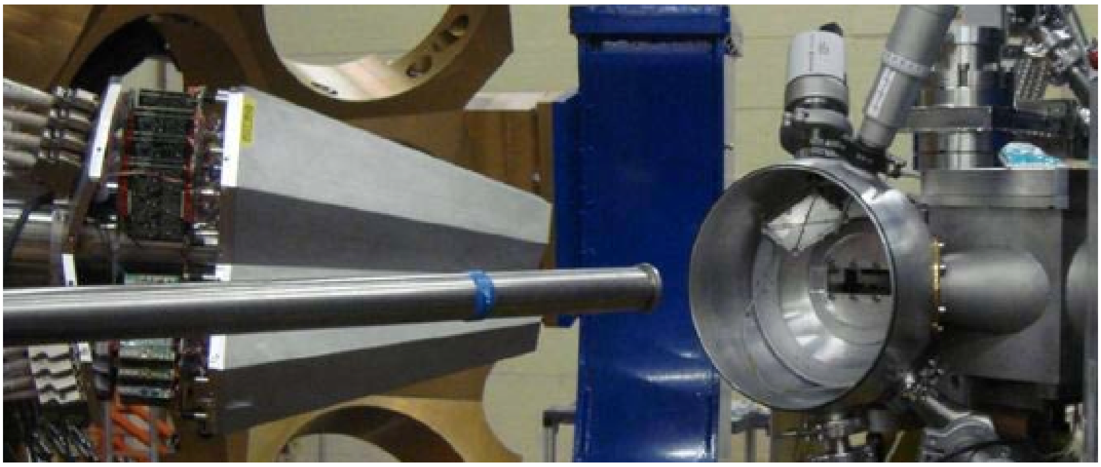

Figure 4.2: The experimental setup of the commissioning experiment performed in July 2009. There was one AGATA triple cluster and DANTE, a multi-channel plate detector. This detector can be seen inside the target chamber. The beam direction is coming from the left side.

4.1.4 The in-beam test of multiple triple clusters

This experiment was carried out in October 2009. It used a heavy-ion fusion-evaporation reaction ^{110}Pd (^{32}S,4n) ^{138}Sm at 135 MeV. Details of this commissioning experiment are given in Section 4.2.

4.1.5 The in-beam test of two triple clusters with the PRISMA spectrometer

There were two experiments carried out in November and December 2009 to test the coupling of two triple cluster to the PRISMA magnetic spectrometer via the AGAVA[3] interface. The reaction for experiments was the same; multi-nucleon transfer of a ^{58}Ni beam at 235 MeV incident on a thin target of ^{96}Zn. PRISMA consists of three detectors; the entrance detector based on micro-channel plates (MCP), a multi-wire parallel-plate avalanche counter (MW-PPAC) detector and an ionisation chamber

---

[3] AGAVA is the interface between the ancillary detector electronics/acquisition and the AGATA Global Trigger and Synchronisation (GTS) system. It provides the time stamp and event number.

(IC) at the focal plane. The entrance detector is based on a large-area MCP in a chevron configuration. This provides time and position signals. The MW-PPAC is at the focal plane with the IC 50 cm away from it. The IC provides the energy signals for the identification of the atomic number of the fragments [Fio10].

First test

The first set-up consisted of two triple clusters with DANTE and the PRISMA magnetic spectrometer coupled through the AGAVA interface. Unfortunately there were many technical problems resulting in low statistics. However due to the fact statistics were collected suggested that the coupling, performed through the AGAVA interface, was working.

Second test

The aim of the second experiment was the optimisation of the on-line PRISMA analysis, and to collect more data to investigate the performance of the AGATA-PRISMA coupling. From this experiment it was shown that the on-line PRISMA analysis was possible.

4.2 Experimental details

Data obtained from the heavy-ion fusion-evaporation reaction ^{110}Pd (^{32}S,4n) ^{138}Sm at 135 MeV were used to determine the Compton polarimetry capability of an AGATA triple cluster. The experiment was performed in October 2009, and was one of a series of this commissioning experiments. The aims of the commissioning experiment were.

- For the first time test two asymmetric triple-clusters in coincidence.
- To couple the asymmetric triple-clusters to ancillaries using the AGata Ancillary VME Adaptor (AGAVA) interface.
- To test the asymmetric triple-clusters with high multiplicity gamma-ray data.

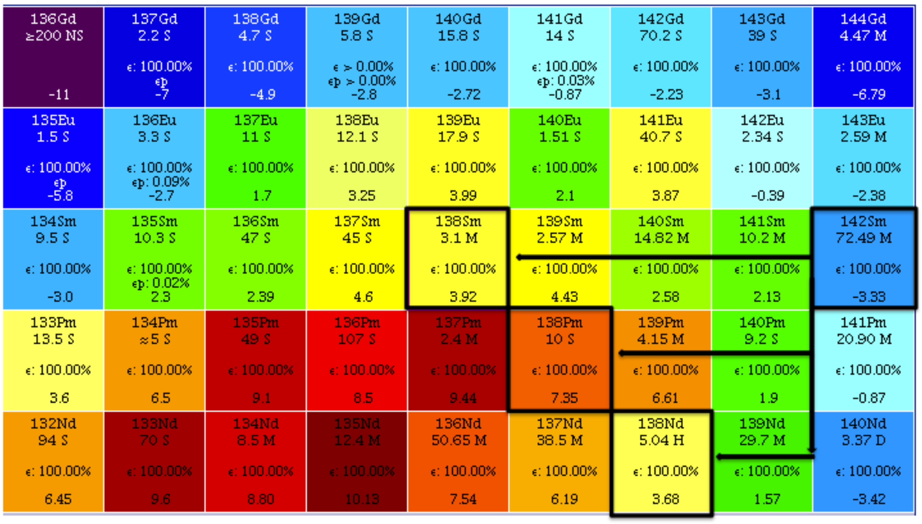

136Gd ≥200 NS -11	137Gd 2.2 S ϵ: 100.00% ϵp -7	138Gd 4.7 S ϵ: 100.00% -4.9	139Gd 5.8 S ϵ > 0.00% ϵp > 0.00% -2.8	140Gd 15.8 S ϵ: 100.00% -2.72	141Gd 14 S ϵ: 100.00% ϵp: 0.03% -0.87	142Gd 70.2 S ϵ: 100.00% -2.23	143Gd 39 S ϵ: 100.00% -3.1	144Gd 4.47 M ϵ: 100.00% -6.79
135Eu 1.5 S ϵ: 100.00% ϵp -5.8	136Eu 3.3 S ϵ: 100.00% ϵp: 0.09% -2.7	137Eu 11 S ϵ: 100.00% 1.7	138Eu 12.1 S ϵ: 100.00% 3.25	139Eu 17.9 S ϵ: 100.00% 3.99	140Eu 1.51 S ϵ: 100.00% 2.1	141Eu 40.7 S ϵ: 100.00% 3.87	142Eu 2.34 S ϵ: 100.00% -0.39	143Eu 2.59 M ϵ: 100.00% -2.38
134Sm 9.5 S ϵ: 100.00% -3.0	135Sm 10.3 S ϵ: 100.00% ϵp: 0.02% 2.3	136Sm 47 S ϵ: 100.00% 2.39	137Sm 45 S ϵ: 100.00% 4.6	138Sm 3.1 M ϵ: 100.00% 3.92	139Sm 2.57 M ϵ: 100.00% 4.43	140Sm 14.82 M ϵ: 100.00% 2.58	141Sm 10.2 M ϵ: 100.00% 2.13	142Sm 72.49 M ϵ: 100.00% -3.33
133Pm 13.5 S ϵ: 100.00% 3.6	134Pm ≈5 S ϵ: 100.00% 6.5	135Pm 49 S ϵ: 100.00% 9.1	136Pm 107 S ϵ: 100.00% 8.5	137Pm 2.4 M ϵ: 100.00% 9.44	138Pm 10 S ϵ: 100.00% 7.35	139Pm 4.15 M ϵ: 100.00% 6.61	140Pm 9.2 S ϵ: 100.00% 1.9	141Pm 20.90 M ϵ: 100.00% -0.87
132Nd 94 S ϵ: 100.00% 6.45	133Nd 70 S ϵ: 100.00% 9.6	134Nd 8.5 M ϵ: 100.00% 8.80	135Nd 12.4 M ϵ: 100.00% 10.13	136Nd 50.65 M ϵ: 100.00% 7.54	137Nd 38.5 M ϵ: 100.00% 6.19	138Nd 5.04 H ϵ: 100.00% 3.68	139Nd 29.7 M ϵ: 100.00% 1.57	140Nd 3.37 D ϵ: 100.00% -3.42

Figure 4.3: An edited chart of nuclides showing the location of the nuclides formed during the reaction. The compound nuclei is ^{142}Sm. ^{138}Sm is formed from 4n evaporation.^{138}Pm is formed from p3n and ^{138}Nd from 2p2n evaporation.

In order to achieve the high gamma-ray multiplicity the previously studied reaction, given above, was used. A beam of ^{32}S at 135 MeV, from the LNL tandem XTU accelerator, was incident on a target of ^{110}Pd which produced a compound nucleus of ^{142}Sm. The target thickness was 500 μg/cm^2 The main exit channels were,

- ^{138}Sm (4n evaporation),
- ^{138}Pm (p3n),
- ^{138}Nd (2p2n).

The recoil velocity was determined experimentally to be 2.30±0.01% of the speed of light. This was by varying v/c and measuring the energy resolution of the 346 keV $2^+ \rightarrow 0^+$ transition of ^{138}Sm. Doppler corrections made the assumption that all the recoils forward scattered at θ=0°. Two AGATA triple clusters were placed in the

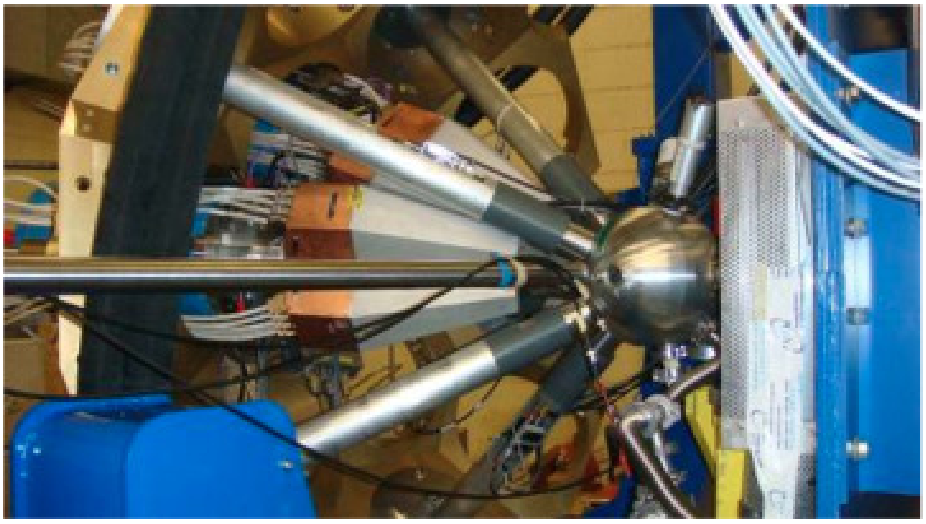

Figure 4.4: The experimental setup is shown here. The beam is coming in from the left and the target chamber (metal sphere) is on the right. The two AGATA triple clusters are also shown and are at 80° to the beam line.

AGATA support frame at 80° to the beam line. The experimental setup is shown in Figure 4.4. The following detectors formed the triple clusters; A001, B002, C002 (triple cluster one) and A003, B003, C005 (triple cluster two). The cryostats of the triple clusters in the AGATA support frame can be seen in Figure 4.5. The triple clusters were used in conjunction with five $LaBr_3$ scintillators and a 300 μm silicon detector with 16 resistive strips. As previously stated this was to test the AGAVA interface and does not form part of the data analysis. The reaction was heavy-ion fusion-evaporation (Section 2.1) and the resulting nuclide are in an aligned state. As a result the Compton polarimetry capability of the triple clusters can be determined. For the purpose of this work the capability will be determined using one triple cluster. There was more useable data available for triple cluster two and for this reason this triple cluster was chosen.

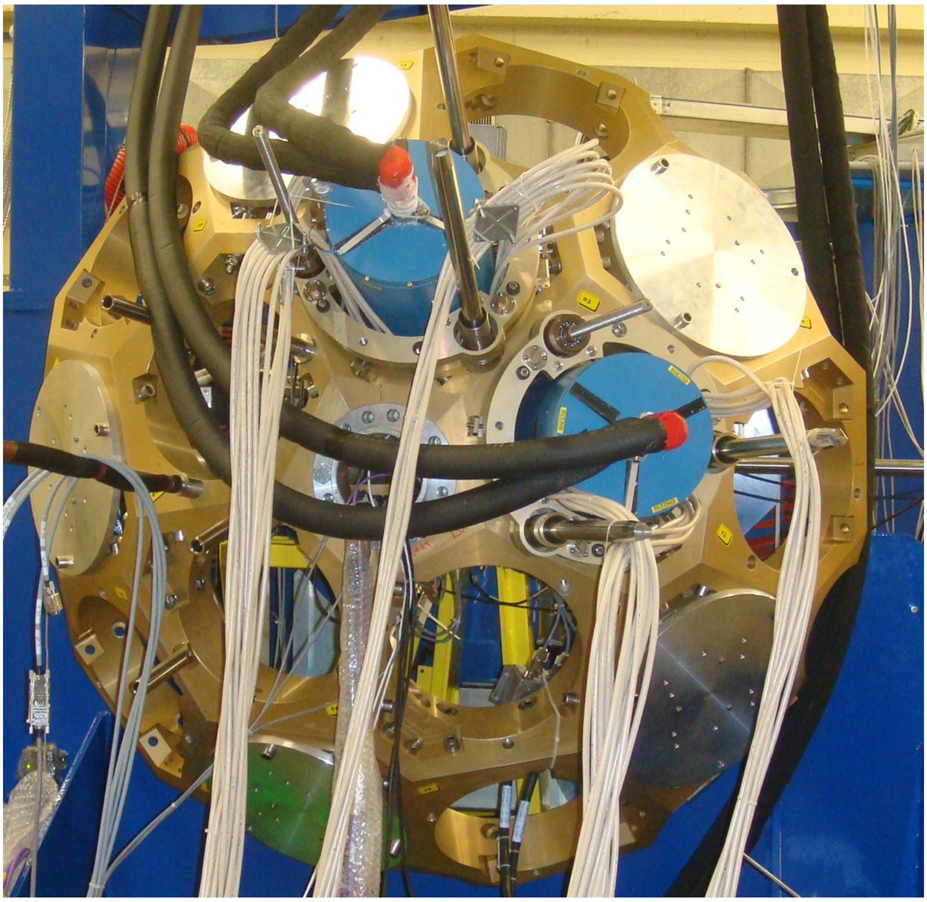

Figure 4.5: In this picture the single cryostat for each triple cluster can be seen. This is half of the support frame that will ultimately house all 60 triple clusters.

4.3 Processing AGATA data

Details of the NARVAL data-acquisition system which is used during experiments were outlined in Section 3.3. When it is necessary for data to be replayed after an experiment has been performed, this can be achieved through the NARVAL-emulator. The NARVAL-emulator is essentially the same as the version used during experiment except the actors are written in C++. This difference in the language it is written in allows the users to manipulate the outputs into the format of their choice.

4.4 Different stage of data processing

Each actor is performed sequentially from the first one, to the last one in the data-flow path as defined in *Topology file* (section 4.6.1). The following sections (4.4.1-4.4.4) are listed in the order that data are processed in the NARVAL-emulator.

4.4.1 Producer stage

The *producer actor* starts the data processing. First it loads all needed libraries for the replay of the experiment. Next data are read from a previously defined location and this data passed to the *preprocessing actor*. Data here is uncalibrated, ungain-matched and non Doppler-corrected.

4.4.2 Preprocessing stage

The data at this stage are gain matched, calibrated and have cross-talk corrections applied. Cross-talk is a signal alteration that is inherent to segmented detector. It is due to conductive or capacitive coupling between the detectors electrodes. The different couplings of the sector preamplifiers to the detector result in sector-to-sector and sector-to-core cross-talks contributions being an of order of magnitude smaller than the core-to-sector cross-talk. There are two types of cross-talk; proportional and differential. Proportional cross-talk is directly proportional to the signal amplitude. There is a net flow of charge from the hit sector to another sectors. The resulting measured energy is smaller than the amount deposited. Differential cross-talk is proportional to the derivative of the induced charge signal and contributes to the signal shape only during the rise-time of the signal. This type of cross-talk only affect neighbouring sectors. This resulting shape is similar to that of a transient signal which makes experimental signals hard to measure. This effect has yet to be included into pulse-shape analysis algorithms [Sch09].

- The gain matching and calibration is performed by the *Preprocessing actors*. There are gain coefficients defined for each crystal in *PreprocessingFilterPSA.conf* which are applied to the data.

- A similar process is carried out for proportional cross-talk corrections. The cross-talk coefficients for each crystal are defined in *xinv_1325-1340.cal* and are applied to the data.

4.4.3 Pulse-shape analysis stage

At this stage pulse-shape analysis is carried is performed and the data is Doppler corrected.

- Pulse-shape analysis is carried out by the *PSAfilter*. It performs a χ^2 minimisation between the basis datasets and the experimental data to find the interaction positions of the gamma rays. The pulse-shape analysis algorithm utilised an energy-weight barycentre method. For a given sector where there are two interactions with a given distance the algorithm will not be able to distinguish and will treat it was one interaction. The energy for this interaction will be the sum of the the two energies and it will be located at the energy-weighted barycentre.

- Doppler correction is also carried out by the *PSAFilter*. The first interaction point in the scattering sequence is chosen on the basis of energy considerations. The angle of emission is obtained from the reaction kinematics and the position of the first interaction point.

4.4.4 Tracking stage

Gamma-ray tracking is carried out by the *tracking actor* utilising the Orsay Forward Tracking Code (OFT). The principles of gamma-ray tracking was introduced in section 3.2.5. Forward tracking involves identifying clusters of interaction points and all possible scattering angles within a cluster and comparing against the Compton scattering formula. In addition to this a file known as *OftHits* is created. It contains all the interaction position for all gamma-ray interactions, the number of times the gamma ray interacted, the coordinates of each interaction, the time stamps, number of counts for the interacting gamma ray. An example of an *OftHits* file is shown in Appendix C9.

4.5 Spectra for ^{138}Sm

Spectra can be produced for the various stages of the data processing. For this work it was decided the format would be ROOT [Roo95]. To output spectra at *producer*, *preprocessing* and *pulse-shape analysis* stages each of the actors were implemented with a ROOT output. It was also necessary to ensure that the NARVAL-emulator would write out the traces. The option to write traces is in the configuration files (Section 4.6.1). The new ROOT outputs allow spectra to be constructed. Figures 4.6-4.9 are the produced spectra, for one AGATA triple cluster, for the various stages of the data processing through the NARVAL-emulator. The total projection spectrum in Figure 4.6 is consistent with expectation as an output from the *producer actor*. That is, it is uncalibrated/non gain-matched and non Doppler-corrected because the *producer actor* reads in and passes the data to the *preprocessing actor*. Each of the spectrum that have been produced from the *preprocessing* and *pulse-shape analysis actor* are again consistent with expectation. Figure 4.7 (*preprocessing*) and Figure 4.8 (*pulse shape analysis*) have similar features. This is due the the calibration/gain matching being carried out at the *preprocessing* stage. This only difference is that after pulse-shape analysis, Doppler correction has been performed.

4.6 NARVAL-emulator usage

The NARVAL-emulator can be installed on a computer of the user's choice as it is operating-system free. The most recent installation guide (written by Laboratori Nazionali de Legnaro) is given in Appendix C1. It outlines the necessary pre-requisite libraries that must be downloaded prior to installation of the NARVAL-emulator. The

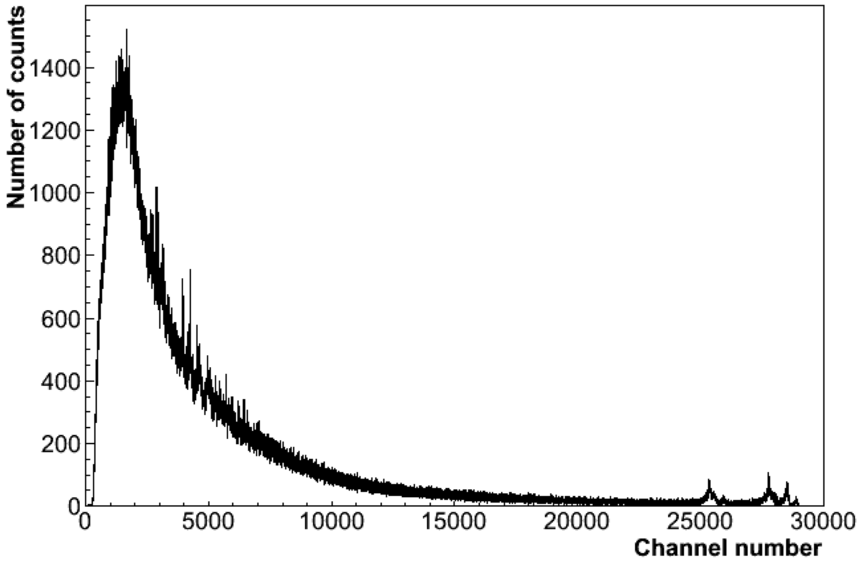

Figure 4.6: A ROOT output from the *producer actor* of the total projection spectrum of ^{138}Sm for a triple cluster. The spectrum here is uncalibrated/non gain-matched and non Doppler-corrected

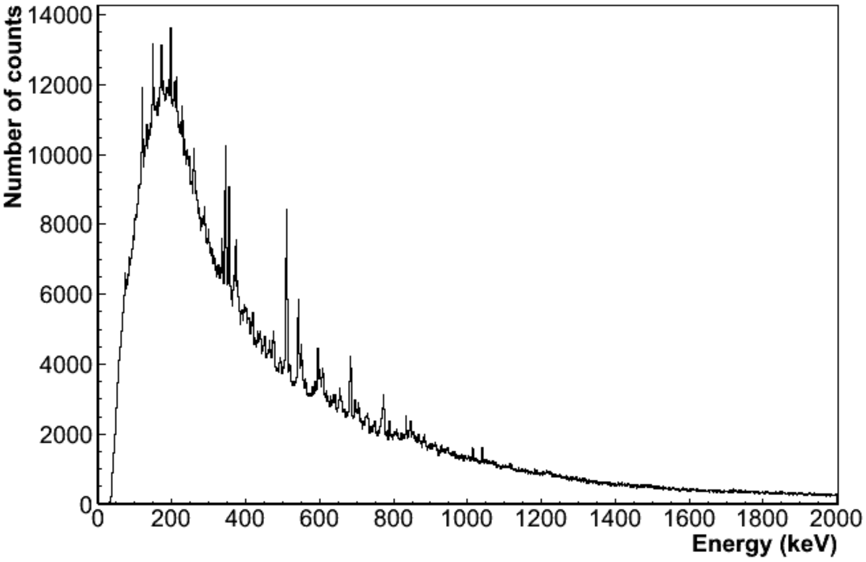

Figure 4.7: A ROOT output from the *preprocessing actor* of the total projection spectrum of ^{138}Sm for a triple cluster. The spectrum here is calibrated/gain matched but still non Doppler-corrected

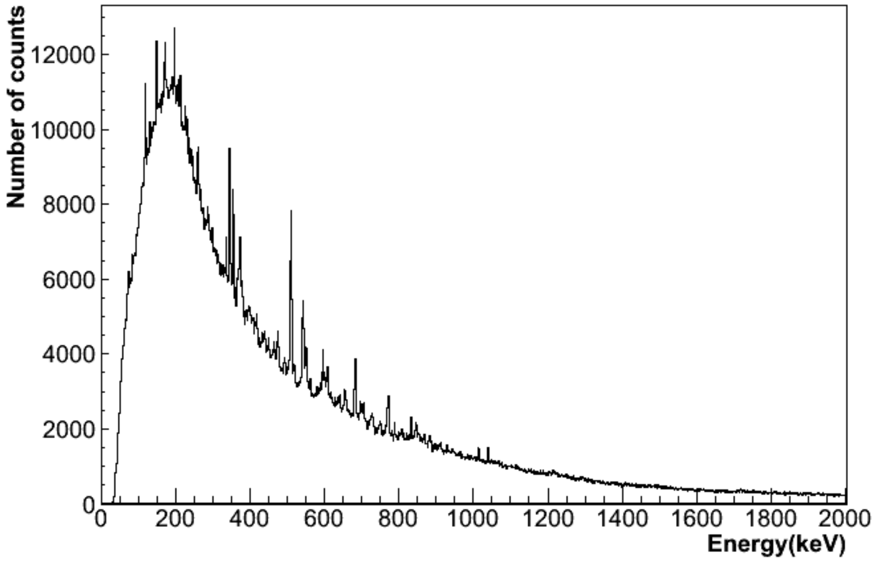

Figure 4.8: A ROOT output from the *pulse-shape analysis actor* of the total projection spectrum of ^{138}Sm for a triple cluster. The spectrum here is calibrated/gain matched and Doppler corrected.

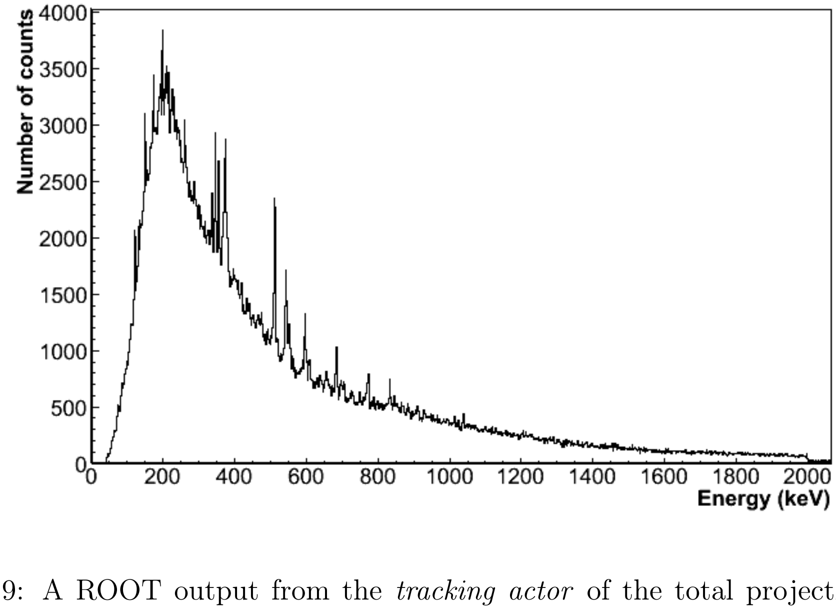

Figure 4.9: A ROOT output from the *tracking actor* of the total projection spectrum of ^{138}Sm for a triple cluster. The spectrum here is calibrated/gain matched, Doppler corrected and tracked.

main executable file is known as *WinCtest*. This is located in the *WinCtest* folder. In Section 3.4 the method to download AGATA data from *The Grid* was outlined. The data for a complete experiment will consist of a series of folders, the structure of which in shown in *TemplateDir* within the installed version of the NARVAL-emulator. The subfolder *Data* contains the experimental data. Within *TemplateDir* there is also *Conf_ offline* and *Conf_ online* folders. These refer to the offline and online analysis, respectively. The offline version must be used with the NARVAL-emulator. Within *Conf_ offline* there are subfolders for each crystal. Within these folders there are a set of configuration files which must be individually edited in order to replay the experiment. This section will outline how each file must be configured for each crystal folder. The first step is to download the basis datasets for each colour crystal. They should be placed in a folder together. The name of the folder is the user's choice. In this method this folder will be referred to as *Bases*. The next stage is to create folders for outputted data to be written to. Normally a folder for each crystal is created and within this, subfolders created for *Preprocessing*, *Pulse-shape analysis* and *Tracking*.

4.6.1 Configuration files editing instructions

In order to replay data through the NARVAL-emualtor the user must edit a series of configuration files. This section will outline what configuration files should edited. Example of each configuration file is given in Appendix C. The following summarises the location of the example file in the Appendix.

- CrystalProducer.conf - Appendix C2
- CrystalProducerATCA.conf - Appendix C3
- PSAFilter.conf - Appendix C4
- PreprocessingFilter.conf - Appendix C5
- TrackingFilter.conf - Appendix C6
- The topology file - Appendix C7

- Event builder - Appendix C8

CrystalProducer.conf

To edit this file the user must input the location of the experimental data and where the output data is to written to.

CrystalProducerATCA.conf

The only edit to this file the user must perform it to change the location of the experimental data. This is done by changing the location on the following line of the file,

```
file 0 7 Data/1G/event_mezzdata.bdat
```

Furthermore the user can chain a number of data files together by increasing the value in the second column from 0 to, for example, 2 if there are two additional data files. It is important to note that if the names of the data files are different to what is shown in Appendix C3 and this should be reflected in the path name.

PSAFilter.conf

To edit this file the user must input the location of the basis datasets and where the output data is to be written to.

PreprocessingFilter.conf

To edit this file the user must input the location to where the output data is to be written to.

TrackingFilter.conf

There is only one file for all the crystals within the *Conf_ offline.* To edit this file the user must input where the output data is to written.

Event builder

This file builds the events. The user can set a minimum fold of the event here.

The topology file

The topology file runs and chains together all the configuration files. The user can choose how many crystals to run by commenting out crystals which are not required. To run the NARVAL-emulator the user must be in the directory that contains the *Topology file*. To execute *WinCtest* input the location of this executable and the input the name of the *Topology file*. The NARVAL-emulator will process all the data which was inputted into *CrystalProducerATCA.conf* and output in the location the user specifies.

4.7 Calibration of an AGATA triple cluster

Energy calibrations were performed using ^{133}Ba. A core, tracked calibration spectrum for each crystal; blue, green and red is shown in Figure 4.10-4.12, respectively. Furthermore a calibration spectrum for the triple cluster is shown in Figure 4.13. It can be seen from Figure 4.11 (green crystal) and Figure 4.12 (red crystal) that there are X-rays present. These X-rays are also present in the total spectrum, Figure 4.13. However, the X-rays are not seen in Figure 4.10 (blue crystal). This could be due to a higher threshold set on the DAQ for the channels in the blue crystals than the green or red. Furthermore, in Figure 4.11 there appears to be dips after 81.0 and 356 keV. The background immediately after the peak could be at the right level for $\sim$10 keV and then there is an additional background contribution. The background level immediately after the 81 keV peak in Figure 4.10, 4.12 and 4.13, is at the same level as the background just after the 53.2 keV peak. This is the same in Figure 4.11, but then there is an extra background around 10 keV after this peak. A similar effect can be seen after the 302.9 and 356.0 keV peaks. This could be a Compton edge. The X-rays in Figure 4.11 are much more stronger than in Figures 4.10, 4.12, 4.13. The

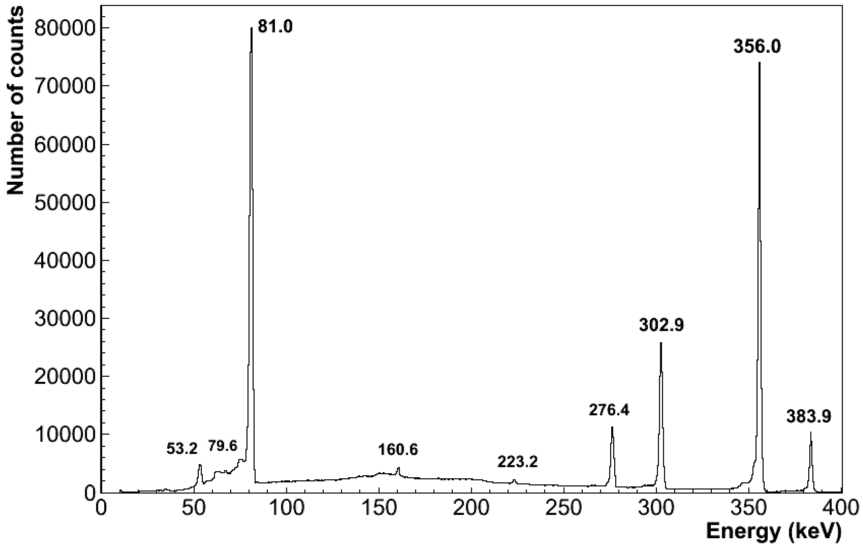

Figure 4.10: Tracked calibration spectrum of ^{133}Ba for the blue crystal. The energies of ^{133}Ba are shown.

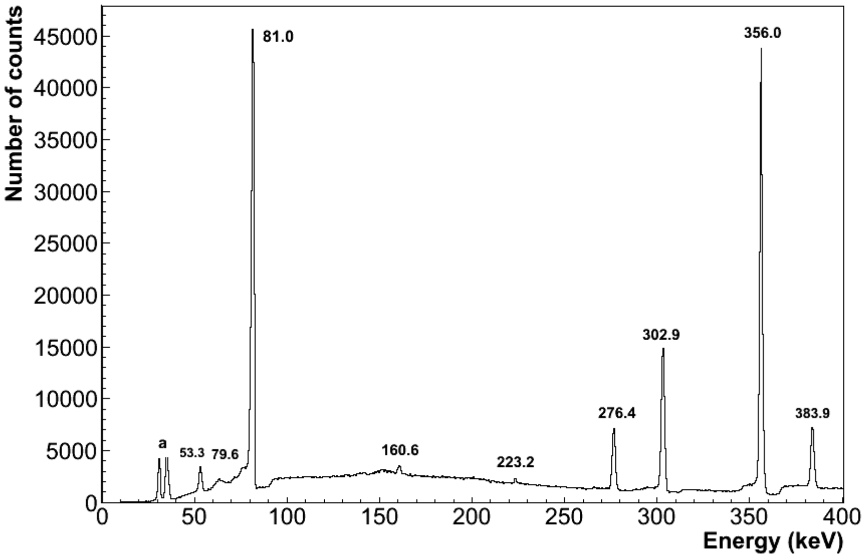

Figure 4.11: Tracked calibration spectrum of ^{133}Ba for the green crystal. The energies of ^{133}Ba are shown. In addition there are additional X-rays peaks shown here (labelled a).

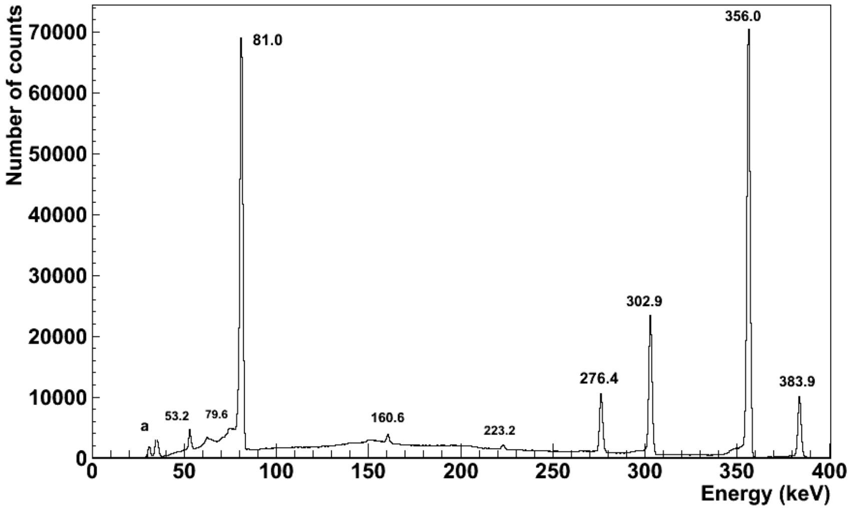

Figure 4.12: Tracked calibration spectrum of ^{133}Ba for the red crystal. The energies of ^{133}Ba are shown. In addition there are additional X-rays peaks shown here (labelled a).

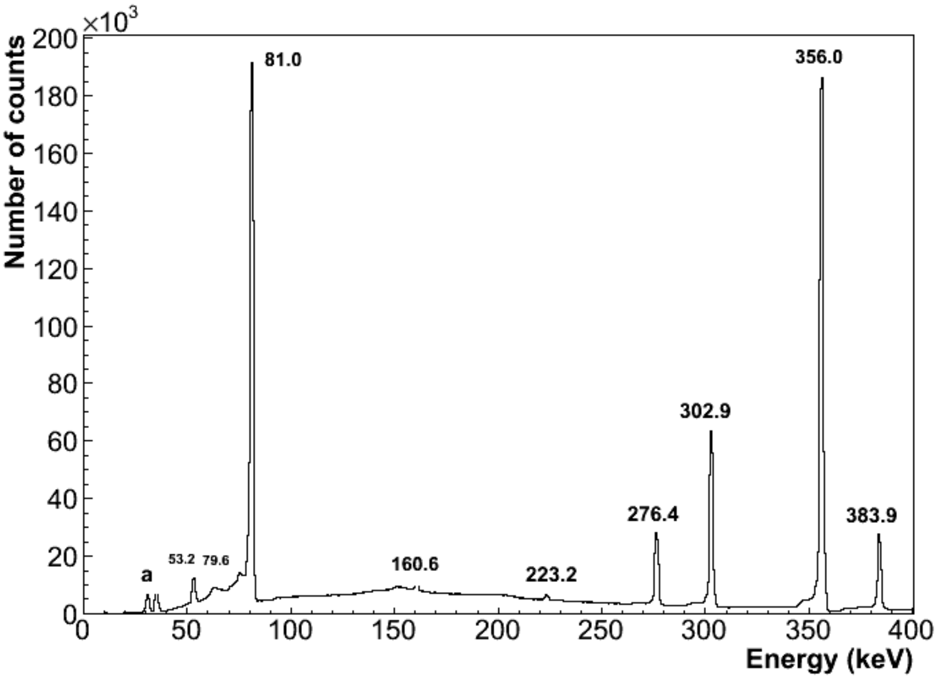

Figure 4.13: Tracked calibration spectrum of ^{133}Ba for the triple cluster. This is a sum spectrum of the blue, green and red crystals. The energies of ^{133}Ba are shown. In addition there are additional X-rays peaks shown here (labelled a).

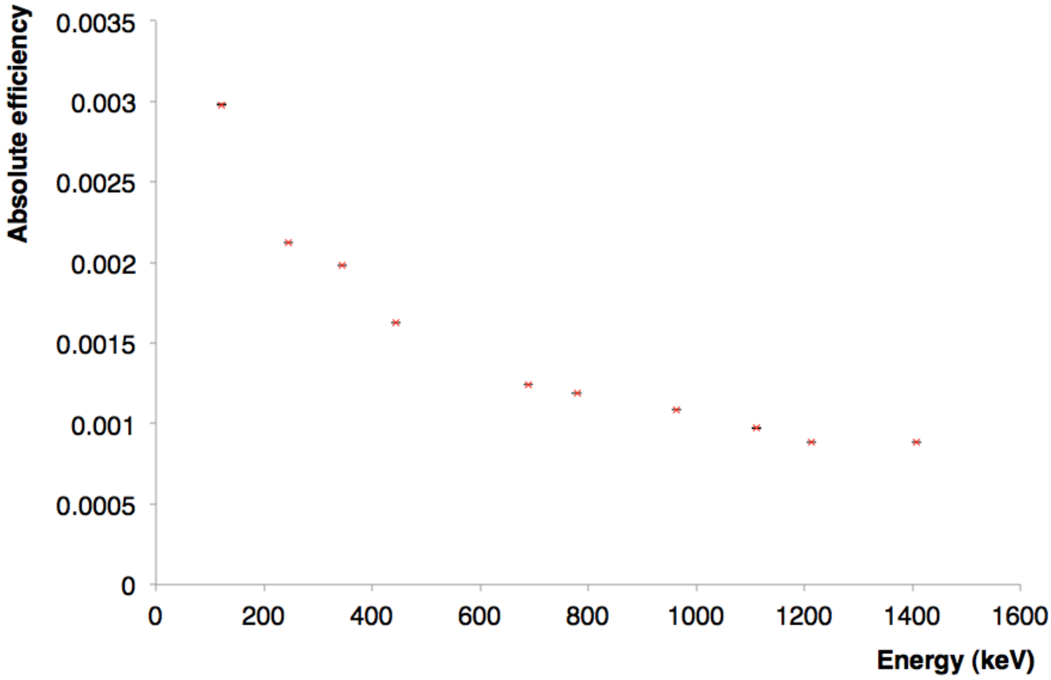

Figure 4.14: The absolute efficiency an asymmetric AGATA detector (C001) using a ^{152}Eu source

threshold could have been lower which may have resulted in a pileup which could have contributed to an additional background.

4.7.1 Efficiency of an AGATA detector

The absolute efficiency of an AGATA detector was determined in a separate experiment using an ^{152}Eu source placed at 25 cm to the front face of detector C001. The efficiency is shown in Figure 4.14. The small error are due to the high counting time for this measurement.

4.8 Compton polarimetry analysis method

In Section 2.4 previous Compton polarimetry work was detailed. It is anticipated that using AGATA as a Compton polarimeter will provide an improvement in the sensitivity that can be achieved. This is due to the granularity of AGATA and the techniques of employing pulse-shape analysis. In Section 2.3.2 the basic design of a Compton polarimeter was outlined and consisted of two detectors; one acting as a scatterer and the second as a absorber. The same principles apply to a AGATA triple cluster with each sector acting as the scatterer and absorber.

4.8.1 Defining an interaction

The pulse-shape analysis algorithm identifies the positions and energies of the interaction points. The algorithm also systematically treats interaction points, within the same sector, which are separated by less than a given distance as one, because they cannot be resolved. This point carries the sum of the individual energies and is situated at the energy-weighted barycentre [Lop04]. In this analysis an interaction is defined as a gamma ray that has interacted once as calculated from the pulse-shape analysis algorithm.

4.8.2 Data sorting and event selection

In the first part of the data analysis it is necessary to utilise the position information outputted from the NARVAL-emulator. This file is created from *WinCtest* and is known as *OftHits*. It contains all interaction positions of the gamma rays in the detector, listed in cartesian format, with their energies and timestamps. A useful event to determine linear polarisation occurs if the incident gamma ray is Compton scattered from the first interaction and then fully absorbed after the second interaction. The sum of the energies deposited in the two interactions gives the energy while the intensity dependence of the azimuthal scattering angle contains the linear polarisation information [Lei97]. Furthermore linear polarisation information could be lost after one or two Compton scatters [Wer95]. For these reasons only two-interaction events were extracted from the *OftHits* file to determine the scattering angles. The number of interactions that occurred was determined and is shown graphically in Figure 4.15. It can be seen that the highest number of interactions were one, that is the gamma

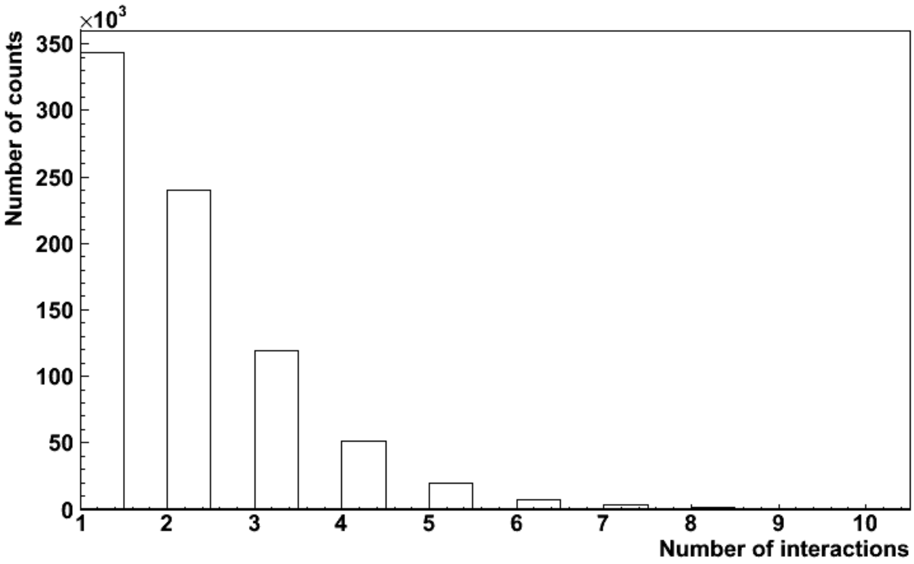

Figure 4.15: Graphical plot of interaction number. This work is concerned with two interaction events and it can be seen that there are approximately 24000 of such.

ray was photoelectric absorbed. Furthermore there are approximately 240000 two-interactions events for use in this work. It could be possible to use the first Compton scatter from a event other than a two-interaction event. However for the purpose of this work two-interaction events were only selected.

4.8.3 Determining the scattering angles

The coordinates need to be converted to spherical polar coordinates in order to determine the change in the azimuthal angle. The relationship between coordinate systems is shown in Figure 4.16. To obtain a set of spherical coordinates for each interaction, the following equations were applied to the cartesian coordinates [Tin00],

$$r = \sqrt{x^2 + y^2 + z^2}, \tag{4.1}$$

$$\theta = cos^{-1}\left(\frac{z}{r}\right), \tag{4.2}$$

$$\phi = tan^{-1}\left(\frac{y}{x}\right). \tag{4.3}$$

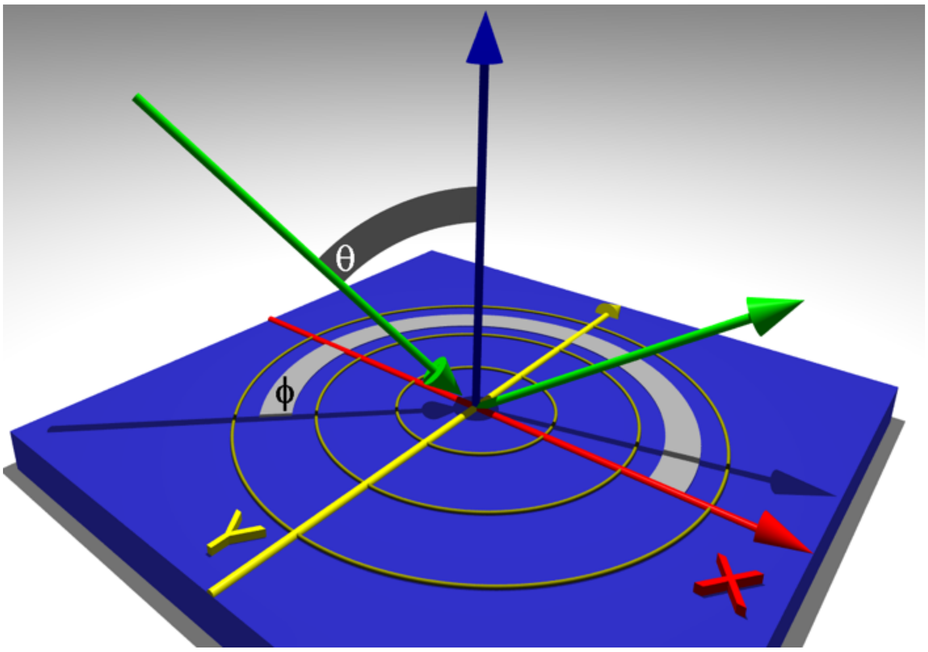

Figure 4.16: A schematic diagram to illustrate the relationship between cartesian and spherical coordinate systems.

Calculating the polar scattering angle (θ)

This is defined as the angle between the incident and scattered gamma ray. The following outlines the steps necessary to determine the polar scattering angle. This calculation assumes the gamma ray was emitted from cartesian coordinate *(0,0,0)*. This is labelled *interaction 0*.

- The coordinate from the two interactions are in the format (x_1, y_1, z_1) (*interaction 1*) and (x_2, y_2, z_2) (*interaction 2*).

- The coordinates of *interaction 2* are transformed in order that it is shifted as from the origin. This is done by subtracting *interaction 1* from *interaction 2*. The new coordinates are labelled *interaction 3*.

- The following equation was used to determine the polar scattering angle.

$$\theta = \cos^{-1} \frac{interaction\,1 \cdot interaction\,3}{||interaction\,1||\;||interaction\,3||}. \tag{4.4}$$

Calculating the azimuthal scattering angle (ϕ)

This is defined as the angle between the electric vector of the incident gamma ray and the plane containing the incident and scattered gamma ray. The following outline how this scattering angle can be determined. Again, the assumption here is that the gamma ray was emitted from cartesian coordinates *(0,0,0)*. This is shown schematically in Figure 4.17.

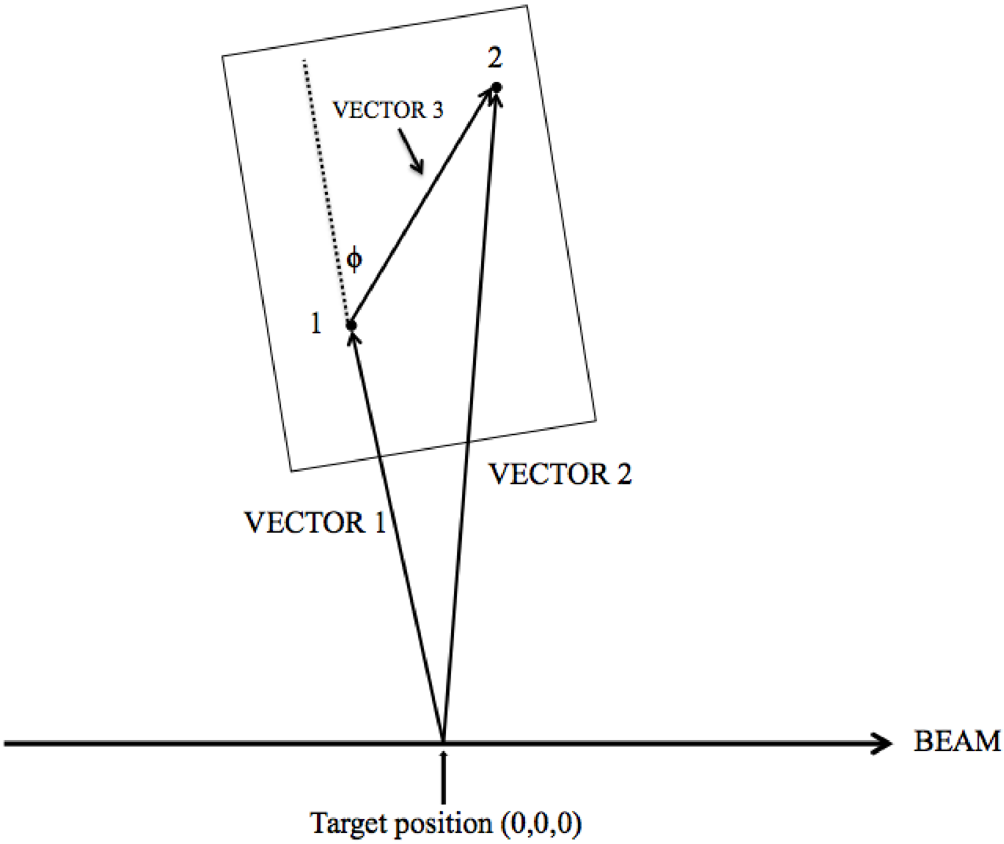

Figure 4.17: A schematic diagrams showing the procedure for calculating the azimuthal scattering angle (ϕ). The azimuthal scattering angle is only dependent on the *(x,y)*.

- Eq. 4.1-4.3 were used to convert (x_1, y_1, z_1) and (x_2, y_2, z_2) to spherical polar coordinates. This formed *vector 1* and *vector 2*, respectively
- *Vector 3* was determined from the vector difference between *vector 2* and *vector*

1.

- The following equation was used to determine the azimuthal scattering angle,

$$\phi = \cos^{-1} \frac{vector\ 1 \cdot vector\ 3}{||vector\ 1||\ ||vector\ 3||}. \tag{4.5}$$

Defining the scattering angle

By analysing the kinematics of each event, the path that a gamma ray took within the detector can be determined. For an incident gamma ray the Compton scattering differential cross-section is given the the Klein-Nishina formula (see Section 2.3 and Eq. 2.8). The angle θ is the polar scattering angle measured from the direction of the incident gamma ray and ϕ is the azimuthal scattering angle measured from the plane containing the electric field vector of the incident gamma ray (see Section 2.3.2 and Figure 2.4). This is polarised Compton scattering. Using Eq. 2.9 and by fixing the value of θ the scattering cross-section for polarised gamma rays is maximum at ϕ=90° and minimum at ϕ=0°, leading to an asymmetry in the number that will scatter parallel and perpendicular to the incident electric field vector. In other words gamma rays tend to scatter at 90° to the incident electric field vector [Sch97]. The asymmetry is defined as follows,

$$A(\theta) = \frac{N(\theta, \phi = 90) - N(\theta, \phi = 0)}{N(\theta, \phi = 90) + N(\theta, \phi = 0)}. \tag{4.6}$$

where N is the number counts in each direction. The relationship between Eq. 4.8 and the linear polarisation, $P(\theta)$, of gamma rays given by,

$$A(\theta) = Q(E_\gamma)P(\theta), \tag{4.7}$$

where $Q(E\gamma)$ is the polarisation sensitivity of the detector and

$$P(\theta) = \frac{W(\theta, \xi = 0^\circ) - W(\theta, \xi = 90^\circ)}{W(\theta, \xi = 0^\circ) + W(\theta, \xi = 90^\circ)}. \tag{4.8}$$

In Eq. 4.8, W is the linear polarisation of gamma rays in terms of an angular distribution function when their electric vector (ξ) is in the reaction place, $W(\theta, \xi = 0^\circ)$, and when perpendicular to the reaction plane, $W(\theta, \xi = 90^\circ)$ [Lee01] [Mil08].

4.8.4 Polarisation sensitivity of the AGATA triple cluster

The polarisation sensitivity (Q) is a Compton polarimeter characterisation method. It depends on the azimuthal scattering angle as as well as the incident and scattered energies. It can be determined from

$$Q(\phi) = \frac{\sin^2 \phi}{\frac{k_1}{k_0} + \frac{k_0}{k_1} - \sin^2 \phi}. \tag{4.9}$$

In Eq. 4.9 k_1 is the wave number of the scattered gamma-ray, k_0 is the wave number of the incident gamma ray and ϕ is the azimuthal scattering angle. The wave number is defined as in Eq. 2.10 In order to measure a polarisation sensitivity value for a photopeak energy is was necessary to obtained an azimuthal scattering angle in addition to an incident and a scattered energy. Using the position information each photopeak energy was gated on and the azimuthal scattering angles was calculated as outlined in Section 4.8.3. This produced an angular distribution of scattering angles. An example of this distribution is shown in Figure E3 (Appendix E). The extraction of an azimuthal scattering angle was achieved by a ROOT [Roo95] implementation of MINUIT with χ^2 minimisation. This angle was chosen as the scattering angle for photopeak. The incident energy was extracted from a Gaussian fit of the photopeak using, again, ROOT [Roo95] MINUIT χ^2-fitting programme. The scattered energy was taken as the average scattered energy for that photopeak.

4.8.5 Asymmetry of a AGATA triple cluster

The following outline the terminology that will be used in the method description for measuring the asymmetry of an AGATA triple cluster.

- *Y-perpendicular* - this defines the perpendicular scatter direction with the beam direction.
- *X-perpendicular* - this defines the parallel scatter direction with the beam direction.

- *beam-perpendicular* - the number of gamma rays that scatter perpendicular with the reaction plane.
- *beam-parallel* - the number of gamma rays that scatter parallel with the reaction plane.
- *energy-scatter* - for a given photopeak energy the number of gamma rays that scatter perpendicular and parallel with the reaction place (E_γ,$N_\perp$,$N_\parallel$).

Assigning ***Y-perpendicular*** and ***X-perpendicular***

The AGATA triple cluster was positioned at 80° to the beam direction. It was assumed that *interaction 1* was approximately 90° to the beam direction and the gamma ray will scatter perpendicular or parallel after *interaction 1.* The directions of scatter *Y-perpendicular* and *X-perpendicular* were assigned, representing a y-axis and x-axis to the beam direction, respectively. This is shown schematically in Figure 4.18. A vector for *Y-perpendicular* was determined from the cross product of *vector 1* (*interaction 1*) and the beam direction. A vector for *X-perpendicular* was determined from the cross product of the *vector 1* and *Y-perpendicular.*

Calculating a scattering vector

A vector was determined which contained the scattering information. This was done by determining the vector difference of the coordinates of *vector 1* and *vector 2.* This produced a new vector *vector 3.* This is shown schematically in Figure 4.19.

Determining ***beam-perpendicular*** and ***beam-parallel***

To determine the scatter direction of *vector 3* it was necessary to project *vector 3* in both the *X-perpendicular* and *Y-perpendicular* directions. The perpendicular projection was determined from the dot product of *vector 3* and *Y-perpendicular.* The parallel projection was determined from the dot product of *vector 3* and *X-perpendicular.* From this *beam-perpendicular* and *beam-parallel* was constructed.

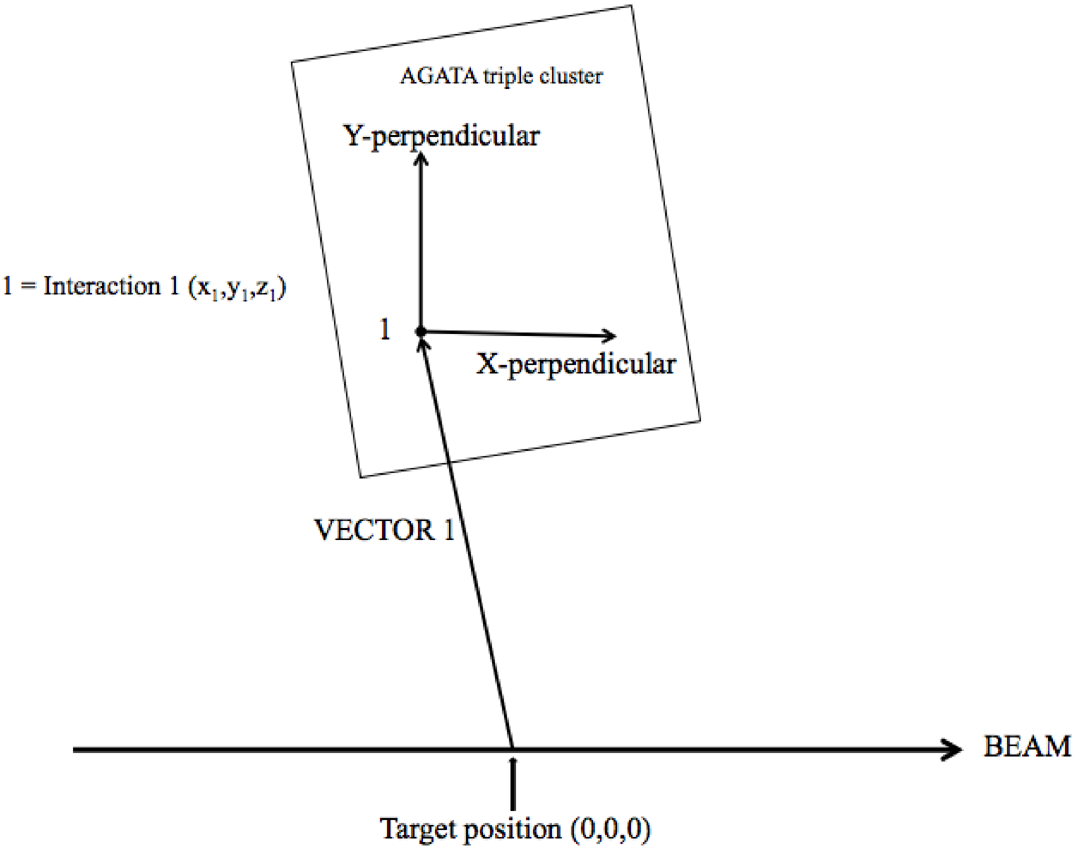

Figure 4.18: A schematic diagram showing the direction of *Y-perpendicular* and *X-perpendicular* with the beam direction.

Background subtraction and peak area selection

In order to obtain a net number of counts in a *perpendicular* and *parallel* direction with the reaction plane, it was necessary to fit and subtract a background to the tracked spectrum shown in Figure 4.9. A background was fitted using the ROOT [Roo95] MINUIT with χ^2-minimisation fitting programme. The background fit is shown in Figure E.1 (Appendix E). It was then necessary to determine what peak area for each photopeak energy would be used in the Compton polarimetry analysis. This was done by implementing a Gaussian fit, again, using the ROOT [Roo95] MINUIT with χ^2-minimisation fitting programme. An example of this is shown in Figure E.2 (Appendix E) for the 346.9 keV photopeak. From this fit a range of energies was

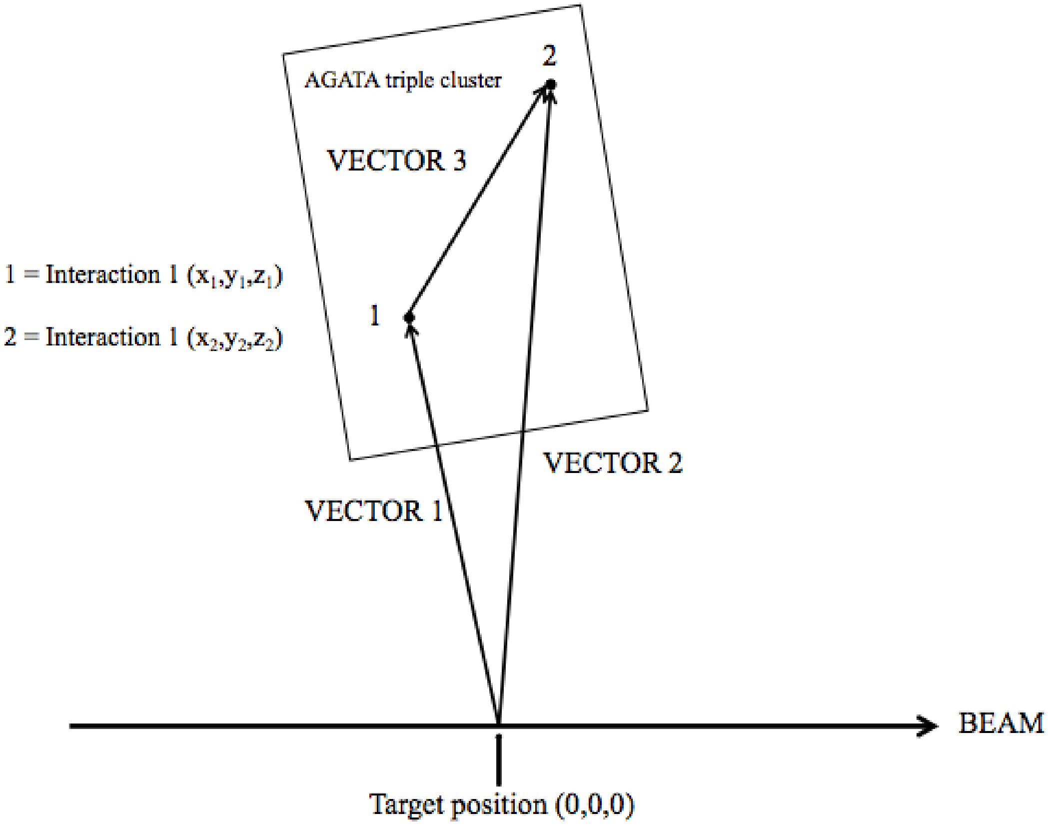

Figure 4.19: A schematic diagram representing the relationship between *vector 1* and *vector 2* with the scattering *vector 3*.

determined for each photopeak and used in methods outlined in this chapter.

Constructing energy-scatter

For each gamma-ray energy of ^{138}Sm an *energy-scatter* was constructed. By applying Eq. 2.15 differing polarisations will appear as positive or negative. As the angular momentum vector of an electric transition is polarised perpendicular to the beam direction and a magnetic transition is polarised parallel, a positive value of asymmetry (A), will show the transition to be predominantly electric in character.

4.8.6 Normalisation constant (a)

In a practical context the asymmetry needs to be normalised to take into account internal asymmetries and the detection efficiency of the absorber. The normalisation constant is the calculated from the ratio of the number of counts perpendicular to the number of counts parallel to the beam direction for an unpolarised gamma-ray source by,

$$a(E_\gamma) = \frac{N_{unpolarised}(\theta, \phi = 90)}{N_{unpolarised}(\theta, \phi = 0)}, \tag{4.10}$$

where N is the number of events that scatter in each direction [Lee02] [Hut02]. Introducing this factor leads to a new asymmetry relationship given by,

$$A = \frac{aN_\perp - N_\parallel}{aN_\perp + N_\parallel}. \tag{4.11}$$

4.8.7 Linear polarisation

The measured asymmetry is proportional to the degree of linear polarisation and is dependent on the gamma-ray energy as,

$$P = \frac{A}{Q}. \tag{4.12}$$

In Eq. 4.12 Q is the polarisation sensitivity and the sign of asymmetry directly gives the sign of the degree of linear polarisation. The degree of linear polarisation was determined for the gamma-ray energies of ^{138}Sm by substituting the previous values for Q and A associated with the gamma-ray energy.

4.8.8 The efficiency of a AGATA triple cluster measuring coincidences between the scatterer and absorber sectors

The coincidence efficiency of an AGATA triple cluster was investigated using the gamma-ray energies of ^{138}Sm. The coincidence efficiency adopted in this work was the previous used expression for segmented detectors by *Hutter et al.* [Hut02]

$$\epsilon = \frac{N_\perp + N_\parallel}{N_{total}}, \tag{4.13}$$

where $N_\perp$ and $N_\parallel$ are the number of scattered events perpendicular and parallel to the reaction plane, respectively, for a given energy. N_{total} is the number of counts without the coincidence requirement. This efficiency produces the amount of coincidence events ($N_\perp$ and $N_\parallel$) compared to the rate of totally detected photopeak events.

4.8.9 Figure of merit (F)

Figure of merit is another method for comparing polarimeters as outlined in section 2.3.5. It is approximately inversely proportional to the time needed for an asymmetry measurement [Mil08]. It depends on the coincidence efficiency and the polarisation sensitivity and is given as,

$$F = \epsilon Q^2. \tag{4.14}$$

Chapter 5

Compton polarimetry results and discussion

5.1 Compton scattering

Compton-scattering events are defined in this work as when a gamma ray has interacted twice as calculated from the pulse-shape analysis algorithm. At each calculated interaction position an amount of energy is deposited. In Figure 5.1, a scattering plot of energy deposited in first interaction versus the energy deposited in the second interaction is shown. The broad diagonal lines in Figure 5.1 are where the sums of energies are constant. From the position information it is possible to calculate the Compton scattering angles for all the interactions as outlined in Section 4.8.3. This is shown in Figure 5.2. The straight vertical lines represent scattering angles of equal energy. A horizontal line at approximately 90° can be seen, the intensity of which decreases with increasing energy. This could reflect the preference for gamma rays to be scattered at Compton scattering angles perpendicular to the polarisation plane of the incident gamma ray. The magnitude of the linear polarisation is extracted in the azimuthal scattering angle calculated using the method outlined in Section 4.8.3. The plot of azimuthal scattering angles is shown in Figure 5.3. It can seen from this plot that the probability of a gamma ray to Compton scatter decreases with increas-

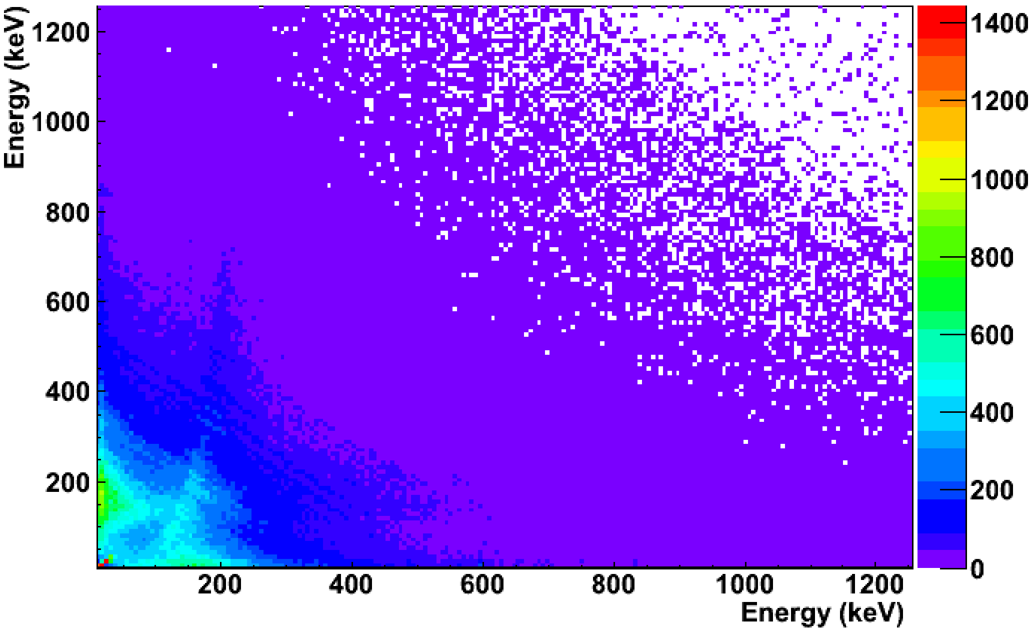

Figure 5.1: A Compton scattering plot. The energy deposited at the first interaction versus the energy deposited at the second interaction for gamma rays emitted from ^{138}Sm. The gamma-ray energies of ^{138}Sm are given in Appendix A.

ing energy. The relationship between both scattering angles in shown in Figure 5.4. The broad line corresponding to 90° polar scattering angle can still be seen with the proposed reason as previously outlined.

5.2 Energy selection for Compton polarimetry measurements

Compton polarimetry measurements were carried out using gamma rays of known multipolarity using the method outlined in Section 4.8. These had previously been assigned by *Paul et al.* [Pau94]. A detailed list of gamma-ray energies and multipolarity are given in Appendix A. A level scheme is given in Appendix B. There were three gamma-ray energies that measurements were not performed on; 686.2, 754.7

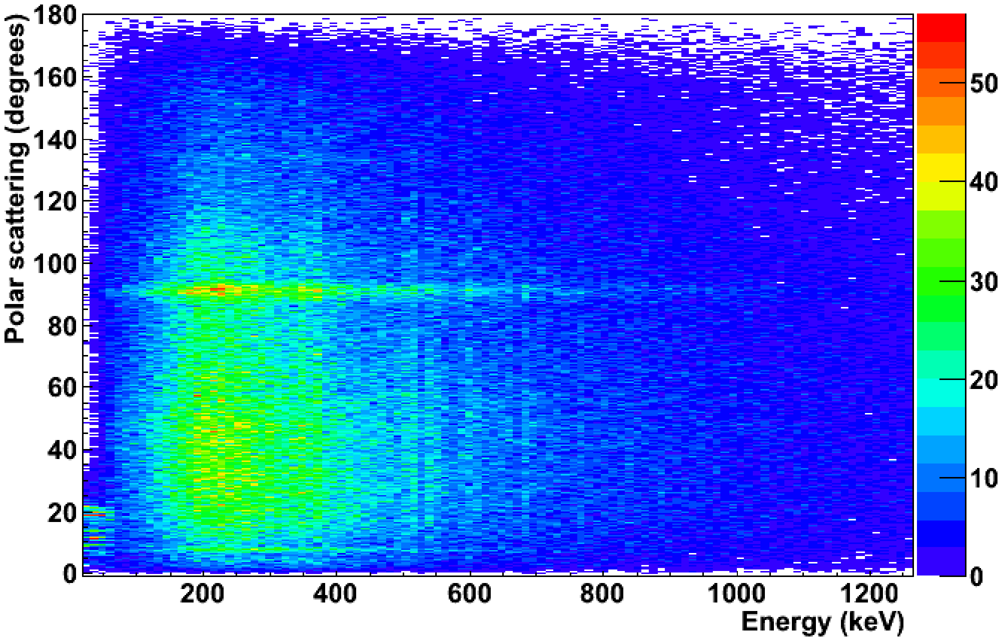

Figure 5.2: Polar scattering angle versus incident gamma-ray energy. Vertical lines show equal energies. The board horizontal line represents a region where the Compton angle is approximately 90°.

and 954.0 keV. The gamma-ray energies were not able to be resolved from 685.9, 754.0 and 953.6 keV, respectively due to a FWMH value of 2 keV.

5.2.1 The normalisation constant (a)

The intrinsic asymmetry an AGATA triple cluster was examined from the scattering of unpolarised gamma rays of ^{133}Ba, for energies 81.0 160.6, 223.3, 302.4, 356.0 and 383.9 keV. A quantitative ratio (normalisation constant) of scatterings perpendicular and parallel to the reaction plane was determined from Eq. 4.10. This ratio accounted and corrected for the different relative efficiencies and solid angles of the absorbing sectors [Wer95]. In addition this normalisation constant accounted for any effects from the tapered angle of each triple cluster. The results are shown in Figure 5.5. The average value is given as 1.10±0.01. The normalisation constant for an ideal

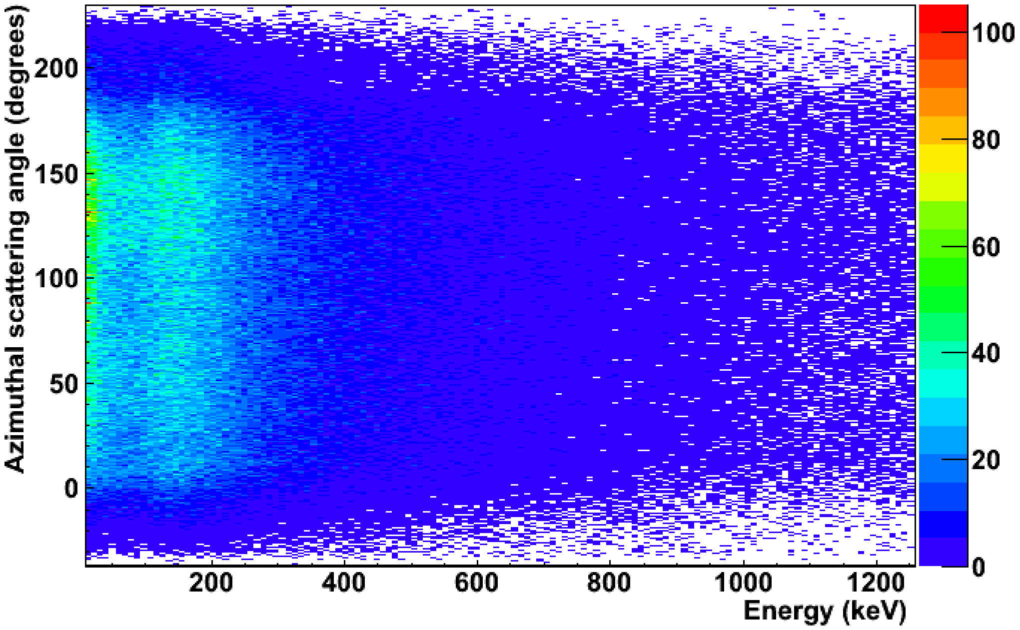

Figure 5.3: Azimuthal scattering angle versus incident gamma-ray energy.

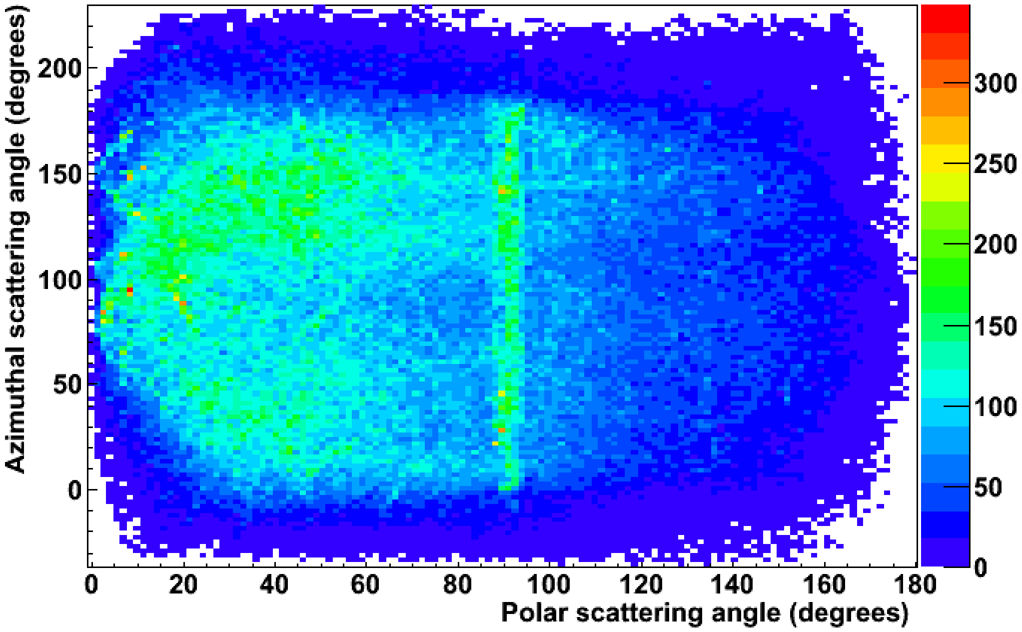

Figure 5.4: Azimuthal scattering angle versus polar scattering angle. The plot retains the key features from Figure 5.2 and 5.3.

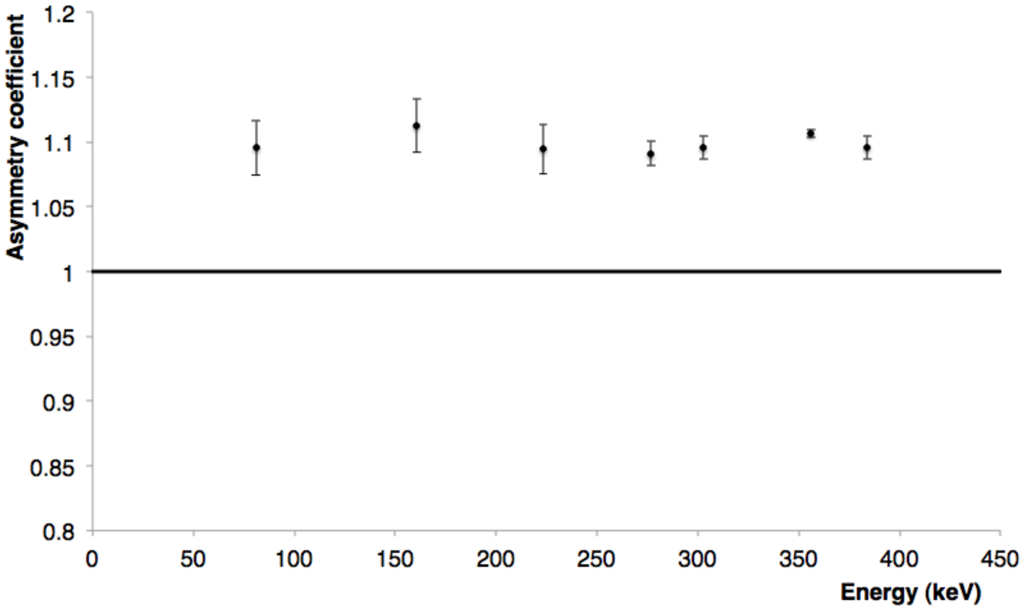

Figure 5.5: The normalisation constant (a) as a function of gamma-ray energy for unpolarised ^{133}Ba. It is a method to quantify the effect of internal geometry on the asymmetry of an AGATA triple cluster. The average value for the normalisation constant was measured as 1.10±0.01.

Compton polarimeter should be one (the line on Figure 5.5 shows the ideal distribution). It can seen that the measured normalisation constant is of the correct order. A good internal geometry of a Compton polarimeter is prerequisite for the analysis of small asymmetries [Hut02]. As stated ^{133}Ba was used to determine a normalisation constant. Due to the maximum gamma-ray energy available of 383.9 keV, the normalisation constant might not reflect the geometry at higher gamma-ray energies. This could have implications on the measured asymmetry of an AGATA triple cluster at higher energies.

5.2.2 Experimental asymmetry measurements

The asymmetry is proportional to the degree of linear polarisation and is dependent on the gamma-ray energy. The number of gamma rays that scattered perpendicular and parallel to the reaction plane were determined using the method outlined in Section 4.8.5. By applying Eq. 4.11 to the measured net number of counts an asymmetry value for each photopeak energy was determined. It has already been stated that an electric character would result in a positive asymmetry. Measurements were first made on E1 transitions and the results are shown in Figure 5.6. It can been seen from Figure 5.6 that the measured asymmetries for E1 transitions were positive. Further asymmetries measurements were made on E2 transitions, results are shown in Figure 5.7. It can be seen that the measured asymmetries are partially consistent with expectation. Table 5.1 summarises the measured asymmetries that were partially consistent with expectation. However the measured asymmetries were consistent, within errors, with expectation. The exception to this was gamma-ray energy 953.6 keV, the measured asymmetry here was -0.18±0.15. Finally asymmetry measurements were also carried out on M1/E2 transitions and the results are shown in Figure 5.8. Again here the measured asymmetries for M1/E2 transitions were partially consistent with expectation, that is the asymmetry should be negative. Table

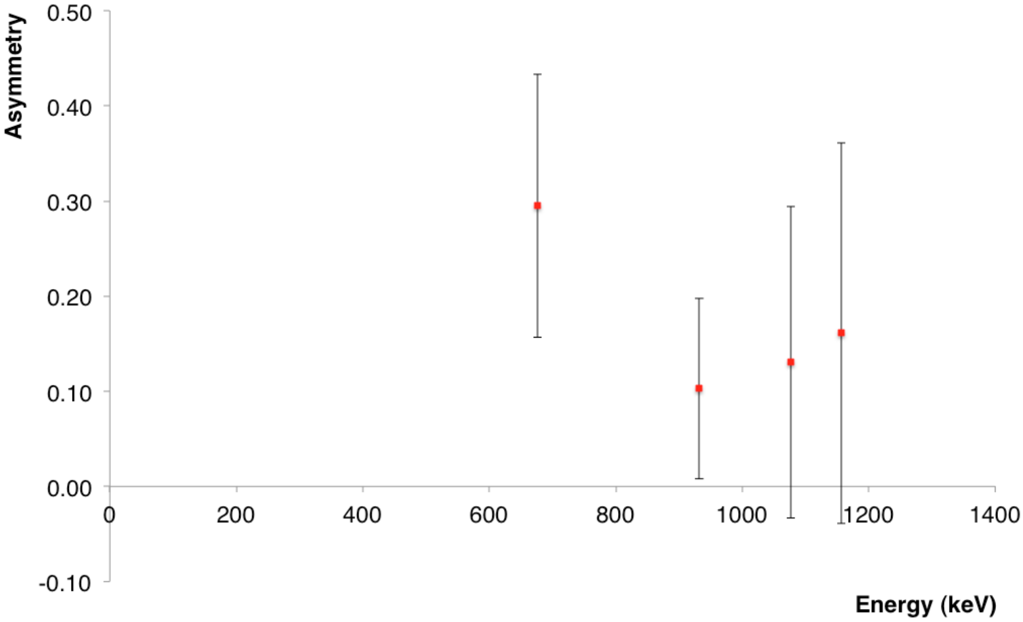

Figure 5.6: The measured asymmetries for E1 transitions of ^{138}Sm.

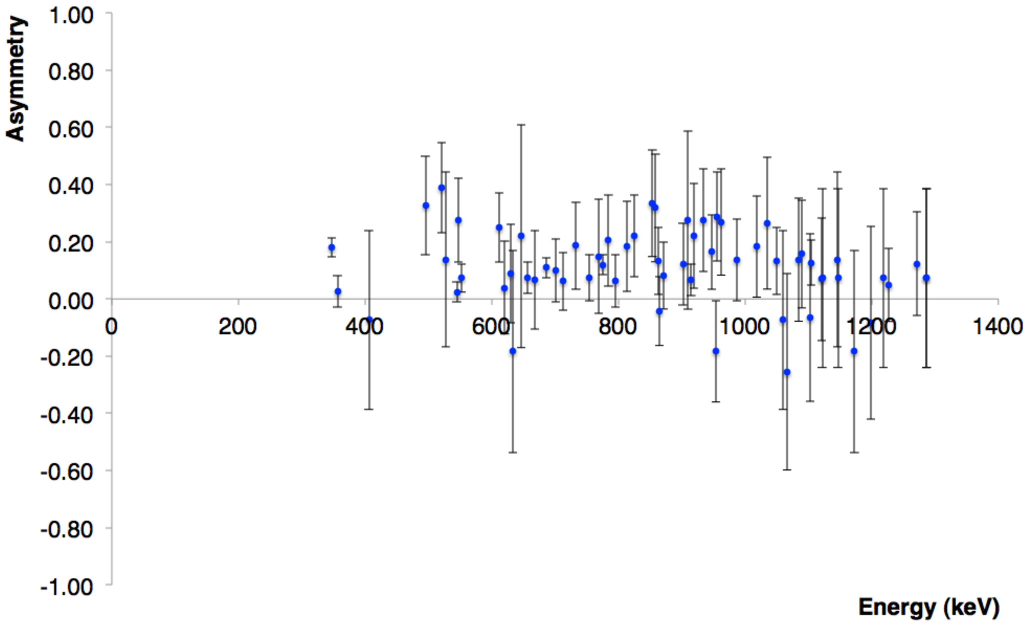

Figure 5.7: The measured asymmetries for E2 transitions of ^{138}Sm.

Energy (keV)	Multipolarity	Iγ%	Measured asymmetry
406.0	(E2)	< 1	-0.07±0.31
633.0	(E2)	< 1	-0.18±0.35
865.0	(E2)	< 1	-0.04±0.12
1059.9	(E2)	1	-0.07±0.31
1066.0	(E2)	< 1	-0.25±0.34
1103.0	(E2)	< 1	-0.06±0.29
1173.0	(E2)	< 1	-0.18±0.35
1199.0	(E2)	< 1	-0.08±0.34

Table 5.1: Summary of measured asymmetries that were consistent, within errors, with expectation for E2 transitions.

5.2 summarises the gamma-ray energies that were measured to be positive. However, the measured asymmetries here were consistent, within errors, with expectation. As there is a competition between photoelectric absorption and Compton scattering be-

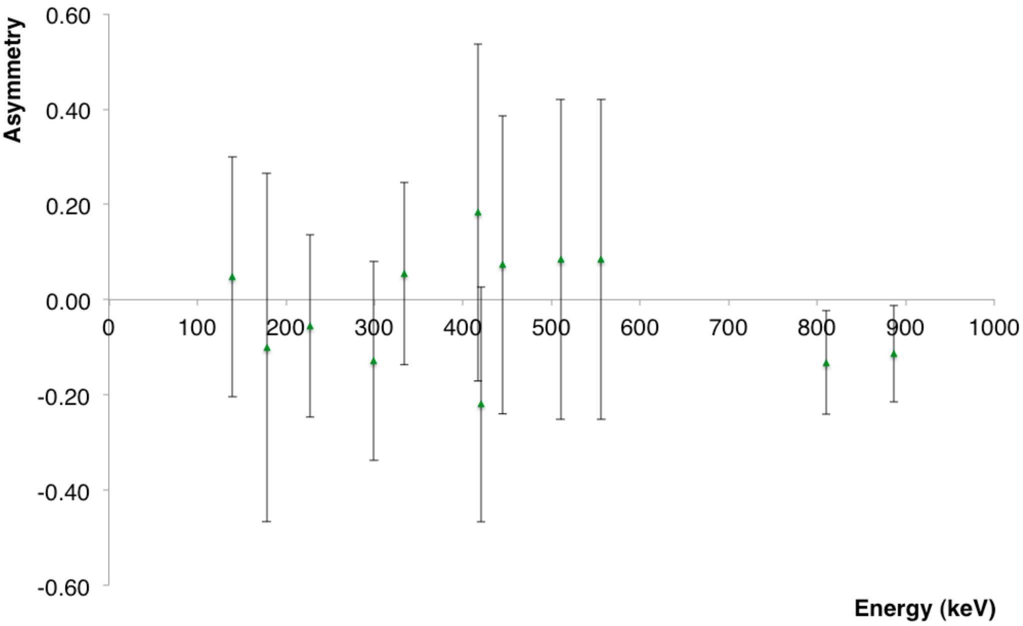

Figure 5.8: The measured asymmetries for M1/E2 transitions of ^{138}Sm.

low ∼200 keV this could have reduced the number of perpendicular and parallel counts which could have resulted in a positive measurement. Other proposed reasons for the all asymmetry measurements which were inconsistent with expectation are given in Section 5.6. Detailed results are given in Appendix D1 and a worked example is given in Appendix E for gamma-ray energy 346.9 keV.

Energy (keV)	Multipolarity	Iγ%	Measured asymmetry
139.7	(M1/E2)	< 1	0.05±0.25
333.6	M1/E2	3	0.06±0.19
417.0	M1/E2	< 1	0.18±0.35
444.4	(M1/E2)	1	0.07±0.31
509.9	(M1/E2)	< 1	0.08±0.34
556.0	(M1/E2)	< 1	0.08±0.34

Table 5.2: Summary of the measured asymmetries that were inconsistent with expectation for M1/E2 transitions.

5.3 Experimental polarisation sensitivity of an AGATA triple cluster

The polarisation sensitivity is a measure of the detector's ability to measure linear polarisation. The polarisation sensitivity was determined in the gamma-ray energy range 139.9-1287 keV using gamma rays of known multipolarity. It has already been stated that AGATA employs a technique of pulse-shape analysis. It is this detailed position information that was used to determine the azimuthal scattering angle and as a result the polarisation sensitivity using the method outlined in Section 4.8.4. Values for Q at a given gamma-ray energy should be in the range $0 \leq Q \leq 1$ ($0 \leq Q \leq 100\%$), [Jon02] to be consistent with previous measurements with other Compton polarimeters and theoretical predictions. The polarisation sensitivity as function of energy results are shown in Figure 5.9, with detailed results given in Appendix D2. The measured polarisation sensitivities are in the previously stated range. The polarisa-

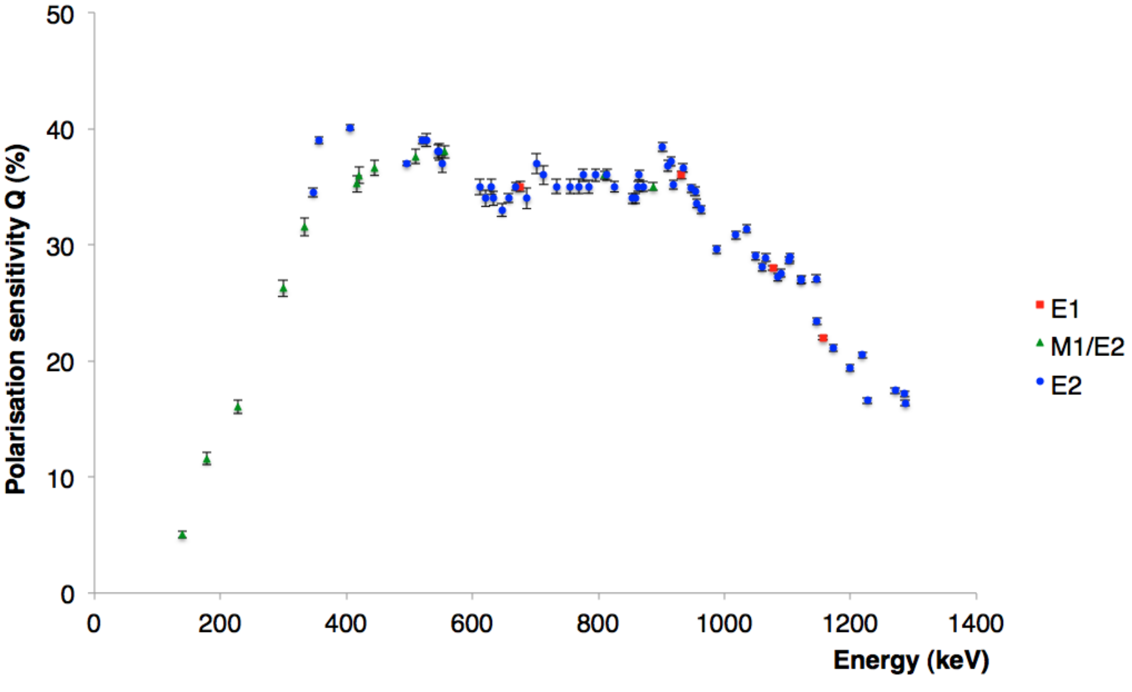

Figure 5.9: Polarisation sensitivity as a function of gamma-ray energy for an AGATA triple cluster for all the transitions of ^{138}Sm.

tion sensitivity was measured to be 5.0±0.3% at 139.7 keV and increases to 40.1±0.8% at 406.0 keV. After this gamma-ray energy there appears to be three dips in sensitivity. Firstly from from 406.0 to 520.5 keV. The second dip is from 520.5 to 701.2 keV and the final dip is from 701.2 to 902.0 keV. After this point the polarisation sensitivity decreases. The polarisation sensitivity at 1287.0 keV was measured to be 16.4±0.1%. The reduced probability of Compton scattering below ~200 keV could result in a decreased polarisation sensitivity because photoelectric absorption carries no polarisation information. For increasing gamma-ray energy the scattering angle is shifted to the forward direction which reduces the polarisation sensitivity [Sch94]. It must be considered that the normalisation constant was only calculated from ^{133}Ba with an energy range of 78-383 keV. The implication here is that the normalisation constant does not reflect the intrinsic geometry of an AGATA triple cluster at gamma-ray energies higher than ~350 keV.

5.4 Experimental linear polarisation

Linear polarisation is the normalised difference in the number of photons occupying two polarisation states [Lei97]. As has already been stated and discussed in this work to determine the linear polarisation of gamma rays, using a Compton polarimeter there has to be a sensitivity of the Compton scattering process to the polarisation of the gamma rays. That is the scattering cross-section is larger in the direction perpendicular to the electric field vector than in the direction parallel to from the Klein-Nishina formula. Precise measurements are important because it prevents wrong multipolarity assignment [Lee01]. The linear polarisation at each gamma-ray energy was determined using the associated polarisation sensitivity and asymmetry measurements applied to Eq. 4.12. The sign of linear polarisation was directly related to the sign of the asymmetry measurement. The results are shown in Figure 5.10. In Section 2.2 it was stated that a linear polarisation measurement should be in the range $-1 \leq P(\theta_\gamma) \leq +1$ [Lei97]. It can be seen that the measured linear polarisations

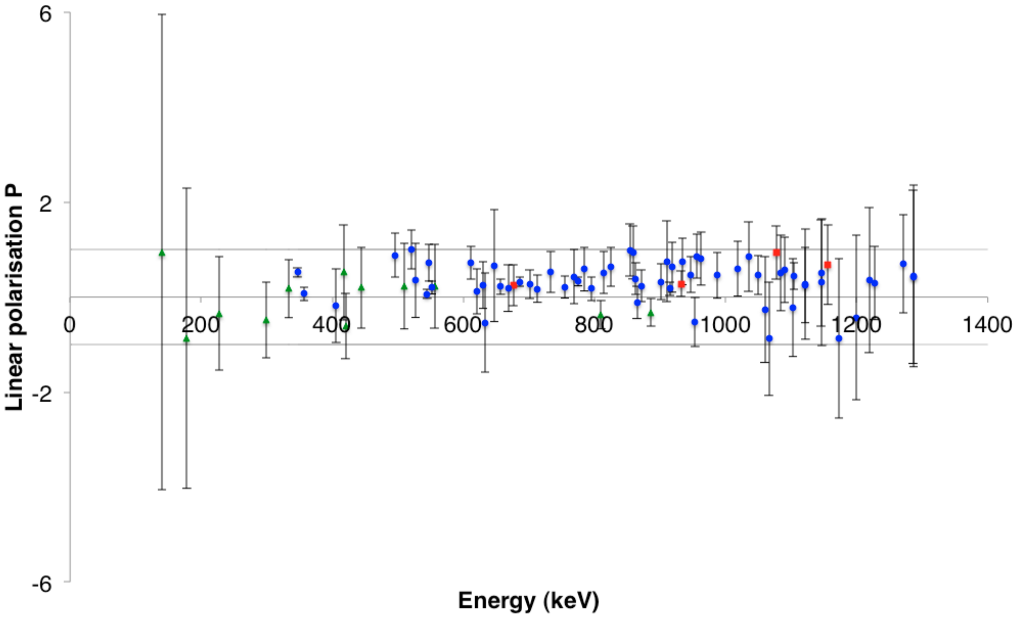

Figure 5.10: Linear polarisation as a function of energy for all transitions of ^{138}Sm.

are within this range. There are a number of measurements with an incorrect sign assigned, these measurements are summerised in Table 5.3. It can clearly be seen that using the method outlined in Section 4.8 the limited capability of an AGATA triple cluster as a Compton polarimeter has been demonstrated. Proposed reasons for this are discussed in Section 5.6.

5.5 Efficiency of an AGATA triple cluster and figure of merit

This is the efficiency of an AGATA triple cluster to measure coincidences between the scatterer and absorber sectors. This was measured from the ratio of the number of gamma rays that scattered perpendicular and parallel to the total number of peak counts without this coincidence requirement using Eq 4.13. The efficiency was measured using the gamma-ray energies of ^{138}Sm. The results are shown in Figure 5.11. It can been seen from Figure 5.11 that the coincidence efficiency increases

Energy (keV)	Multipolarity	Iγ%	Linear polarisation
406.0	(E2)	< 1	-0.18±0.78
633.0	(E2)	< 1	-0.53±1.04
865.0	(E2)	< 1	-0.11±0.33
1059.9	(E2)	1	-0.26±1.12
1066.0	(E2)	< 1	-0.87±1.19
1103.0	(E2)	< 1	-0.23±1.03
1173.0	(E2)	< 1	-0.87±1.68
1199.0	(E2)	< 1	-0.43±1.73
139.7	(M1/E2)	< 1	0.95±5.01
333.6	M1/E2	3	0.17±0.61
417.0	M1/E2	< 1	0.52±1.01
444.4	(M1/E2)	1	0.20±0.85
509.9	(M1/E2)	< 1	0.23±0.90
556.0	(M1/E2)	< 1	0.22±0.89

Table 5.3: Summary of the measured linear polarisations that were consistent, within errors, with expectation for E2 and M1/E2 transitions.

with increasing energy up to ~400 keV. After this energy the AGATA triple exhibits almost uniform efficiency before slightly increasing again at ~1285 keV. The coincidence efficiency at 139.7 keV is 23.0±5.3% and is 40.1±13.7% at 1287 keV. Using the coincidence efficiency method outlined in Section 4.8.4, an AGATA triple cluster exhibits low coincidence efficiency. The coincidence efficiency of segmented detectors was investigated by *Hutter et al.* [Hut02] where a coincidence efficiency at lower energies was measured to be ~20%. An AGATA triple cluster exhibits a much lower coincidence efficiency at lower energies. This could be partly due to the lower perpendicular and parallel counting rates due to the competition of Compton scattering with photoelectric absorption. Previous work by *Hutter et al.* [Hut02] and *Schlitt et al.* [Sch04] found the the coincidence efficiency also increases with increasing energy

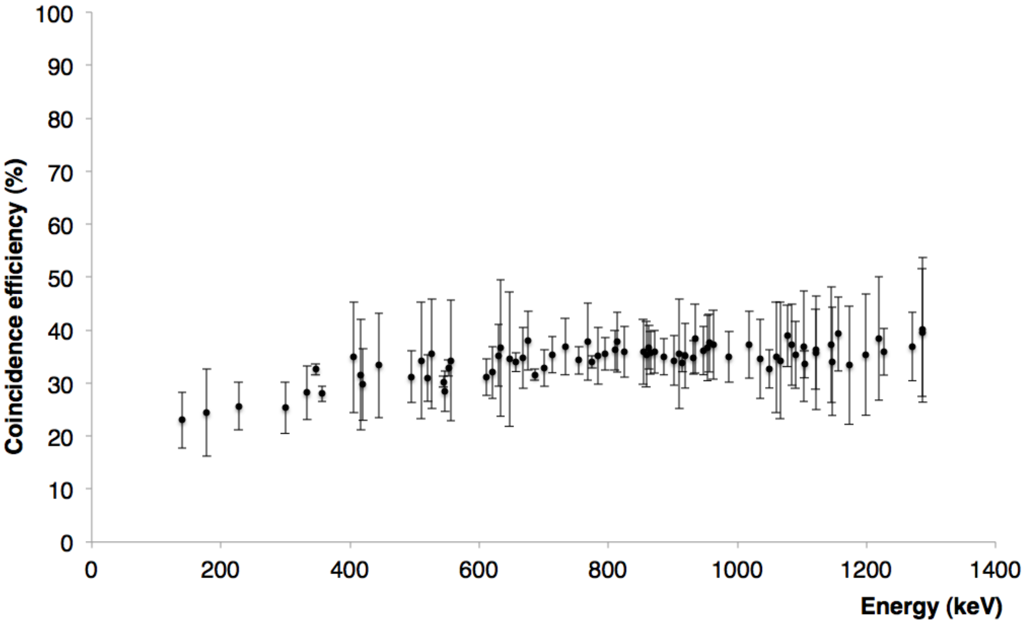

Figure 5.11: Coincidence efficiency as a function of energy for an AGATA triple cluster to measure coincidence between the scatterer and absorber sectors.

up to a saturation point. Even though an increase in coincidence efficiency is observed with an AGATA triple cluster it is unclear if the almost uniform part of the measured efficiency is a saturation point.

5.5.1 Figure of merit

The figure of merit is an important quantity when comparing the performance of different polarimeters. It determines the measuring time necessary to achieve a certain accuracy in measuring an asymmetry [Sch94]. The figure of merit was determined for the gamma-ray energies of ^{138}Sm, detailed results are given in Appendix D2, and shown graphically in Figure 5.12. The figure of merit at 139.7 keV is 0.06±0.02% and it increases with increasing energy to 5.6±1.7% at 406.0 keV. Following this there is almost uniform response to ∼950 keV, expect for a dip around ∼650 keV. After ∼950 keV the figure of merit decreases with increasing energy. The figure of merit at 1287 keV is 1.1±0.4%. Similar features can be seen for polarisation sensitivity measurements (Figure 5.9). This is to be expected because the polarisation sensitivity propagates quadratically into the figure of merit [Sch94].

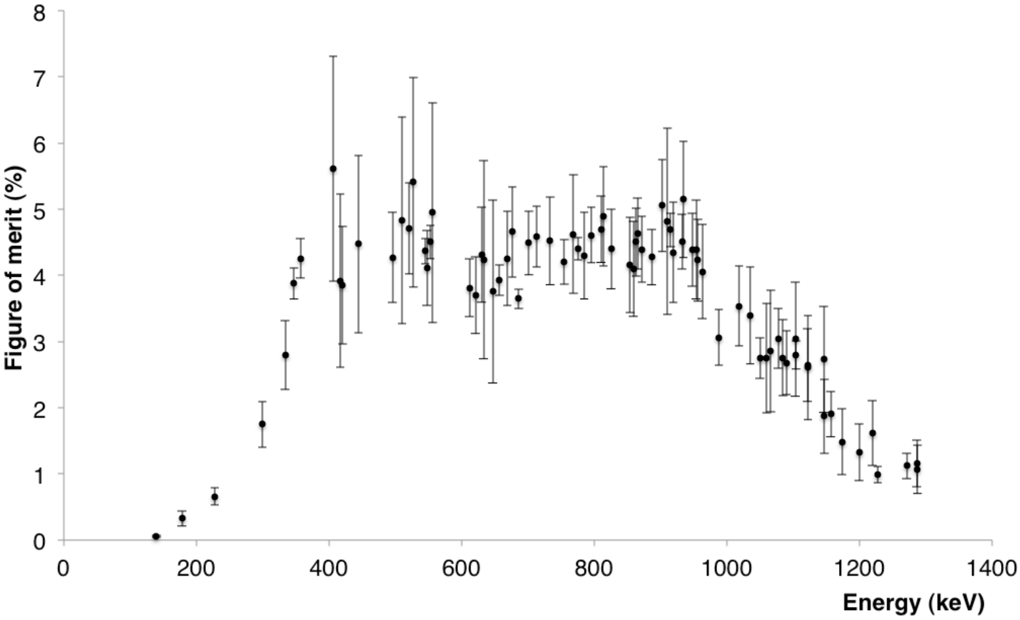

Figure 5.12: Figures of merit for an AGATA triple cluster for the gamma-ray energies of ^{138}Sm.

5.6 Discussion

In this work, using the method outlined in Section 4.8, it has demonstrated the limited capability of an AGATA triple cluster as a Compton polarimeter. The following will discuss proposed reasons for why the capability is limited.

5.6.1 Effectiveness of the tracking algorithm

In Section 3.2.5 the principles of gamma-ray tracking were outlined. The Compton scattering angle can be calculated from using the Compton scattering formula (Eq. 2.7) and from the position information (Eq. 3.8). The smallest difference between each angle corresponds to the correct scattering angle. In this work two-interaction events were used to determine the Compton polarimetry capability. *Hammond et al.* [Ham05] investigated an ambiguity in gamma-ray tracking, of two-interaction events, in the gamma-ray energy range 255-700 keV, because there is the greatest ambiguity in this range. An example in shown in Figure 5.13 for a 600 keV gamma ray. In Figure 5.13a a 600 keV gamma ray is forward scattered at 55°. The energy deposited at the first interaction position is 200 keV and at the final interaction position is 400 keV. The same gamma ray could have deposited 400 keV at the first interaction position, then backscattered at an angle of 135°, and finally deposited 200 keV (Figure 5.12b). In both examples the distance between the target and first interaction is 10 cm and the scattered gamma ray travelled 2.3 cm. According to the Compton scattering formula both sequences are possible leading to an ambiguity. This has an implication for the determination of the emission angle. This is given in this example of ∼10°. Misidentification of the tracks of gamma rays in this energy range, around 90°, is relevant to linear polarisation experiments because asymmetries are largest near 90° [Ham05]. The ambiguity could result in a larger angular distribution of scattering angles which would reduce the polarisation sensitivity.

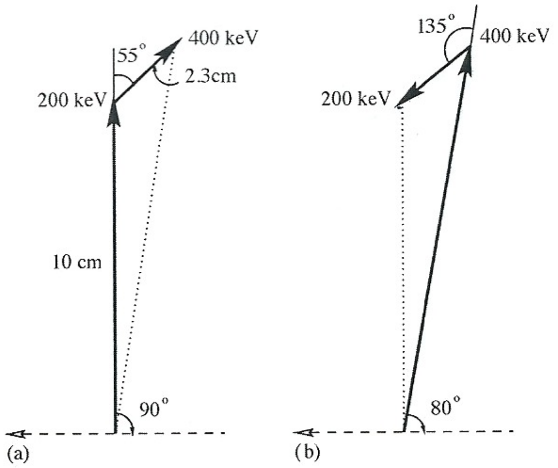

Figure 5.13: An example of an ambiguous scattering sequence for a 600 keV gamma ray [Ham05]

5.6.2 Potential limitations of the pulse shape analysis algorithm

Influence of the barycenter

In this work an interaction was defined by the pulse-shape analysis algorithm and is given at the energy-weighted barycenter [Lop04]. If the second interaction took place within a different sector to the first interaction this would be recorded as two interactions. Problems can arise when the second interaction took place within the same sector as the first interaction. The energy-weighted barycenter method would only record this as one interaction. Polarisation information is generally lost after one or two Compton scatters [Wer95]. The energy-weighted baycenter method could reduce the number of perpendicular and parallel count rates thus resulting in a loss of linear polarisation information. This is proposed as a strong reason for the incorrect assignment of E2 and M1/E2 transitions. Furthermore the loss of counts could result in a loss of efficiency.

Location the interaction position

The pulse-shape analysis algorithm compares the measured pulse shape to a theoretical basis dataset of known interactions and finds the χ^2 to define the interaction position. The accuracy of this is fundamental to provide the tracking algorithms with the correct position information. The basis dataset that was used in this work was JASS. When data are replayed through the NARVAL-emulator proportional cross-talk corrections are applied as outlined in Section 4.4.2. Without these corrections a decreased energy would be recorded because of a net flow of charge from the hit sector to another sector. This could result in a decreased number of counts in a photopeak. However there are two types of cross talk and, the second type, differential is not corrected for in the NARVAL-emulator. This could have an implication for Compton polarimetry measurements. A decreased number of photopeak events could in turn decrease the number of counts perpendicular and parallel to the reaction place. This could lead to an incorrect asymmetry measurement leading to an incorrect electric of magnetic character assignment. The spatial distribution in the x-y plane and x-z plane for the first interaction, calculated by the pulse-shape analysis algorithms, were investigated. Spatial distributions are shown in Figure 5.14 and Figure 5.15 for x-y and x-z, respectively. The front face of the AGATA triple cluster should exhibit a uniform distribution. This is not observed due to clustering of points. The clustering effect observed in Figure 5.14 and 5.15 could be due to the differential cross-talk within the AGATA triple cluster that has not been corrected for in the pulse-shape analysis algorithm.

5.6.3 Limitation of two interaction events

In this work two-interaction events were used to investigate the Compton polarimetry capability of an AGATA triple cluster. Figure 4.15 (Section 4.8.2) shows the number of events that interacted twice. This was given at ~240000. Also shown in Figure 4.15 were the number of events that interacted other than twice. One interaction events cannot be used because photoelectric absorption carries no polarisation information. If the first Compton scatter from any event was used in addition to the two-interaction events this could potentially increase the polarisation sensitivity and improve an asymmetry measurement thus leading to a better estimate of linear polarisation.

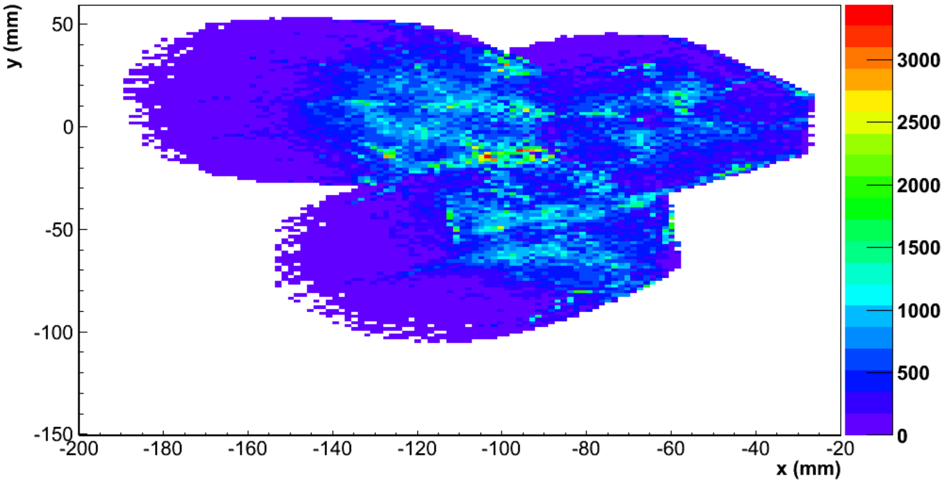

Figure 5.14: The x-y plane distribution for the first interaction point calculated by the pulse shape analysis algorithm. The front face of the AGATA triple cluster should exhibit a uniform distribution. However this is not seen due to clustering of interaction points.

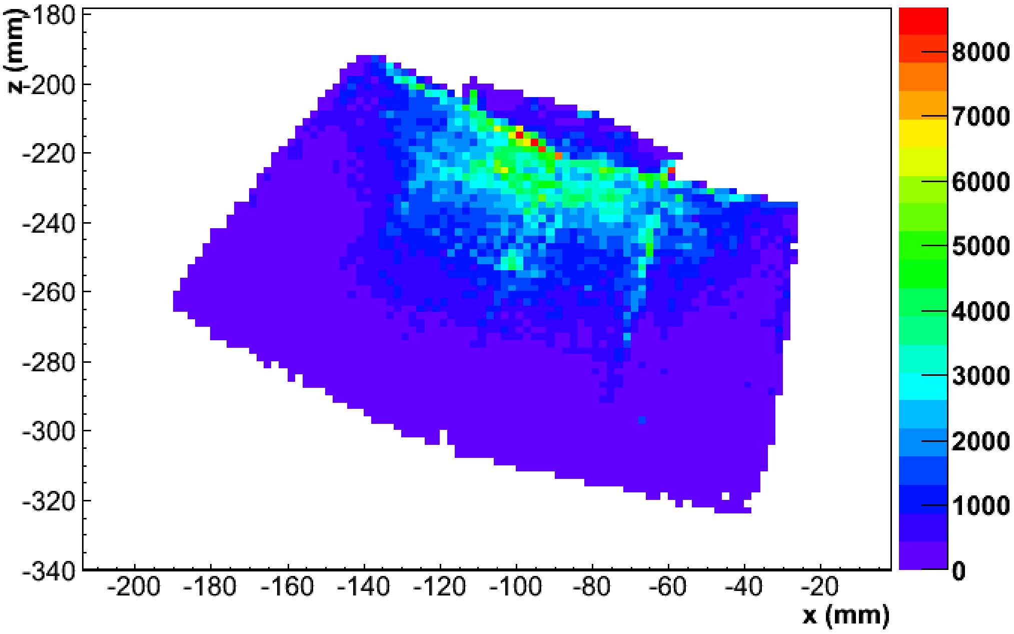

Figure 5.15: The x-z plane distribution for the first interaction point calculated by the pulse shape analysis algorithm.

Chapter 6

Summary and conclusions

A new generation of gamma-ray spectrometers is currently under construction in Europe and the USA; namely AGATA and GRETA, respectively. The performance of these arrays will be based on the techniques of pulse-shape analysis and gamma-ray tracking. The position information of the interacting gamma ray is necessary for the tracking algorithm. This position information is determined from pulse-shape analysis, from the detected pulse shapes on the sector electrodes which are characteristic of the interaction positions. The pulse-shape analysis algorithm compares the measured pulse shapes to a simulated basis dataset of known interaction positions. The minimal χ^2 defines the interaction point. Currently the pulse shape algorithm reconstructs one interaction point per sector. If there are multiple interactions within a sector then the reconstructed interaction position is given as the energy-weighted barycenter. There are two basis datasets implemented; JASS and ADL. Central to the AGATA spectrometer is the data acquisition, NARVAL. It controls the data flow from the crystals and processes the data by utilising implemented actors, each performing a specific action. A key feature of NARVAL is the NARVAL-emulator which can be installed on a computer of the user's choice. It can be used to replay data from a performed experiment. The choice of computer language allows the user to manipulate the implemented actors to produce spectra of a given format. In this work it was demonstrated that by implementing a ROOT output into the *producer*, *preprocessing* and *pulse shape analysis actors* spectra was produced. Data obtained from the heavy-ion fusion-evaporation ^{110}Pd (^{32}S,4n) ^{138}Sm at 135 MeV was replayed through the NARVAL-emulator and position information was extracted to measure the Compton polarimetry capability of an AGATA triple cluster. Two-interaction Compton scattering events, as given by the pulse-shape analysis algorithm, were selected. The Compton polarimetry capability was investigated through measurements of polarisation sensitivity, asymmetries and linear polarisations. The measured polarisation sensitivities ranged from 5.1±0.3% at 139.7 keV to 16.3±0.2% at 1287 keV. Asymmetry measurements were carried out on E1, E2 and M1/E2 transitions and the resulting sign would indicate an electric or magnetic character. It was found that there was only partial consistency with expectation. Using the polarisation sensitivity and the asymmetry measurements, a linear polarisation was determined at each gamma-ray energy, with the sign from the asymmetry measurement propagating through. Finally measurements were made to obtain a coincidence efficiency and a figure of merit. The coincidence efficiency ranged from 23.0±5.3% at 139.7 keV to 40.1±13.7% at 1287 keV. The figure of merit ranged from 0.06±0.02% at 139.7 keV to 1.1±0.4% at 1287 keV. It was found that an AGATA triple cluster exhibited low coincidence efficiency and figure of merit at low energies. It is concluded that, using the method in this work, an AGATA triple cluster has a limited Compton polarimetry capability.

6.1 Future work

It has been proposed that this limited capability could be due to the energy-weighted barycenter method which is utilised by the pulse-shape analysis method and the non-correction of the effect from differential cross-talk. Other proposed reasons included only using two-interaction events and an ambiguity of gamma-ray tracking with two-interaction events. Initially future work could investigate it there is an improvement in polarisation sensitivity and asymmetry measurements from using the first Compton scatter from any event. Finally, improvements in the Compton polarimetry measurements using an AGATA detector is dependent on improvements in the pulse-shape analysis algorithms. The key future work would be improve the basis dataset by correcting for differential cross-talk.

Appendix A

Transitions in ^{138}Sm

Energy(keV)	**Iγ%**	**Multipolarity**	**Assignment**	**Band**
139.7	< 1	(M1/E2)	$(14^- \to 13^-)$	12
178.2	1	(M1/E2)	$(15^- \to 14^-)$	12
227.4	4	M1/E2	$(16^- \to 15^-)$	12
299.4	3	M1/E2	$(17^- \to 16^-)$	12
333.6	3	M1/E2	$(18^- \to 17^-)$	12
346.9	100	E2	$2^+ \to 0^+$	12
356.6	41	E2	$12^+ \to 10^+$	4
406.0	< 1	(E2)	$(16^- \to 14^-)$	12
417.0	< 1	M1/E2	$13^- \to 12^-$	9, 8
420.2	2	(M1/E2)	$(19^- \to 18^-)$	12
444.4	1	(M1/E2)	$(20^- \to 19^-)$	12
495.4	4	E2	$18^+ \to 16^+$	5, 4
509.9	< 1	(M1/E2)	$(21^- \to 20^-)$	12
520.5	5	E2	$(9^- \to 7^-)$	1
527.0	< 1	(E2)	$(17^- \to 15^-)$	12
544.9	98	E2	$4^+ \to 2^+$	6

Table A.1 – Continued

Energy(keV)	**Iγ%**	**Multipolarity**	**Assignment**	**Band**
547.4	6	(E2)	$18^+ \rightarrow 16^+$	5
552.3	43	E2	$10^+ \rightarrow 8^+$	4, 6
556.0	< 1	(M1/E2)	$(22^- \rightarrow 21^-)$	12
611.6	9	E2	$(11^- \rightarrow 9^-)$	1
620.7	5	E2	$(11^- \rightarrow 9^-)$	11
630.1	4	E2	$(17^- \rightarrow 15^-)$	2
633.0	< 1	(E2)	$(18^- \rightarrow 16^-)$	12
646.9	1	E2	$(9^- \rightarrow 7^-)$	11
657.0	39	E2	$14^+ \rightarrow 12^+$	4
668.3	4	E2	$14^+ \rightarrow 12^+$	9,10
676.0	4	(E1)	$14^+ \rightarrow 12^+$	1,6
685.9	95	E2	$6^+ \rightarrow 4^+$	6
686.2	8	E2	$(20^+ \rightarrow 18^+)$	5
701.2	9	E2	$(13^- \rightarrow 11^-)$	1
713.0	12	E2	$12^+ \rightarrow 10^+$	10
733.3	7	E2	$(15^- \rightarrow 13^-)$	2, 1
754.0	< 1	E2	$(19^- \rightarrow 17^-)$	12
754.7	18	E2	$10^+ \rightarrow 8^+$	10, 6
768.5	3	(E2)	$(16^+ \rightarrow 14^+)$	9
775.2	91	E2	$8^+ \rightarrow 6^+$	6
784.4	4	E2	$(19^- \rightarrow 17^-)$	2
795.3	12	E2	$14^+ \rightarrow 12^+$	10
810.1	8	M1/E2	$13^+ \rightarrow 12^+$	8, 4
813.8	4	(E2)	$(13^- \rightarrow 11^-)$	11
825.1	5	E2	$16^+ \rightarrow 14^+$	10
853.9	3	E2	$15^+ \rightarrow 13^+$	8
858.7	3	(E2)	$(15^- \rightarrow 13^-)$	1

Table A.1 – Continued

Energy(keV)	**Iγ%**	**Multipolarity**	**Assignment**	**Band**
863.1	7	E2	$16^{+} \to 14^{+}$	5, 4
865.0	< 1	(E2)	$(20^{-} \to 18^{-})$	12
871.3	7	E2	$22^{+} \to 20^{+}$	5
886.3	10	M1/E2	$15^{+} \to 14^{+}$	7, 4
902.0	5	E2	$18^{+} \to 16^{+}$	10
910.0	< 1	(E2)	$(18^{+} \to 16^{+})$	9
915.0	36	E2	$16^{+} \to 14^{+}$	4
918.8	3	E2	$(22^{+} \to 20^{+})$	3
931.9	11	(E1)	$7^{-} \to 6^{+}$	1, 6
934.2	3	(E2)	$17^{+} \to 15^{+}$	8
947.4	6	E1	$9^{-} \to 8^{+}$	11, 6
953.6	3	(E2)	$(21^{-} \to 19^{-})$	2
954.0	< 1	(E2)	$(21^{-} \to 19^{-})$	12
956.1	4	E2	$(24^{+} \to 22^{+})$	3
962.7	3	(E2)	$(17^{+}) \to 15^{+}$	7
987.3	5	E2	$(15^{-} \to 13^{-})$	12, 11
1018.3	3	(E2)	$(26^{+} \to 24^{+})$	3
1035.0	2	(E2)	$(20^{+}) \to 18^{+}$	10
1049.5	8	(E2)	$(20^{-}) \to 18^{+}$	3, 4
1059.9	1	(E2)	$(17^{-} \to 15^{-})$	1
1066.0	< 1	(E2)	$(22^{-} \to 20^{-})$	12
1077.0	4	(E1)	$(7^{-}) \to 6^{+}$	11, 6
1084.4	2	(E2)	$(28^{+} \to 26^{+})$	3
1089.8	3	(E2)	$(24^{-} \to 22^{+})$	5
1103.0	< 1	(E2)	$(24^{-} \to 22^{-})$	12
1104.0	17	E2	$18^{+} \to 21^{-}$	4
1121.3	2	(E2)	$(23^{-} \to 13^{-})$	2

Table A.1 – Continued

Energy(keV)	**Iγ%**	**Multipolarity**	**Assignment**	**Band**
1122.0	< 1	(E2)	$(23^- \rightarrow 21^-)$	12
1145.6	1	(E2)	$(30^+ \rightarrow 28^+)$	3
1146.8	1	(E2)	$(19^+ \rightarrow 17^+)$	7
1156.3	3	(E1)	$(15^- \rightarrow 13^-)$	2, 4
1173.0	< 1	(E2)	$(14^- \rightarrow 14^-)$	12
1199.0	< 1	(E2)	$(32^+ \rightarrow 30^+)$	3
1219.0	< 1	(E2)	$(27^- \rightarrow 25^-)$	12
1227.0	6	E2	$14^+ \rightarrow 12^+$	9, 4
1271.1	3	(E2)	$(20^+ \rightarrow 18^+)$	4
1286.0	< 1	(E2)	$(26^+ \rightarrow 24^+)$	5
1287.0	< 1	(E2)	$(25^- \rightarrow 23^-)$	2

Appendix B

Level scheme for ^{138}Sm

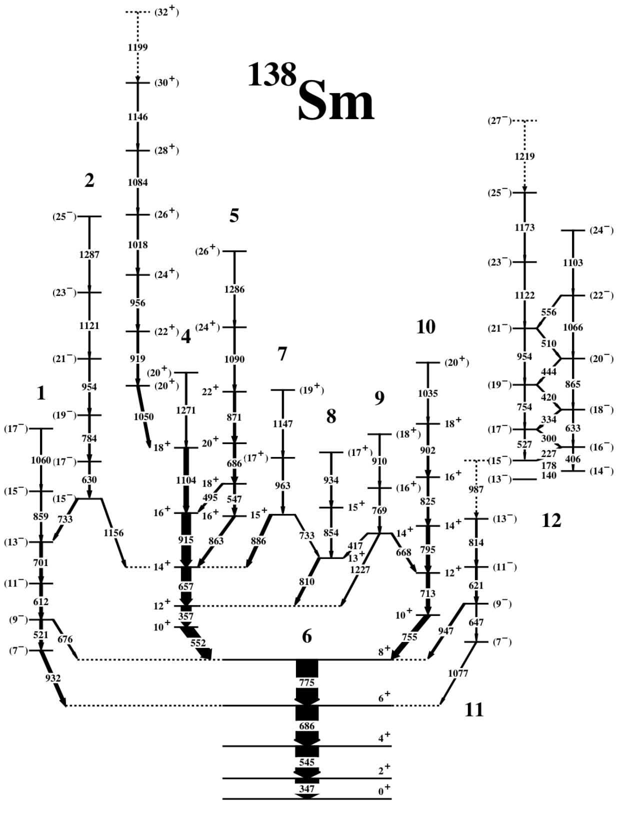

Figure B.1: Level scheme for ^{138}Sm *Paul et al.* [Pau94]

Appendix C

NARVAL-emulator

C.1 The NARVAL-emulator installation guide

You need to have svn and boost and installed.

You also need libboost-thread-dev (multi threading libboost) installed.

Create narval_emu directory and change the directory to narval_emu.

Run svn co svn://gamma01.lnl.infn.it/agata/trunk/narval_emulator.

Change directory to myADF0.2.

Type chmod +x configure.

Run ./configure ithout-narval.

Change directory to WinCtest.

Run cmake -i, it will ask you to set the names of variables:

Set CMAKE_BUILD_TYPE to Release.

Set CMAKE_INSTALL_PREFIX to /usr/local.

Set ROOT_CINT_EXECUTABLE to your root1 directory .../root/bin/rootcint.

Set ROOT_CONFIG_EXECUTABLE to your root directory .../root/bin/root-config.

C.2 CrystalProducer.conf

```
ActualClass       CrystalProducerATCA
```

```
CrystalID         10
TimeStep         10
TstampCorrection  0
ReadDataPrefix /Data/AGATA/
WriteDataPrefix /Data/AGATA/Output/1G/
```

C.3 CrystalProducerATCA.conf

```
# analysis setup for SortATCA and for ProducerDiskMezzanine
#
# defined keywords and expected input fields are
#
# file --> file# #mezz datafile
# mezz --> #mezz file# slot# #chan
# core --> #seg  mezz# chan#  calE thresh tau [tau2 tau20 [tau3 tau30] ]
# segm --> seg#  mezz# chan#  calE        tau [tau2 tau20 [tau3 tau30] ]
#
# file and mezz describe the data acquisition
# core and segm describe the analysis (they should be in another setup file)
# core with low gain is the 36th segment
#
# Empty lines and lines beginning with # are ignored
# (sometime empty lines disturb so ut is safer to us a #)
# What comes after the expected fields is ignored
#

####################################################################################
# ADAPTED FOR USE AS DATA AND EVENT-STRUCTURE DESCRIPTOR IN ProducerDiskMezzanine
# 1) if the filename is a single digit integer (0/1) the data is considered
```

```
#    to come the PCIe readout of the AGATA preprocessing electronics
# 2) the CalE ... parts are not used but don't disturb if they stay in the file
# 3) ProducerDiskMezzanine assumes that the second CC is given here as segm 36
##################################################################################

#############################################################
# Description of data source (as many streams as needed).
# The fields are:
#  1  index of data source (used in the mezzanine section)
#  2  number of mezzanines in this data stream
#  3  filename or PCIe port
#############################################################

file 0 7 Data/1G/event_mezzdata.bdat

#####################################################
# Description of the mezzanines.
# The data fields are:
#  1  index (used in the event description section)
#  2  the data dource the mezzane comes from
#  3  ID of the mezzanine in the mezzanine header
#  4  number of channels in the mezzanine block
#####################################################

mezz   0  0  1  6
mezz   1  0  2  6
mezz   2  0  3  6
mezz   3  0  4  6
mezz   4  0  5  6
```

```
mezz   5  0  6  6
mezz   6  0  7  6

################################################################
# Description of the event: core and related segments
# (the second core of AGATA data is added as extra segment).
# The fields are:
#  1 number of segments (for core)
#    segment number     (for segm)
#  2 index of its mezzanine
#  3 channel number in that mezzanine
# If present, the other fields [energy calibration, trigger
# threshold (core only) and signal decay constant] are ignored
#################################################################

core  37  0  0
segm   0  1  5
segm   1  1  4
segm   2  1  3
segm   3  1  2
segm   4  1  1
segm   5  1  0
segm   6  2  5
segm   7  2  4
segm   8  2  3
segm   9  2  2
segm  10  2  1
segm  11  2  0
segm  12  3  5
```

```
segm  13  3  4
segm  14  3  3
segm  15  3  2
segm  16  3  1
segm  17  3  0
segm  18  4  5
segm  19  4  4
segm  20  4  3
segm  21  4  2
segm  22  4  1
segm  23  4  0
segm  24  5  5
segm  25  5  4
segm  26  5  3
segm  27  5  2
segm  28  5  1
segm  29  5  0
segm  30  6  5
segm  31  6  4
segm  32  6  3
segm  33  6  2
segm  34  6  1
segm  35  6  0
segm  36  0  1
```

C.4 PSAFilter.conf

```
ActualClass      PSAFilterGridSearch
#BasisFile        D:/NarvalTests/base/base33L2mm.bin
```

```
#BasisFile        D:/NarvalTests/base/baseMGS2mm5nsG002.bin
#BasisFile        D:/NarvalTests/base/baseJASS2mm5nsGreen.bin
BasisFile /Data/AGATA/Bases/JASS2mm5ns/BaseGreen.bin
WriteDataPrefix /Data/AGATA/Output/1G/
```

C.5 PreprocessingFilter.conf

```
ActualClass PreprocessingFilterPSA
WriteDataPrefix /Data/AGATA/Output/1G/
XtalkFile         xinv_1325-1340.cal
CoreEnergyGate    20 2000
```

C.6 TrackingFilter.conf

```
ActualClass       TrackingFilterOFT
WriteDataPrefix /Data/AGATA/Output/
SourcePosition   0 0 -115.
```

C.7 Example of a Topology file

```
Chain 3       1R/
Producer      CrystalProducerATCA
Filter        PreprocessingFilterPSA
Filter        PSAFilterGridSearch

Chain 3       1G/
Producer      CrystalProducerATCA
Filter        PreprocessingFilterPSA
Filter        PSAFilterGridSearch
```

```
Chain 3       1B/
Producer      CrystalProducerATCA
Filter        PreprocessingFilterPSA
Filter        PSAFilterGridSearch

Chain 3       2R/
Producer      CrystalProducerATCA
Filter        PreprocessingFilterPSA
Filter        PSAFilterGridSearch

Chain 3       2G/
Producer      CrystalProducerATCA
Filter        PreprocessingFilterPSA
Filter        PSAFilterGridSearch

Chain 3       2B/
Producer      CrystalProducerATCA
Filter        PreprocessingFilterPSA
Filter        PSAFilterGridSearch

Chain 2       ./
Builder       EventBuilder
Filter        TrackingFilterOFT
```

C.8 Event builder

```
BuilderType TimeStamp 100
MinFold 1
Verbose
```

C.9 Example of an OftHits file

```
-1 355.70 0 0 0 10337590

7 355.70 -92.12 -16.01 -219.58 0

-1 80.11 0 0 0 10337593

7 80.11 -84.42 -60.91 -212.07 18

-1 81.90 0 0 0 10337595

7 81.90 -77.06 -41.48 -230.73 6

-1 186.14 0 0 0 10337603

7 186.14 -92.48 -17.28 -225.76 0

-1 209.68 0 0 0 10337607

7 209.68 -97.34 -25.14 -221.92 0

-1 155.19 0 0 0 10337615

7 155.19 -68.64 -56.21 -226.25 12

-1 75.07 0 0 0 10337618

7 75.07 -79.49 -41.76 -220.83 6

-1 85.99 0 0 0 10337642

7 25.44 -107.85 -47.39 -205.73 24

7 60.55 -117.83 -50.00 -214.31 25

-1 56.71 0 0 0 10337656

7 56.71 -93.19 -42.27 -217.34 30

-1 355.31 0 0 0 10337673

7 355.31 -115.81 -36.80 -251.43 33

-1 64.07 0 0 0 10337674

7 64.07 -82.11 -45.26 -216.72 6
```

Appendix D

Summary of Compton polarimetry results

D.1 Summary of asymmetry and linear polarisation results of ^{138}Sm using an AGATA triple cluster

Energy(keV)	**Iγ%**	**Multipolarity**	**Assignment**	**Net $N_{\parallel}$**	**Net $N_{\perp}$**	**Asymmetry**	**Linear polarisation**
139.7	< 1	(M1/E2)	$(14^{-} \rightarrow 13^{-})$	11 ± 3	12 ± 3	0.05 ± 0.25	0.95 ± 5.01
178.2	1	(M1/E2)	$(15^{-} \rightarrow 14^{-})$	6 ± 2	5 ± 2	-0.10 ± 0.37	-0.86 ± 3.16
227.4	4	M1/E2	$(16^{-} \rightarrow 15^{-})$	21 ± 5	19 ± 4	-0.06 ± 0.19	-0.34 ± 1.20

Table D.1 – Continued

Energy(keV)	**Iγ%**	**Multipolarity**	**Assignment**	**Net $N_{\parallel}$**	**Net $N_{\perp}$**	**Asymmetry**	**Linear polarisation**
299.4	3	M1/E1	$(17^{-}\rightarrow 16^{-})$	19 ± 4	15 ± 4	-0.13 ± 0.21	-0.49 ± 0.80
333.6	3	M1/E2	$(18^{-}\rightarrow 17^{-})$	19 ± 4	21 ± 5	0.06 ± 0.19	0.17 ± 0.61
346.9	100	E2	$2^{+}\rightarrow 0^{+}$	557 ± 24	775 ± 28	0.18 ± 0.03	0.51 ± 0.09
356.6	41	E2	$12^{+}\rightarrow 10^{+}$	229 ± 15	240 ± 15	0.03 ± 0.06	0.07 ± 0.14
406.0	< 1	(E2)	$(16^{-}\rightarrow 14^{-})$	8 ± 3	7 ± 3	-0.07 ± 0.31	-0.18 ± 0.78
417.0	< 1	M1/E2	$^{-}\rightarrow 12^{-}$	5 ± 2	7 ± 3	0.18 ± 0.35	0.52 ± 1.01
420.2	2	(M1/E2)	$(19^{-}\rightarrow 18^{-})$	15 ± 4	10 ± 3	-0.22 ± 0.25	-0.61 ± 0.69
444.4	1	(M1/E2)	$(20^{-}\rightarrow 19^{-})$	7 ± 3	8 ± 3	0.07 ± 0.31	0.20 ± 0.85
495.4	4	E2	$(20^{-}\rightarrow 19^{-})$	19 ± 4	35 ± 6	0.33 ± 0.17	0.88 ± 0.46
509.9	< 1	(M1/E2)	$(21^{-}\rightarrow 20^{-})$	6 ± 2	7 ± 3	0.08 ± 0.34	0.23 ± 0.90
520.5	5	E2	$(9^{-}\rightarrow 7^{-})$	21 ± 5	44 ± 7	0.39 ± 0.16	1.00 ± 0.41
527.0	< 1	(E2)	$(17^{-}\rightarrow 15^{-})$	7 ± 3	9 ± 3	0.14 ± 0.30	0.35 ± 0.78
544.9	98	E2	$4^{+}\rightarrow 2^{+}$	593 ± 24	620 ± 25	0.02 ± 0.03	0.06 ± 0.09
547.4	6	(E2)	$18^{+}\rightarrow 16^{+}$	27 ± 5	45 ± 7	0.28 ± 0.15	0.72 ± 0.39
552.3	43	E2	$10^{+}\rightarrow 8^{+}$	279 ± 17	319 ± 18	0.07 ± 0.05	0.20 ± 0.13
556.0	< 1	(M1/E2)	$(22^{-}\rightarrow 21^{-})$	6 ± 2	7 ± 3	0.08 ± 0.34	0.22 ± 0.89
611.6	9	E2	$(11^{-}\rightarrow 9^{-})$	41 ± 6	65 ± 8	0.25 ± 0.12	0.71 ± 0.34
620.7	5	E2	$(11^{-}\rightarrow 9^{-})$	27 ± 5	29 ± 5	0.04 ± 0.16	0.12 ± 0.48

Table D.1 – Continued

Energy(keV)	**Iγ%**	**Multipolarity**	**Assignment**	**Net $N_{\parallel}$**	**Net $N_{\perp}$**	**Asymmetry**	**Linear polarisation**
630.1	4	E2	$(17^- \rightarrow 15^-)$	23 ± 5	27 ± 5	0.09 ± 0.17	0.25 ± 0.49
633.0	< 1	(E2)	$(18^- \rightarrow 16^-)$	7 ± 3	5 ± 2	-0.18 ± 0.35	-0.53 ± 1.04
646.9	1	E2	$(9^- \rightarrow 7^-)$	4 ± 2	6 ± 2	0.22 ± 0.39	0.67 ± 1.18
657.0	39	E2	$14^+ \rightarrow 12^+$	227 ± 15	260 ± 16	0.07 ± 0.05	0.22 ± 0.16
668.3	4	E2	$14^+ \rightarrow 12^+$	23 ± 5	26 ± 5	0.07 ± 0.17	0.19 ± 0.49
676.0	4	(E1)	$14^+ \rightarrow 12^+$	30 ± 5	35 ± 6	0.08 ± 0.15	0.24 ± 0.43
685.9	95	E2	$6^+ \rightarrow 4^+$	535 ± 23	653 ± 26	0.11 ± 0.04	0.32 ± 0.10
686.2	8	E2	$20^+ \rightarrow 18^+)$	-[1]	-[2]	-[3]	-[4]
701.2	9	E2	$(13^- \rightarrow 11^-)$	56 ± 7	67 ± 8	0.10 ± 0.11	0.27 ± 0.30
713.0	12	E2	$12^+ \rightarrow 10^+$	67 ± 8	75 ± 9	0.06 ± 0.10	0.17 ± 0.28
733.3	7	E2	$(15^- \rightarrow 13^-)$	27 ± 5	38 ± 6	0.19 ± 0.15	0.53 ± 0.43
754.0	< 1	E2	$(19^- \rightarrow 17^-)$	-[5]	-[6]	-[7]	-[8]

---

[1] Counts indeterminate (see Section 5.2 for details)

[2] Counts indeterminate (see Section 5.2 for details)

[3] Asymmetry indeterminate (see Section 5.2 for details)

[4] Linear polarisation indeterminate (see Section 5.2 for details)

[5] Counts indeterminate (see Section 5.2 for details)

[6] Counts indeterminate (see Section 5.2 for details)

[7] Asymmetry indeterminate (see Section 5.2 for details)

[8] Linear polarisation indeterminate (see Section 5.2 for details)

Table D.1 – Continued

Energy(keV)	**Iγ%**	**Multipolarity**	**Assignment**	**Net $N_\parallel$**	**Net $N_\perp$**	**Asymmetry**	**Linear polarisation**
754.7	18	E2	$10^{+}\rightarrow 8^{+}$	105 ± 10	120 ± 11	0.07 ± 0.08	0.21 ± 0.23
768.5	3	(E2)	$(16^{+}) \rightarrow 14^{+})$	16 ± 4	21 ± 5	0.15 ± 0.20	0.42 ± 0.57
775.2	91	(E2	$8^{+}\rightarrow 6^{+}$	564 ± 24	701 ± 26	0.12 ± 0.03	0.33 ± 0.10
784.4	4	E2	$(19^{-}\rightarrow 17^{-})$	24 ± 5	35 ± 6	0.21 ± 0.16	0.59 ± 0.46
795.3	12	E2	$14^{+}\rightarrow 12^{+}$	83 ± 9	93 ± 10	0.06 ± 0.09	0.17 ± 0.25
801.1	8	M1/E2	$13^{+}\rightarrow 12^{+}$	70 ± 8	55 ± 7	-0.13 ± 0.11	-0.37 ± 0.30
813.8	4	(E2)	$(13^{-}\rightarrow 11^{-})$	25 ± 5	35 ± 6	0.18 ± 0.16	0.51 ± 0.44
825.1	5	E2	$16^{+}\rightarrow 14^{+}$	30 ± 5	45 ± 7	0.22 ± 0.14	0.63 ± 0.41
853.9	3	E2	$15^{+}\rightarrow 13^{+}$	16 ± 4	30 ± 5	0.33 ± 0.19	0.98 ± 0.55
858.7	3	(E2)	$(15^{-}\rightarrow 13^{-})$	16 ± 4	29 ± 5	0.32 ± 0.19	0.93 ± 0.55
863.1	7	E2	$16^{+}\rightarrow 14^{+}$	47 ± 7	60 ± 8	0.13 ± 0.12	0.38 ± 0.34
865.0	< 1	(E2)	$(20^{-}\rightarrow 18^{-})$	54 ± 7	50 ± 7	-0.04 ± 0.12	-0.11± 0.33
871.3	7	E2	$22^{+}\rightarrow 20^{+}$	50 ± 7	58 ± 8	0.08 ± 0.12	0.23 ± 0.33
886.3	10	M1/E1	$15^{+}\rightarrow 14^{+}$	80 ± 9	65 ± 8	-0.11 ± 0.10	-0.33 ± 0.29
902.0	5	E2	$18^{+}\rightarrow 16^{+}$	32 ± 6	40 ± 6	0.12 ± 0.14	0.32 ± 0.37
910.0	< 1	(E2)	$(18^{+}\rightarrow 16^{+})$	6 ± 2	10 ± 3	0.28 ± 0.31	0.75 ± 0.85
915.0	36	E2	$16^{+}\rightarrow 14^{+}$	235 ± 15	265 ± 16	0.07 ± 0.05	0.18 ± 0.15
918.8	3	E2	$(22^{+}\rightarrow 20^{+})$	18 ± 4	27 ± 5	0.22 ± 0.18	0.63 ± 0.52

Table D.1 – Continued

Energy(keV)	**Iγ%**	**Multipolarity**	**Assignment**	**Net $N_{\parallel}$**	**Net $N_{\perp}$**	**Asymmetry**	**Linear polarisation**
931.9	11	(E1)	$7^{-}\rightarrow 6^{+}$	75 ± 9	90 ± 9	0.10 ± 0.09	0.28 ± 0.26
934.2	3	(E2)	$17^{+}\rightarrow 15^{+}$	18 ± 4	30 ± 5	0.28 ± 0.18	0.75 ± 0.49
947.4	6	E1	$9^{-}\rightarrow 8^{+}$	37 ± 6	50 ± 7	0.16 ± 0.13	0.47 ± 0.38
953.6	3	(E2)	$(21^{-}\rightarrow 19^{-})$	28 ± 5	20 ± 4	-0.18 ± 0.15	-0.53 ± 0.51
954.0	< 1	(E2)	$(21^{-}\rightarrow 19^{-})$	-[9]	-[10]	-[11]	-[12]
956.1	4	E2	$(24^{+}\rightarrow 22^{+})$	24 ± 5	41 ± 6	0.29 ± 0.16	0.86 ± 0.46
962.7	3	(E2)	$(17^{+})\rightarrow 15^{+}$	17 ± 4	28 ± 5	0.27 ± 0.19	0.81 ± 0.56
987.3	5	E2	$(15^{-}\rightarrow 13^{-})$	32 ± 6	41 ± 6	0.14 ± 0.14	0.46 ± 0.48
1018.3	3	(E2)	$(26^{+}\rightarrow 24^{+})$	20 ± 4	28 ± 5	0.18 ± 0.18	0.59 ± 0.57
1035.0	2	(E2)	$(20^{+})\rightarrow 18^{+}$	11 ± 3	18 ± 4	0.27 ± 0.23	0.85 ± 0.74
1049.5	8	(E2)	$(20^{-})\rightarrow 18^{+}$	47 ± 7	60 ± 8	0.13 ± 0.12	0.46 ± 0.41
1059.9	1	(E2)	$(17^{-}\rightarrow 15^{-})$	8 ± 3	7 ± 3	-0.07 ± 0.31	-0.26 ± 1.12
1066.0	< 1	(E2)	$(22^{-}\rightarrow 20^{-})$	8 ± 3	5 ± 2	-0.25 ± 0.34	-0.87 ± 1.19
1077.0	4	(E1)	$(7^{-})\rightarrow 6^{+}$	24 ± 5	39 ± 6	0.26 ± 0.16	0.94 ± 0.56
1084.4	2	(E2)	$(28^{+}\rightarrow 26^{+})$	14 ± 4	18 ± 4	0.14 ± 0.22	0.51 ± 0.79

---

[9] Counts indeterminate (see Section 5.2 for details)

[10] Counts indeterminate (see Section 5.2 for details)

[11] Asymmetry indeterminate (see Section 5.2 for details)

[12] Linear polarisation indeterminate (see Section 5.2 for details)

Table D.1 – Continued

Energy(keV)	**Iγ%**	**Multipolarity**	**Assignment**	**Net $N_{\parallel}$**	**Net $N_{\perp}$**	**Asymmetry**	**Linear polarisation**
1089.8	3	(E2)	$(24^{-}\rightarrow 22^{+})$	18 ± 4	24 ± 5	0.16 ± 0.19	0.57 ± 0.68
1103.0	< 1	(E2)	$(24^{-}\rightarrow 22^{-})$	9 ± 3	8 ± 3	-0.06 ± 0.29	-0.23 ± 1.03
1104.0	17	E2	$18^{+}\rightarrow 21^{-}$	104 ± 10	131 ± 11	0.13 ± 0.08	0.44 ± 0.27
1121.3	2	(E2)	$(23^{-}\rightarrow 13^{-})$	15 ± 4	17 ± 4	0.07 ± 0.21	0.26 ± 0.79
1122.0	< 1	(E2)	$(23^{-}\rightarrow 21^{-})$	7 ± 3	8 ± 3	0.07 ± 0.31	0.27 ± 1.16
1145.6	1	(E2)	$(30^{+}\rightarrow 28^{+})$	7 ± 3	9 ± 3	0.14 ± 0.30	0.51 ± 1.13
1146.8	1	(E2)	$(19^{+}\rightarrow 17^{+})$	7 ± 3	8 ± 3	0.07 ± 0.31	0.31 ± 1.34
1156.3	3	(E1)	$(15^{-})\rightarrow 13^{-})$	19 ± 4	25 ± 5	0.15 ± 0.18	0.68 ± 0.84
1173.0	< 1	(E2)	$(14^{-}\rightarrow 14^{-})$	7 ± 3	5 ± 2	-0.18 ± 0.35	-0.87 ± 1.68
1199.0	< 1	(E2)	$(32^{+}\rightarrow 30^{+})$	7 ± 3	6 ± 2	-0.08 ± 0.34	-0.43 ± 1.73
1219.0	< 1	(E2)	$(27^{-}\rightarrow 25^{-})$	7 ± 3	8 ± 3	0.07 ± 0.31	0.36 ± 1.53
1227.0	6	E2	$14^{+}\rightarrow 12^{+}$	43 ± 7	47 ± 7	0.05 ± 0.13	0.29 ± 0.77
1271.1	3	(E2)	$(20^{+}\rightarrow 18^{+})$	20 ± 4	25 ± 5	0.12 ± 0.18	0.70 ± 1.04
1286.0	< 1	(E2)	$(26^{+}\rightarrow 24^{+})$	7 ± 3	8 ± 3	0.07 ± 0.31	0.43 ± 1.83
1287.0	< 1	(E2)	$(25^{-}\rightarrow 23^{-})$	7 ± 3	8 ± 3	0.07 ± 0.31	0.45 ± 1.92

D.2 Summary of polarisation sensitivity, efficiency and figure of merit of an AGATA triple cluster using ^{138}Sm

Energy(keV)	**Iγ%**	**Multipolarity**	**Polarisation sensitivity (%)**	**Efficiency (%)**	**Figure of merit (%)**
139.7	< 1	(M1/E2)	5.0 ± 0.3	23.0 ± 5.3	0.06 ± 0.02
178.2	1	(M1/E2)	11.6 ± 0.5	24.4 ± 8.2	0.3 ± 0.1
227.4	4	M1/E2	16.0 ± 0.6	25.6 ± 4.5	0.7 ± 0.1
299.4	3	M1/E2	26.3 ± 0.7	25.4 ± 4.9	1.8 ± 0.3
333.6	3	M1/E2	31.5 ± 0.8	28.2 ± 5.0	2.8 ± 0.5
346.9	100	E2	34.5 ± 0.9	32.6 ± 1.0	3.9 ± 0.2
356.6	41	E2	39.5 ± 0.9	28.0 ± 1.5	4.4 ± 0.3
406.0	< 1	(E2)	40.1 ± 0.8	34.9 ± 10.5	5.6 ± 1.7
417.0	< 1	M1/E2	35.2 ± 0.7	31.6 ± 10.5	3.9 ± 1.3
420.2	2	(M1/E2)	36.0 ± 0.7	29.8 ± 6.8	3.9 ± 0.9
444.4	1	(M1/E2)	36.6 ± 0.7	33.3 ± 9.9	4.5 ± 1.3
495.4	4	E2	37.3 ± 0.6	31.2 ± 4.9	4.3 ± 0.7
509.9	< 1	(M1/E2)	37.6 ± 0.6	34.2 ± 11.0	4.8 ± 1.6
520.5	5	E2	39.7 ± 0.6	31.0 ± 4.4	4.9 ± 0.7
527.0	< 1	(E2)	39.5 ± 0.6	35.6 ± 10.3	5.5 ± 1.6

Table D.2 – Continued

Energy(keV)	**Iγ%**	**Multipolarity**	**Polarisation sensitivity (%)**	**Efficiency (%)**	**Figure of merit (%)**
544.9	98	E2	38.2 ± 0.6	30.2 ± 1.0	4.4 ± 0.2
547.4	6	(E2)	38.4 ± 0.6	28.5 ± 3.8	4.2 ± 0.6
552.3	43	E2	37.7 ± 0.5	32.9 ± 1.6	4.7 ± 0.3
556.0	< 1	(M1/E2)	38.1 ± 0.6	34.3 ± 11.5	5.0 ± 1.7
611.6	9	E2	35.3 ± 0.5	31.1 ± 3.5	3.9 ± 0.4
620.7	5	E2	34.2 ± 0.5	32.0 ± 4.9	3.7 ± 0.6
630.1	4	E2	35.7 ± 0.5	35.2 ± 5.8	4.5 ± 0.7
633.0	< 1	(E2)	34.8 ± 0.4	36.7 ± 12.9	4.4 ± 1.6
646.9	1	E2	33.2 ± 0.4	34.5 ± 12.6	3.8 ± 1.4
657.0	39	E2	34.8 ± 0.4	34.0 ± 1.8	4.1 ± 0.2
668.3	4	E2	35.3 ± 0.4	34.8 ± 5.8	4.3 ± 0.7
676.0	4	(E1)	35.0 ± 0.4	38.0 ± 5.5	4.7 ± 0.7
685.9	95	E2	34.8 ± 0.4	31.6 ± 1.1	3.8 ± 0.2
686.2	8	E2	-[13]	-[14]	-[15]
701.2	9	E2	34.2 ± 0.5	32.8 ± 3.4	3.8 ± 0.4
713.0	12	E2	36.6 ± 0.4	35.4 ± 3.5	4.7 ± 0.5

---

[13] Polarisation sensitivity indeterminate (see Section 5.2 for details)

[14] Efficiency (see Section 5.2 for details)

[15] Figure of merit (see Section 5.2 for details)

Table D.2 – Continued

Energy(keV)	**Iγ%**	**Multipolarity**	**Polarisation sensitivity** (%)	**Efficiency** (%)	**Figure of merit** (%)
733.3	7	E2	35.7 ± 0.4	36.9 ± 5.4	4.7 ± 0.7
754.0	< 1	E2	-[16]	-[17]	-[18]
754.7	18	E2	35.2 ± 0.4	34.3 ± 2.6	4.3 ± 0.3
768.5	3	(E2)	35.4 ± 0.4	37.8 ± 7.3	4.7 ± 0.9
775.2	91	(E2	36.0 ± 0.4	34.0 ± 1.1	4.4 ± 0.2
784.4	4	E2	35.4 ± 0.4	35.1 ± 5.3	4.4 ± 0.7
795.3	12	E2	36.3 ± 0.4	35.6 ± 3.1	4.7 ± 0.4
801.1	8	M1/E2	36.2 ± 0.4	36.2 ± 3.8	4.8 ± 0.5
813.8	4	(E2)	36.7 ± 0.4	37.7 ± 5.7	5.1 ± 0.8
825.1	5	E2	35.4 ± 0.3	35.9 ± 4.8	4.5 ± 0.6
853.9	3	E2	34.0 ± 0.3	35.9 ± 6.2	4.2 ± 0.7
858.7	3	(E2)	34.3 ± 0.3	35.4 ± 6.1	4.2 ± 0.7
863.1	7	E2	35.4 ± 0.3	36.8 ± 4.2	4.6 ± 0.5
865.0	< 1	(E2)	36.0 ± 0.3	35.7 ± 4.1	4.6 ± 0.5
871.3	7	E2	35.5 ± 0.3	35.9 ± 4.0	4.5 ± 0.5
886.3	10	M1/E2	35.7 ± 0.3	34.9 ± 3.4	4.4 ± 0.4

---

[16] Polarisation sensitivity indeterminate (see Section 5.2 for details)

[17] Efficiency (see Section 5.2 for details)

[18] Figure of merit (see Section 5.2 for details)

Table D.2 – Continued

Energy(keV)	**Iγ%**	**Multipolarity**	**Polarisation sensitivity (%)**	**Efficiency (%)**	**Figure of merit (%)**
902.0	5	E2	38.4 ± 0.3	34.3 ± 4.7	5.1 ± 0.7
910.0	< 1	(E2)	36.8 ± 0.3	35.6 ± 10.3	4.8 ± 1.4
915.0	36	E2	37.2 ± 0.3	33.9 ± 1.8	4.7 ± 0.3
918.8	3	E2	35.2 ± 0.3	35.2 ± 6.1	4.3 ± 0.8
931.9	11	(E1)	36.1 ± 0.3	34.8 ± 3.1	4.5 ± 0.4
934.2	3	(E2)	36.6 ± 0.3	38.4 ± 6.5	5.1 ± 0.9
947.4	6	E1	34.9 ± 0.3	36.1 ± 4.5	4.4 ± 0.6
953.6	3	(E2)	34.6 ± 0.3	36.6 ± 6.2	4.4 ± 0.7
954.0	< 1	(E2)	-[19]	-[20]	-[21]
956.1	4	E2	33.6 ± 0.3	37.6 ± 5.5	4.2 ± 0.6
962.7	3	(E2)	33.0 ± 0.3	37.2 ± 6.5	4.1 ± 0.7
987.3	5	E2	29.6 ± 0.2	34.9 ± 4.7	3.1 ± 0.4
1018.3	3	(E2)	30.8 ± 0.3	37.2 ± 6.3	3.5 ± 0.6
1035.0	2	(E2)	31.4 ± 0.3	34.5 ± 7.4	3.4 ± 0.7
1049.5	8	(E2)	29.0 ± 0.2	32.7 ± 3.6	2.8 ± 0.3
1059.9	1	(E2)	28.1 ± 0.2	34.9 ± 10.5	2.7 ± 0.8

---

[19] Polarisation sensitivity indeterminate (see Section 5.2 for details)

[20] Efficiency (see Section 5.2 for details)

[21] Figure of merit (see Section 5.2 for details)

Table D.2 – Continued

Energy(keV)	**Iγ%**	**Multipolarity**	**Polarisation sensitivity (%)**	**Efficiency (%)**	**Figure of merit (%)**
1066.0	< 1	(E2)	28.9 ± 0.2	34.2 ± 11.0	2.9 ± 0.9
1077.0	4	(E1)	28.0 ± 0.2	38.9 ± 5.8	3.1 ± 0.5
1084.4	2	(E2)	27.2 ± 0.2	37.2 ± 7.7	2.8 ± 0.6
1089.8	3	(E2)	27.6 ± 0.2	35.3 ± 6.3	2.7 ± 0.5
1103.0	< 1	(E2)	28.7 ± 0.2	37.0 ± 10.5	3.0 ± 0.9
1104.0	17	E2	28.9 ± 0.2	33.5 ± 2.5	2.8 ± 0.2
1121.3	2	(E2)	27.0 ± 0.2	36.4 ± 7.5	2.6 ± 0.5
1122.0	< 1	(E2)	27.0 ± 0.2	35.7 ± 10.7	2.6 ± 0.8
1145.6	1	(E2)	27.1 ± 0.2	37.2 ± 10.9	2.7 ± 0.8
1146.8	1	(E2)	23.4 ± 0.2	34.1 ± 10.2	1.9 ± 0.6
1156.3	3	(E1)	22.0 ± 0.2	39.3 ± 7.0	1.9 ± 0.3
1173.0	< 1	(E2)	21.1 ± 0.2	33.3 ± 11.1	1.5 ± 0.5
1199.0	< 1	(E2)	19.4 ± 0.2	35.3 ± 11.4	1.3 ± 0.4
1219.0	< 1	(E2)	20.5 ± 0.2	38.5 ± 11.7	1.6 ± 0.5
1227.0	6	E2	16.6 ± 0.1	35.9 ± 4.4	1.0 ± 0.1
1271.1	3	(E2)	17.4 ± 0.2	36.9 ± 6.4	1.1 ± 0.2
1286.0	< 1	(E2)	17.2 ± 0.2	39.5 ± 12.0	1.2 ± 0.4
1287.0	< 1	(E2)	16.4 ± 0.1	40.1 ± 13.7	1.1 ± 0.4

Appendix E

Worked example for 346.9 keV

Presented in this appendix is a worked example of how the linear polarisation for gamma-ray energy 346.9 keV was determined.

E.1 Peak area selection and background subtraction

In order to obtain a net number of counts in the parallel and perpendicular direction with respect to the reaction place, it was necessary to carry out a background subtraction of the tracked spectrum that was produced from the NARVAL-emulator. A background fit was performed using the ROOT MINUIT χ^2-fitting programme. The background fit (red line) of the tracked spectrum is shown in Figure E.1. It can be seen that the background fit is in good agreement with the data at gamma-ray energies greater than ~275 keV. The energy gate for each photopeak energy was determined by fitting a Gaussian peak to the appropriate peak area, again using the ROOT [Roo95] MINUIT χ^2-fitting programme. This is shown in Figure E.2 for the 346.9 keV photopeak energy. The red line is the background fit. In this gamma-ray energy region the background fit is in good agreement with the data. From this the photopeak energy range was taken to be 339.8 to 351.5 keV.

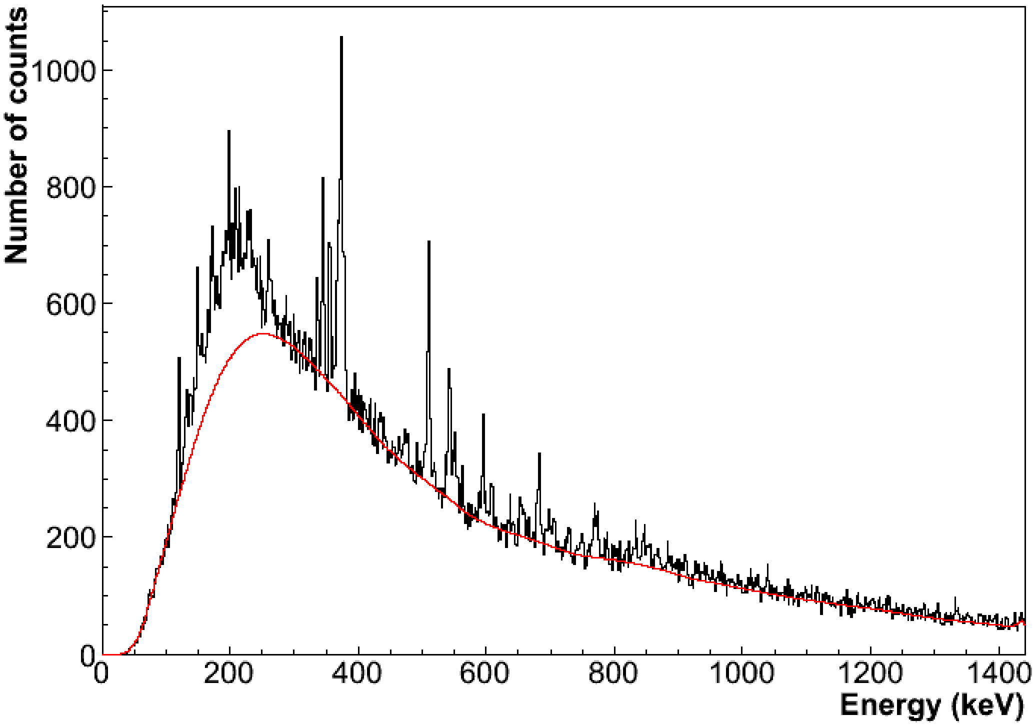

Figure E.1: The background fit of the tracked spectrum.

E.2 Polarisation sensitivity

Following the first interaction a gamma ray was scattered at an angle and was fully absorbed at the second interaction. The pulse-shape analysis algorithm provided coordinates of both the first and second interaction. The azimuthal scattering is defined as the angle between the electric vector of the incident gamma ray and the plane containing the incident and scattered gamma ray. It contains the linear polarisation information [Lei97]. It was necessary to determined all the azimuthal scattering angles from the coordinates produced by the pulse-shape analysis algorithm using the method outlined in Section 4.8.3. In the method angle can be determined in the following, assuming the the gamma ray was emitted from cartesian coordinates *(0,0,0)*. This is shown schematically in Figure E.3.

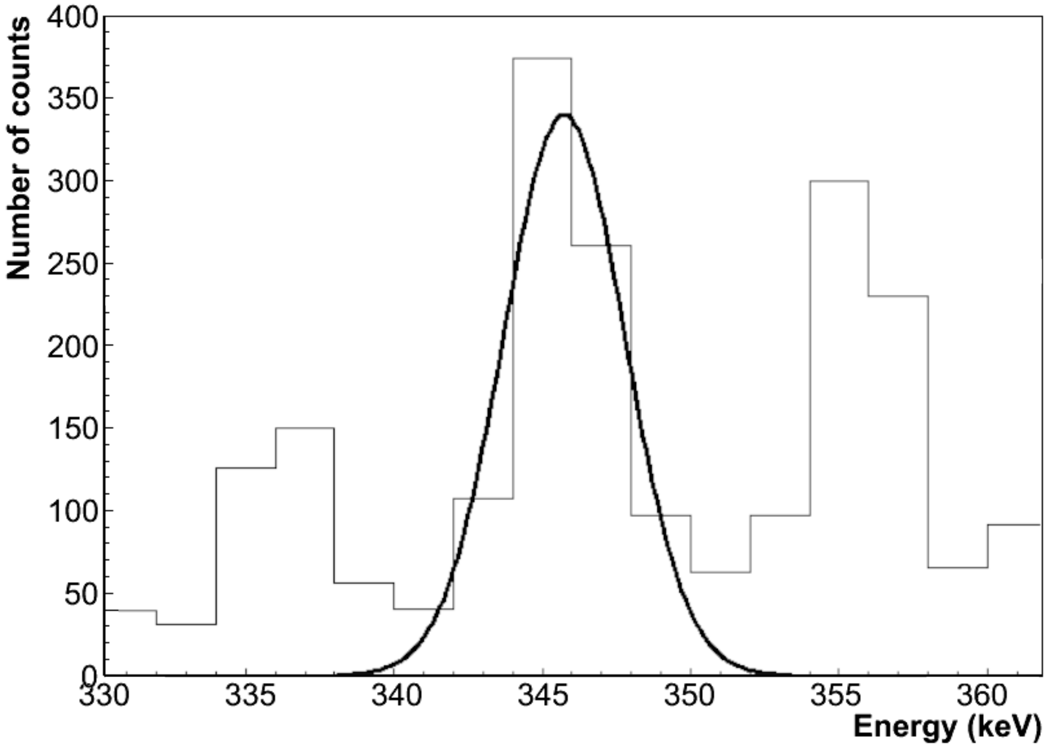

Figure E.2: A background subtracted tracked spectrum in the gamma-ray energy range 330-360 keV. In order to determine the photopeak range a Gaussian fit of the peak area was performed. This is shown here for the photopeak energy 346.9 keV.

- Cartesian coordinates (x_1, y_1, z_1) and (x_2, y_2, z_2) were converted to spherical polar coordinates. This formed *vector 1* and *vector 2*, respectively
- *Vector 3* was determined from the vector difference between *vector 2* and *vector 1*.
- The following equation was used to determine the azimuthal scattering angle,

$$\phi = \cos^{-1} \frac{vector\ 1 \cdot vector\ 3}{||vector\ 1||\ ||vector\ 3||}. \tag{E.1}$$

This produced an azimuthal scattering angular distribution. This is shown for the gamma-ray energy 346.9 keV in Figure E.4. In order to apply Eq. 4.9 it was necessary

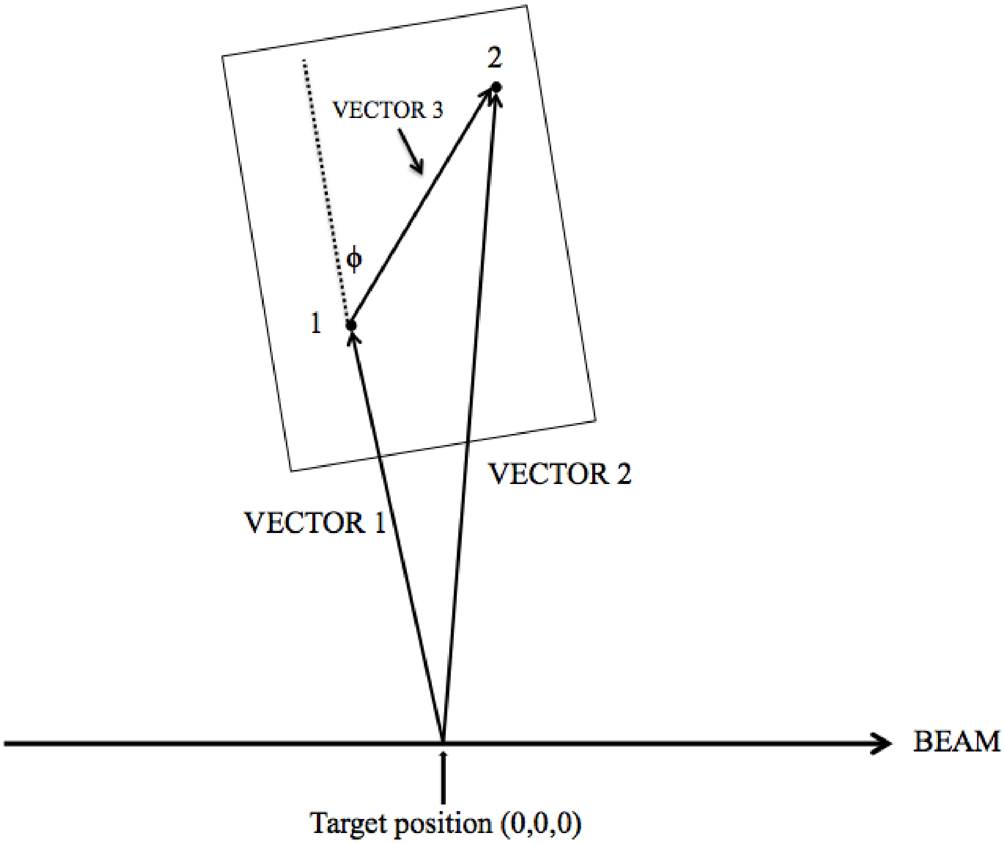

Figure E.3: A schematic diagrams showing the procedure for calculating the azimuthal scattering angle (ϕ).

to obtain a best fit angle. This angle was obtained by using the ROOT MINUIT χ^2-fitting programme and is given to be 126±1.1°. Following this the incident and scattered energy was determined from the method outlined in Section 4.8.4. These are given as 345.9±2.9 and 191.5±1.1 keV, respectively. From this scattered energy and the incident energy the associated k_1 and k_0 were determined using Eq. 2.10. Both these values and the azimuthal scattering angle were substituted into Eq. 4.9 as follows,

$$Q(\phi) = \frac{\sin^2(126)}{(0.55 + 1.80) - \sin^2(126)} = 34.7 \pm 0.9\%. \tag{E.2}$$

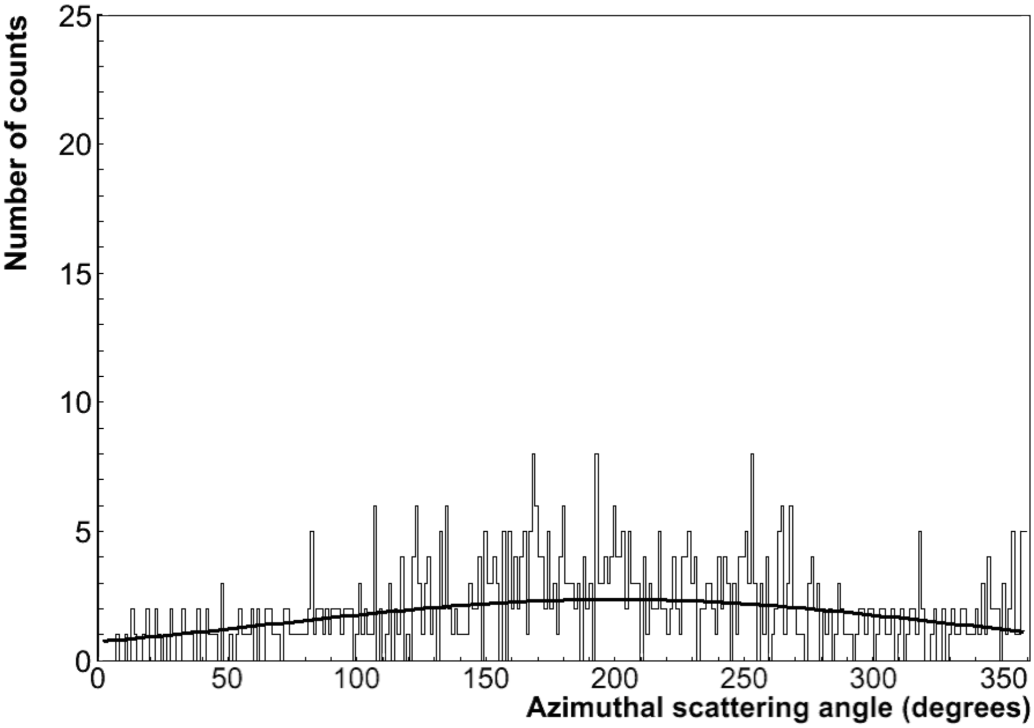

Figure E.4: The azimuthal angular distribution for the 346.9 keV photopeak.

E.3 Asymmetry measurement

This work considered two-interaction events as defined by the pulse-shape analysis algorithm (Sections 4.8.1 and 4.8.2). Following the background subtraction it was necessary to determine the number of two-interaction events and of these events how many scattered perpendicular and parallel to the reaction plane. This was done by using the method outlined in Section 4.8.5. The following outline the terminology that was used in the method description for measuring the asymmetry of an AGATA triple-cluster.

- *Y-perpendicular* - this defines the perpendicular scatter direction with the beam direction.
- *X-perpendicular* - this defines the parallel scatter direction with the beam di-

rection.

- *beam-perpendicular* - the number of gamma rays that scatter perpendicular with the reaction plane.
- *beam-parallel* - the number of gamma rays that scatter parallel with the reaction plane.
- *energy-scatter* - for a given photopeak energy the number of gamma rays that scatter perpendicular and parallel with the reaction plane (E_γ,$N_\perp$,$N_\parallel$).

Assigning ***Y-perpendicular*** and ***X-perpendicular***

The AGATA triple cluster was positioned at 80° to the beam direction. It was assumed that *interaction 1* was approximately 90° to the beam direction and the gamma ray will scatter perpendicular or parallel after *interaction 1*. The directions of scatter *Y-perpendicular* and *X-perpendicular* were assigned, representing a y-axis and x-axis to the beam direction, respectively. This is shown schematically in Figure E.5. A vector for *Y-perpendicular* was determined from the cross product of *vector 1* (*interaction 1*) and the beam direction. A vector for *X-perpendicular* was determined from the cross product of the *vector 1* and *Y-perpendicular*.

Calculating a scattering vector

A vector was determined which contained the scattering information. This was done by determining the vector difference of the coordinates of *vector 1* and *vector 2*. This produced a new vector *vector 3*. This is shown schematically in Figure E.6.

Determining ***beam-perpendicular*** and ***beam-parallel***

To determine the scatter direction of *vector 3* it was necessary to project *vector 3* in both the *X-perpendicular* and *Y-perpendicular* directions. The perpendicular projection was determined from the dot product of *vector 3* and *Y-perpendicular*.

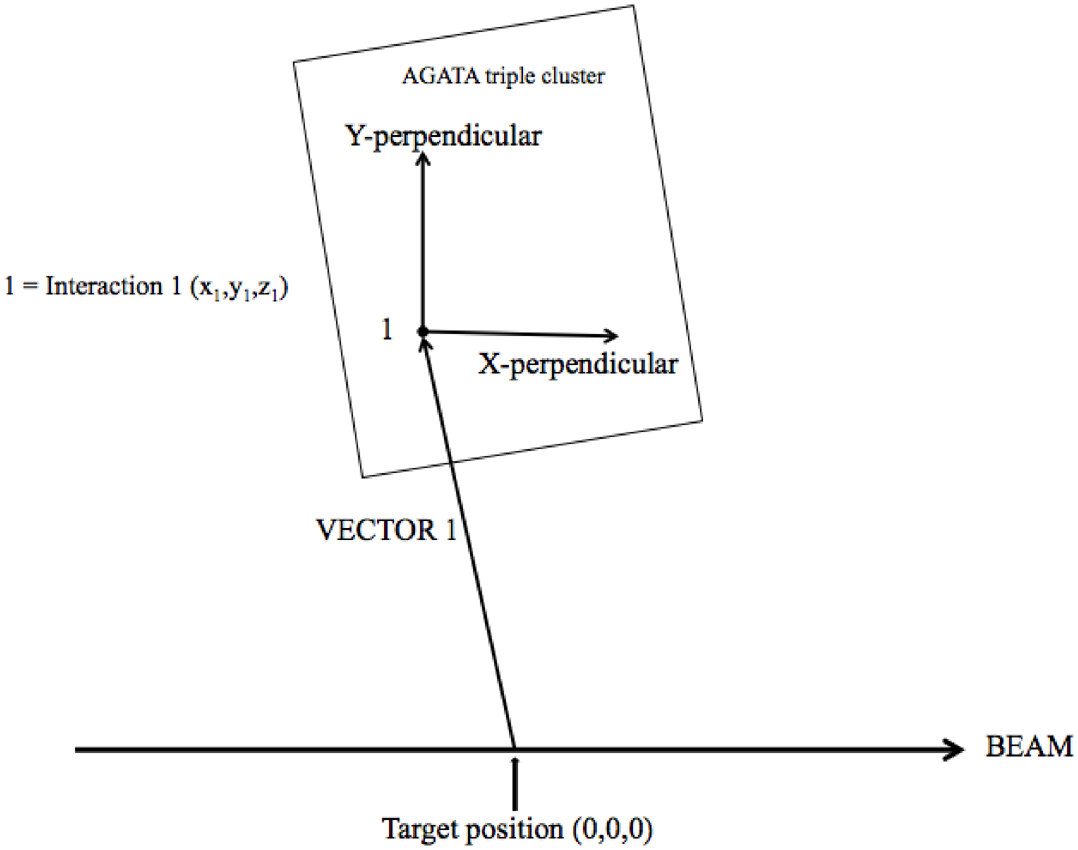

Figure E.5: A schematic diagram showing the direction of *Y-perpendicular* and *X-perpendicular* with the beam direction.

The parallel projection was determined from the dot product of *vector 3* and *X-perpendicular*. From this *beam-perpendicular* and *beam-parallel* was constructed.

Constructing energy-scatter

For each gamma-ray energy of ^{138}Sm an *energy-scatter* was constructed. By applying Eq. 2.15 differing polarisations will appear as positive or negative. As the angular momentum vector of an electric transition is polarised perpendicular to the beam direction and a magnetic transition is polarised parallel, a positive value of asymmetry (A), will show the transition to be predominantly electric in character. From the *energy-scatter* a spectrum for (E_γ,$N_\perp$) and (E_γ,$N_\parallel$) was produced. This is shown for

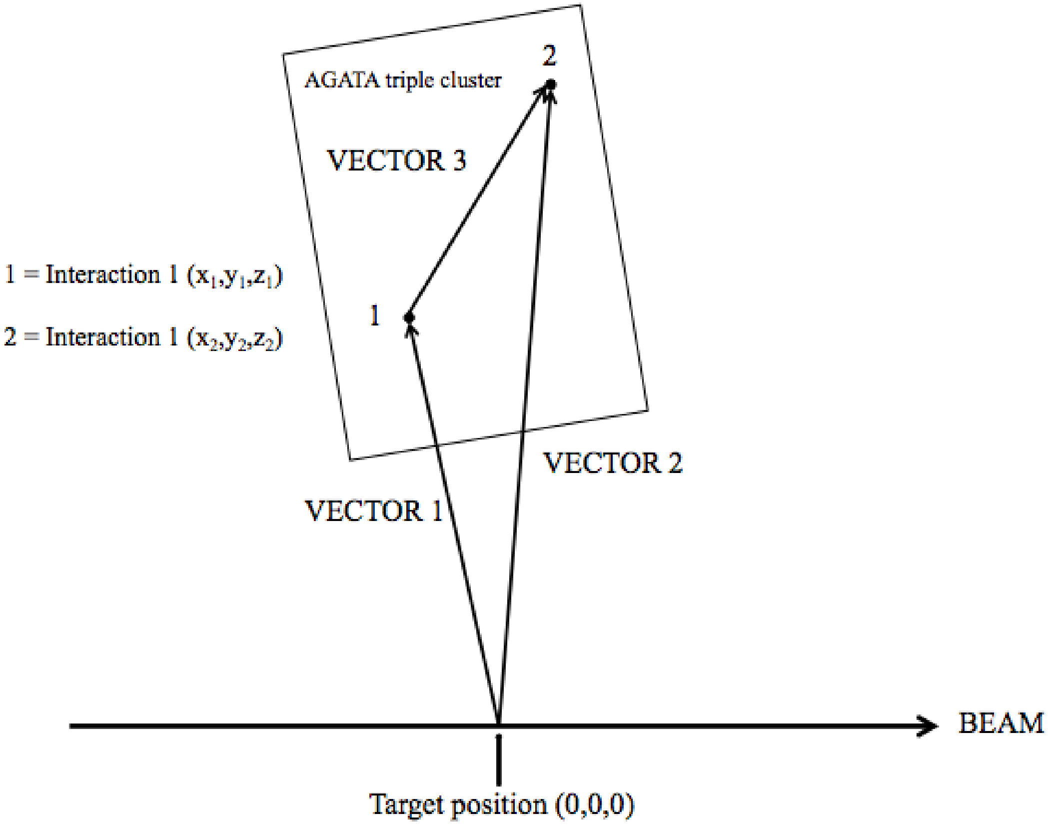

Figure E.6: A schematic diagram representing the relationship between *vector 1* and *vector 2* with the scattering *vector 3*.

all energies in Figure E.7 and E.8, respectively.

Count type	$N_\perp$	$N_\parallel$
Number of counts	775±28	557±23

Table E.1: Summary of the perpendicular ($N_\perp$) and parallel ($N_\parallel$) net number of counts for 346.9 keV.

The asymmetry was calculated using Eq. 4.11. In this equation a is a normalisation constant that was determined as outlined in Section 4.8.6 and is given as 1.1±0.01.

$$A = \frac{1.1(775 - 557)}{1.1(775 + 557)} = 0.18 \pm 0.03. \tag{E.3}$$

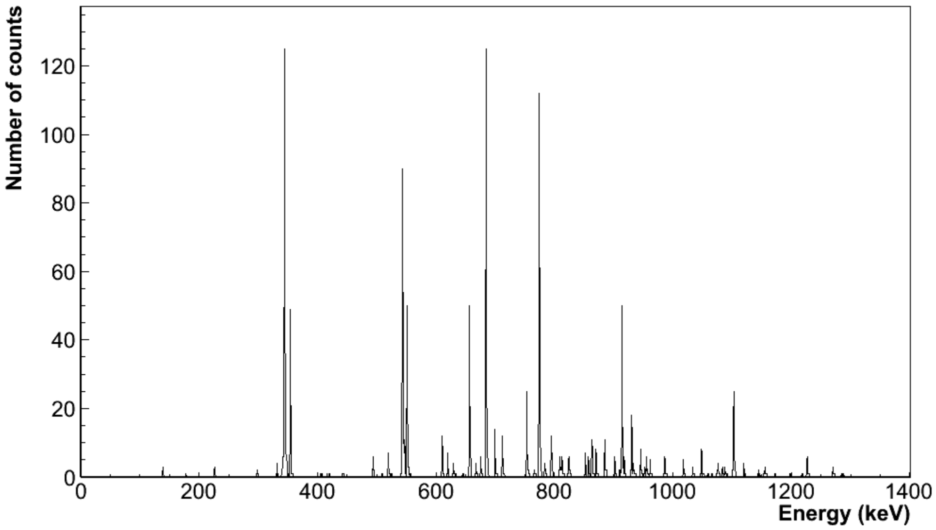

Figure E.7: A perpendicular scattering spectrum of two-interaction events.

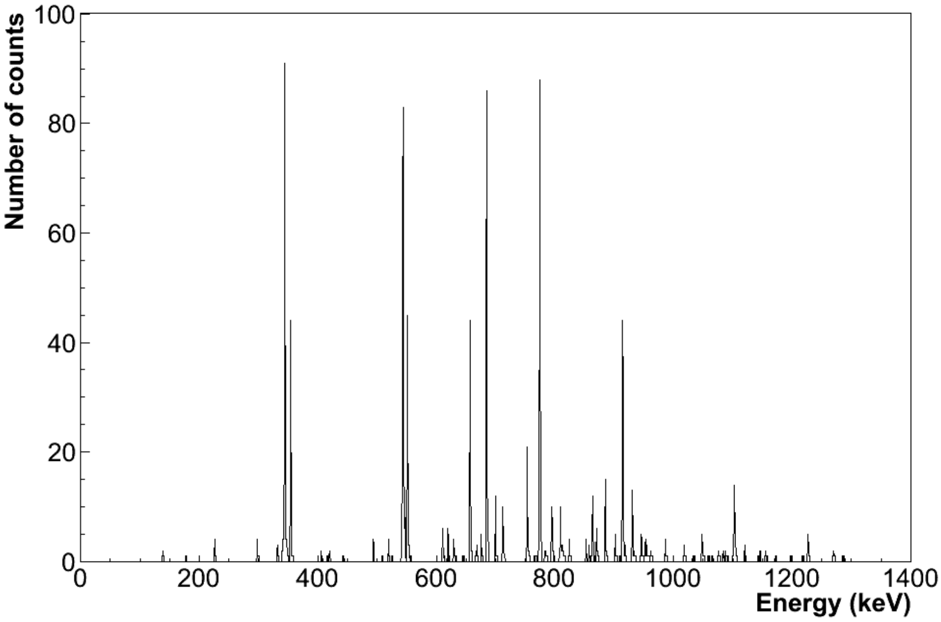

Figure E.8: A parallel scattering spectrum of two-interaction events.

E.4 Linear polarisation

The linear polarisation was determined from the polarisation sensitivity and the asymmetry measurement using Eq. 4.12. With the sign of the asymmetry measurement indicating an electric or magnetic character.

$$P = \frac{0.18}{0.35} = 0.51 \pm 0.09. \tag{E.4}$$

This gamma-ray energy was assigned an electric character.

Bibliography

[Ada95] *http://www.dmoz.org/Computers/Programming/Languages/Ada*

[Bea94] C.W. Beausang and J. Simpson. Large arrays of suppressed spectrometers for nuclear structure experiments. *Journal of Physics G: Nuclear and Particle Physics*, 22(5):527-558, 1996.

[Bec92] F.A. Beck, *et al.*, Workshop on Large Gamma-Ray Detector Arrays. Chalk River, Canada, AECL-10163 364, 1992.

[Ben11] P.C. Bender. *Nuclear structure of neutron rich ^{34}P using in-beam gamma ray spectroscopy.* Ph.D. thesis, Florida State University, 2011. Original reference, H. Morinaga and T. Yamazaki. In-Beam Gamma-Ray Spectroscopy. North-Holland, 1976.

[Bos09] A.J. Boston, et al., Performance of an AGATA asymmetric detector. *Nuclear Instruments and Methods in Physics Research A*, 604:482, 2009.

[Bru08] B. Bruyneel and B. Birkenbach. *AGATA Detector simulation Library (ADL) v.2.0*, 2008.

[But73] P.A. Butler, *et al.*, Construction and use of a three Ge(li) Compton polarimeter. *Nuclear Instruments and Methods*, 108:497-502, 1973.

[Cas05] R.F. Casten. Nuclear Structure from a Simple Perspective. 2nd Ed.. Oxford Science Publications, 2005.

[Cos95] E. Costa, *et al.*, Design of a scattering polarimeter for hard X-ray astronomy. *Nuclear Instruments and Methods in Physics Research A*, 366:161-172, 1995.

[Dar06] I.G. Darby. *Decay Spectroscopy of the Light Rhenium Isotopes.* Ph.D. thesis University of Liverpool, 2006.

[Dav65] C.M. Davission. Interaction of γ-Radiation with matter. North-Holland, 1965.

[Dim08] M.R. Dimmock. *Characterisation of a AGATA symmetric Prototype Detector.* Ph.D. thesis, University of Liverpool, 2008.

[Dro06] Ch. Droste, *et al.*, Polarisation sensitivity of the CLUSTER detector used in EUROBALL array. *Nuclear Instruments and Methods in Physics Research A*, 556:182-186, 2006.

[Duc99] G. Duchene. *et al.*, The Clover: a new generation of composite Ge detectors. *Nuclear Instruments and Methods in Physics Research A*, (432):90-110, 1999.

[Eva55] R.D. Evans. The Atomic Nucleus, McGraw-Hill. New York, 1955.

[Fan47] U. Fano. Phys. Rev. 72, 26 (1947)

[Fer79] A. Ferguson, *et al,*, Polarization sensitive detectors. *Nuclear Instruments and Methods*,(162):565-586, 1979.

[Fio10] E. Fioretto, *et al.*, Spectroscopic studies with the PRISMA-CLARA set-up. *Journal of Physics Conference Series*, 205, 2010.

[Gra05] X. Grave, *et al.*, NARVAL a Modular Distributed Data Acquisition. System with Ada 95 and RTAI. *IEEE Realtime*, 2005.

[Gar95] L. Garcia-Raffi, *et al.*, Non-orthogonal gamma-ray Compton polarimeters. *Nuclear Instruments and Methods in Physics Research Section A*, (359):628-631, 1995.

[Ham05] N.J. Hammond, *et al.*, Ambiguity in gamma-ray tracking of ’two-interaction’ events. *Nuclear Instruments and Methods in Physics Research A*, (547):535-540, 2005.

[Han67] W.G. Hanson and B.W. Sargent. Photopeak Efficiency of a Well-Type Scintillation Detector. *The Review of Scientistic Instruments*, (39)4, 1968.

[Hut02] C. Hutter, *et al.*, Polarisation sensitivity of a segmented HPGe detector up to 10MeV. *Nuclear Instruments and Methods in Physics Research A*, 489: 247-256, 2002.

[Jon02] G. Jones. Calibration of Compton polarimeters. *Nuclear Instruments and Methods in Physics Research Section A: Accelerators, Spectrometers, Detectors and Associated Equipment*, 491(3):452-459, 2002.

[Kac11] M. Kaci and V. Mendez. The AGATA GRID computing model for data management and data processing. July 2011.

[Kno00] G.F. Knoll. Radiation Detection and Measurement. Third Edition, Wiley (2000).

[Kor01] W. Korten and J. Gerl. *Agata, technical proposal.* GSI, Darmstadt, 2001.

[Kra88] K.S. Krane. Introductory Nuclear Physics. Wiley, 1988.

[Lee01] J.H. Lee, *et al.*, Linear Polarization Measurements of Gamma Rays in ^{155}Gd by using a Segmented Compton Polarimeter. *Journal of the Korean Physical Society*, (40)5:793-801, 2002.

[Lee02] J.H. Lee, *et al.*, Polarisation sensitivity and efficiency for a planar-type segmented germanium detector as a Compton polarimeter. *Nuclear Instruments and Methods in Physics Research Section A*, (506):125-135, 2003.

[Lei97] R.M. Leider. New Generation of Gamma-Detector Arrays, Experimental Techniques in Nuclear Physics, ed. D.N. Poenaru and W. Greiner. Walter de Gruyter. New York, 1997.

[Log73] B. Logan, *et al.*, A figure of merit for gamma-ray polarimeters. *Nuclear Instruments and Methods in Physics Research Section A* (108):603-604, 1973.

[Lop04] A. Lopez-Martens. *et al.*, γ-ray tracking algorithms: a comparison. *Nuclear Instruments and Methods in Physics Research Section A*, (533):545-466, 2004.

[Met50] F. Metzger *et al.*, A Study of the Polarization-Direction Correlation of Successive Gamma-Ray Quanta. *Phys. Rev.*, (78):551-558, 1950.

[Mil08] D. Miller, *et al.*, Linear polarisation sensitivity of SeGA detectors. *Nuclear Instruments and Methods in Physics Research A*,(581)3:713-718, 2008.

[Ola05] A. Olariu *et al.*, Pulse Shape Analysis for the location of the γ-interactions on AGATA. *IEEE*(53), 2006.

[Pau94] E.S. Paul, *et al.*, Shape coexistence in ^{138}Sm and evidence for the rotational alignment of a pair of N=6 neutrons. *J. Phys. G: Nucl. Part. Phys.*, (20)1405, 1994.

[Pau95] E.S. Paul. Angular correlation analysis with EUROGAM II. Technical report. 1995.

[Ram39] W. Ramo. Currents Induced in Electron Motion. *Proceedings of the Institute of Radio Engineers*, (27)9:585-585, 1939.

[Rec08] F. Recchia. *In-beam test and imaging capabilities of the AGATA prototype detector.* PhD. thesis, University of Padua, 2008.

[Roo95] *http://root.cern.ch/drupal/*

[Sim05] J. Simpson. The AGATA project. *Journal of Physics G: Nuclear and Particle Physics*, 31:S1801-S1806, 2005.

[Sim06] J. Simpson. The AGATA project. *Journal of Physics: Conference Series*, 41(1):72-80. 2006.

[Sch94] B. Schlitt, *et al.*, A sectored Ge-Compton polarimeter for parity assignment in photon scattering experiments. *Nuclear Instruments and Methods in Physics Research A*, 337:416-426, 1994.

[Sch97] G.J. Schmid, *et al.*, Gamma-ray polarization sensitivity of the Gammasphere segmented germanium detectors, *Nuclear Instruments and Methods in Physics Research Section A: Accelerators, Spectrometers, Detectors and Associated Equipment*, 47(1):95-110, 1997.

[Sch09] M.C. Schlarb. *Simulation and Real-Time Analysis of Pulse Shapes from segmented HPGe-Detectors.* PhD. Thesis, University of Koln, 2009.

[Sho38] W. Shockley. Currents to conductors induced by a moving point charge. *Journal of Applied Physics*, 10:635. 1938.

[Tin00] M. Tinker and R. Lambourne. Further Mathematics for the Physical Sciences. Wiley, New York, 2000.

[Twi75] P.J. Twin. Electromagnetic Interactions in Nuclear Spectroscopy, ed. W.D. Hamilton. 1975.

[Uns11] C.D. Unsworth. *Characterisation of an Asymmetric AGATA Detector*. Ph.D. thesis, University of Liverpool, 2011.

[Wer95] A. Von der Werth, *et al.*, Two Compton polarimeter constructions for modern standard γ-spectroscopy. *Nuclear Instruments and Methods in Physics Research A*, 357:458-466, 1995.

[Wie10] A. Wiens, *et al.*, The AGATA Triple Cluster Detector, *Nuclear Instruments and Methods in Physics Research Section A: Accelerators, Spectrometers, Detectors and Associated Equipment*, 618(1-3):223-233, 2010.